ALMA MATER STUDIORUM
UNIVERSITÀ DI BOLOGNA

DOTTORATO DI RICERCA IN

IL FUTURO DELLA TERRA, CAMBIAMENTI CLIMATICI E SFIDE SOCIALI

Ciclo 38

Settore Concorsuale: 02/C1 - ASTRONOMIA, ASTROFISICA, FISICA DELLA TERRA E DEI PIANETI

Settore Scientifico Disciplinare: FIS/06 - FISICA PER IL SISTEMA TERRA E IL MEZZO CIRCUMTERRESTRE

A PHYSICS-INFORMED METHODOLOGY TO ESTIMATE PM2.5 FROM SATELLITE AOD

Presentata da: Giorgia Proietti Pelliccia

Coordinatore Dottorato

Silvana Di Sabatino

Supervisore

Tiziano Maestri

Co-supervisore

Erika Brattich

Esame finale anno 2026

Abstract

The exposure to aerosol pollution poses critical risks to human health, with effects ranging from allergies to chronic respiratory diseases, and even carcinogenic effects (Brunekreef and Holgate, 2002; Thangavel et al., 2022; Li et al., 2022b). For this reason, the monitoring of aerosol concentrations, in the form of Particulate Matter (PM) mass concentration, is crucial especially in highly populated and industrialized areas. However, the number of ground-based monitoring stations in Europe is close to 3 to 4 stations per million inhabitants, which is not sufficient for wide regional monitoring, and is 0.2 or less in developing countries (Martin et al., 2019). Recently, the European Commission revised the Ambient Air Quality Directive with a limit yearly average value of 10 $\mu g/m^3$ for $PM_{2.5}$ (PM of particles with aerodynamic diameters lower than 2.5 μm) to reach the recommended limits provided by WHO (EU, 2024). In this Directive, alternative methodologies for the estimation of $PM_{2.5}$ are allowed to complement the currently active monitoring networks.

In the past decades, the possibility of using satellite data to complement the ground-based monitoring of PM was vastly investigated (Hoff and Christopher, 2009; Chen et al., 2019). Satellite retrievals of Aerosol Optical Depth (AOD) can be related to PM with several methodologies, including statistical or scaling methods (Ma et al., 2021). The AOD is the total aerosol extinction in the atmospheric column and can be related to PM assuming that the aerosols are well-mixed below the Mixing Layer Height (MLH). The physical equations that relate the extinction of incoming Solar radiation by aerosols and the respective mass concentration are well established (e.g. Koelemeijer et al. (2006); Wang et al. (2009)). These equations describe how aerosol extinction depends on microphysical characteristics (aerosol type and size) that influence the aerosol extinction properties.

The Po Valley, in Northern Italy, is an area known for frequent air pollution exceedances due to high urbanization and industrialization density, as well as its peculiar geography and meteorological conditions, that facilitate the accumulation of atmospheric pollutants. During winter, stable atmospheric conditions confine the majority of aerosols within the Planetary Boundary Layer. Previous studies highlighted that the majority of AOD in the area refers to aerosols below the

MLH (Barnaba et al., 2010; Ferrero et al., 2011), creating favourable conditions for relating satellite-observed Aerosol Optical Depth (AOD) to surface-level $PM_{2.5}$ concentrations. For these reasons, it is an ideal area of study to test alternative approaches to estimate $PM_{2.5}$. The present work focuses on a physics-informed approach that exploits these theoretical relationships from aerosol radiative transfer theory, to estimate $PM_{2.5}$ from AOD. The city of Bologna is selected as a case study due to its peculiar location in the Po Valley.

The particle growth due to increase in Relative Humidity (RH), known as hygroscopicity, is a phenomenon that critically impacts the correlation between AOD and $PM_{2.5}$. Previous studies (Arvani et al., 2016; Ferrero et al., 2019) have investigated the use of empirical functions in the Po Valley, to account for the difference between satellite AOD, retrieved at ambient conditions, and $PM_{2.5}$, measured at dry conditions. These functions are generally not representative of the RH changes in our study area, as they rely on empirical coefficients found in the literature. This work proposes a physics-informed approach that directly relates $PM_{2.5}$ at ambient RH with satellite AOD, without relying on empirical humidity corrections.

In the present work, we exploit the availability of $PM_{2.5}$ estimates at ambient RH retrieved by an Optical Particle Counter (OPC) in Bologna during February-September 2023. Interest in $PM_{2.5}$ estimates from OPCs is recently growing (Karagulian et al., 2019). The Light Aerosol Optical Counter (LOAC) (Renard et al., 2010, 2016) provides information on aerosol particle type classification in addition to the Particle Number concentration (PN) measured by all OPCs. From LOAC measurements, we compute the three key parameters required by the theoretical equation: Effective Radius from PN measurements, average Extinction Efficiency from particle type classification combined with Mie theory calculations, and average mass density from type-specific density values. This allows us to estimate the theoretical coefficient that links $PM_{2.5}$ and AOD without empirical fitting. We also use high spatial resolution satellite AOD retrieved from MODIS observation with the MAIAC algorithm (Lyapustin et al., 2018), which performs better than other algorithms over urban areas. Co-located with the LOAC, we use Mixing Layer Height (MLH) measurements from a ceilometer.

We find that $PM_{2.5}$ measured at ambient RH is better correlated with AOD than the reference $PM_{2.5}$ measured under dry conditions (RH $< 50\%$). The linear correlation coefficient R between $PM_{2.5}$ (ambient RH) and satellite AOD (scaled by MLH) is 0.56 with a coefficient of determination $R^2 = 0.31$, while with dry $PM_{2.5}$ we obtain R = 0.16, which indicates the absence of linear correlation. When we estimate the theoretical coefficient between $PM_{2.5}$ and AOD using the LOAC auxiliary variables, R increases to 0.76, with $R^2 = 0.58$, which is almost double the value obtained without using the LOAC auxiliary variables. This confirms that explicit representation of local aerosol properties enhances both physical consistency

and predictive capability.

We perform numerical simulations of urban aerosol Particle Size Distributions (PSD) to evaluate the Effective Radius retrieved by the LOAC. The simulations show that, due to its detection limit to particles with radii greater than 0.1 μm, the LOAC overestimates the Effective Radius by up to a factor of 2 in realistic urban conditions. After applying a simple correction to account for the presence of particles with radii lower than 0.1 μm, the estimation error decreases to below 20%. When the corrected Effective Radius is used to estimate the linear coefficient linking $PM_{2.5}$ and AOD, the slope of the linear regression between measured and estimated $PM_{2.5}$ approaches the value of 1, confirming the validity of the proposed methodology.

The proposed physics-informed methodology involves the use of satellite AOD, $PM_{2.5}$ and auxiliary data from the LOAC, as well as meteorological variables (MLH and RH) and simulated aerosol optical properties. This approach validates the physical equation linking columnar and surface aerosol properties, demonstrating its applicability in complex urban environments such as the Po Valley. The methodology can be extended by integrating other satellite AOD products and independent estimates of aerosol PSD properties. In this way, it offers a flexible framework for integrating satellite and ground-based observations, contributing to a deeper understanding of aerosol microphysics and its influence on air quality variability.

Contents

Abstract i

1 Introduction 1
- 1.1 Aerosol pollution: health effects and monitoring . . . 1
  - 1.1.1 Aerosol definition . . . 1
  - 1.1.2 $PM_{2.5}$ health effects . . . 4
  - 1.1.3 Air Quality Guidelines and Directives . . . 5
  - 1.1.4 PM measurement techniques . . . 6
  - 1.1.5 Alternative methodologies . . . 7
- 1.2 Study area . . . 8
- 1.3 Objectives . . . 10
  - 1.3.1 Thesis structure . . . 10

2 State of the Art 13
- 2.1 From Extinction to Mass Concentration . . . 13
  - 2.1.1 Definition of Relevant Properties . . . 13
  - 2.1.2 Theoretical relationship between AOD and PM . . . 16
  - 2.1.3 Mass-specific Extinction Coefficient . . . 16
  - 2.1.4 Linear Approximation . . . 17
- 2.2 From Satellite AOD to Ground-based PM . . . 19
  - 2.2.1 Statistical Approach . . . 20
  - 2.2.2 Study Definition . . . 22

3 Preliminary studies 25
- 3.1 Datasets . . . 26
  - 3.1.1 LOAC data . . . 27
  - 3.1.2 Satellite AOD . . . 30
  - 3.1.3 Mixing Layer Height . . . 31
  - 3.1.4 Auxiliary data . . . 36
- 3.2 LOAC Data Analysis . . . 36
  - 3.2.1 $PM_{2.5}$ and Particle Number Variability . . . 37
  - 3.2.2 PSD, Effective Radius and particle type . . . 39
  - 3.2.3 Discussion . . . 41
- 3.3 Variation of PM with RH . . . 42
  - 3.3.1 Seasonality of PM and RH . . . 42
  - 3.3.2 PM-RH Hysteresis . . . 46

3.3.3 Hygroscopic Growth Function . . . 48
3.4 Conclusions . . . 53
3.4.1 Key Findings . . . 53
3.4.2 Implications for the Methodology . . . 54

4 Physics-informed AOD-PM Framework 55
4.1 Objectives . . . 55
4.2 Effective Radius Correction . . . 56
4.2.1 Numerical simulations . . . 56
4.2.2 Correction Algorithm . . . 57
4.3 Computation of aerosol properties . . . 59
4.3.1 Effective Radius from LOAC Measurements . . . 59
4.3.2 Average Mass Density . . . 59
4.3.3 Average Extinction Efficiency . . . 60
4.3.4 Uncertainties . . . 61
4.4 Linear regressions . . . 61
4.4.1 Theoretical framework . . . 61
4.4.2 Statistical Methods . . . 62
4.4.3 Dataset . . . 63
4.4.4 Results . . . 64
4.4.5 Discussion . . . 68
4.5 Conclusions . . . 70

5 Conclusions 71
5.1 Summary and main contributions . . . 71
5.1.1 Research context and motivation . . . 71
5.1.2 Methodological developments and main results . . . 72
5.2 Limitations and future perspectives . . . 73
5.3 Concluding remarks . . . 74

A Aerosol Optical Properties 75
A.1 Aerosol Properties Database . . . 75
A.1.1 Optical Properties . . . 76
A.2 Urban aerosol PSDs . . . 80
A.2.1 Code description . . . 80

Bibliography 81

Chapter 1

Introduction

1.1 Aerosol pollution: health effects and monitoring

Gases, particulates, and biological components present in the atmosphere cause air pollution. The World Health Organization (WHO) reports that the burden of disease attributable to air pollution is comparable to other major global health risks such as tobacco smoking and unhealthy diet, and recognizes air pollution as the single largest environmental threat to human health (WHO, 2021).

Air pollution has been recognised as a major environmental health issue since the early twentieth century (Brunekreef and Holgate, 2002). Severe smog episodes during the first half of the century, characterised by high concentrations of sulfur dioxide and smoke particles, caused thousands of deaths from respiratory illness. These events led to the first air quality legislation, such as the 1970 Clean Air Act in the U.S.A. (Anderson et al., 2011). While traditional smog constituents have declined substantially over the past three decades, other pollutants have emerged as primary concerns (Brunekreef and Holgate, 2002). Current air quality monitoring focuses on five major pollutants: Particulate Matter (PM), Ozone (O_3), Nitrogen dioxide (NO_2), Sulfur dioxide (SO_2) and Carbon Monoxide (CO) (WHO, 2003, 2006, 2021).

The following sections examine $PM_{2.5}$ health effects, trace air quality standards from WHO guidelines to current EU directives, and describe measurement techniques for PM mass and number concentration.

1.1.1 Aerosol definition

The particulate component of air pollution, defined as Particulate Matter (PM), is made up of aerosols, which are solid and liquid particles suspended in the atmo-

sphere. Aerosols originate from natural or anthropogenic sources through direct emission into the atmosphere or through condensation and coagulation processes (Li et al., 2022a). After emission, aerosol particles undergo atmospheric aging through condensation, coagulation, and cloud processing, which alter their size and morphology (Bhandari et al., 2019). Black carbon particles, for example, are emitted as small chain-like structures but grow substantially through interactions with atmospheric gases and particulate matter.

Given the large variety of origin and formation, aerosols differ in sizes, chemical composition and morphology. To standardize aerosol characterization, researchers use the Aerodynamic Equivalent Diameter (AED). The AED of a particle represents the diameter of a spherical particle with unit density and the same settling velocity. Different particles with the same AED tend to have the same settling velocity and deposition times. This classification is crucial because PM deposited in human airways depends on AED (Anderson et al., 2011). Additionally, the spherical approximation enables application of Mie theory to aerosol-radiation interactions.

Health effects of aerosol pollution are studied in relation to $PM_{2.5}$ and PM_{10}, which measure the mass concentration (in $\mu g/m^3$) of particles with AED below 2.5 and 10 μm, respectively. Larger particles settle quickly due to gravity and are typically filtered by the nose and upper airway. $PM_{2.5}$ is suspended in the air for extended periods of time, during which it can be transported for long distances, and it is small enough to penetrate the airways (Wang et al., 2025; Anderson et al., 2011; Harrison and Beddows, 2017; Kwon et al., 2020).

While fine and coarse particles are well characterized by mass concentration ($PM_{2.5}$ and PM_{10}), ultra-fine particles (UFP) with AED below 0.1 μm are best quantified by particle number concentration (PN) (Kwon et al., 2020; Anderson et al., 2011). Figure 1.1 shows the difference in size-resolved distribution of number, area and mass concentration for UFP, $PM_{2.5}$ and PM_{10}.

Aerosol chemical composition varies widely depending on formation mechanism and source. Anthropogenic aerosols originate from industrial combustion, vehicle exhaust, and resuspension of road dust and debris (Harrison and Beddows, 2017; Harrison, 2020). In urbanized areas, vehicle exhaust aerosols contain elemental carbon and organic compounds, while nitrate and sulfate aerosols form from NO_2 and SO_2 in urban air pollution, combined with ammonia primarily from agricultural sources. Biomass burning and cooking also contribute organic and black carbon, and trace mineral elements are present in soil resuspension (Harrison, 2020). Atmospheric microplastics have recently emerged as an additional anthropogenic aerosol component of growing concern, with plastic particles detected even at remote coastal locations far from emission sources (Rindelaub et al., 2025).

Aerosols of natural origin are mineral dust from deserts and arid areas, trans-

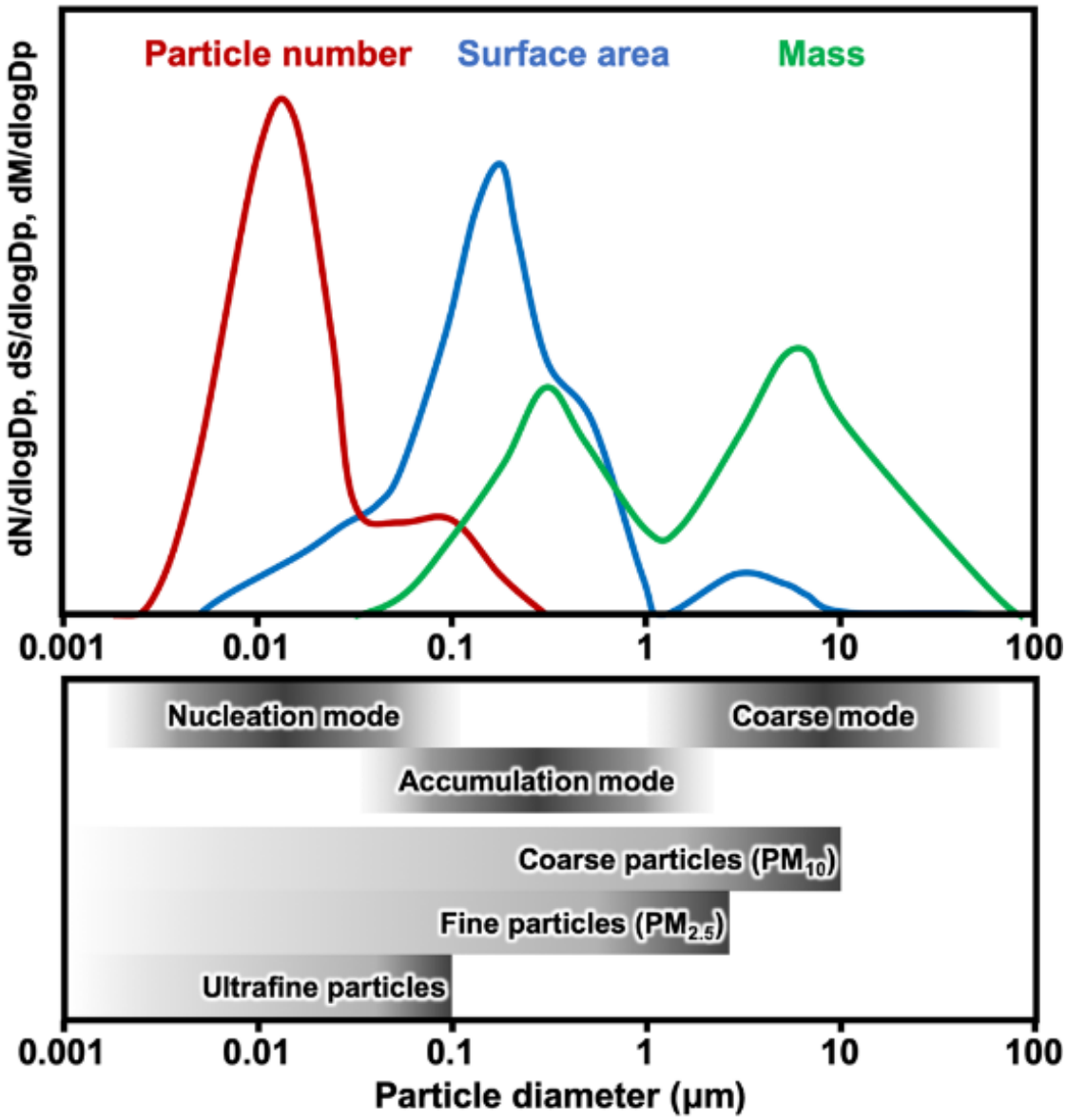

Figure 1.1: Top: Size-resolved distributions of number, area and mass concentration; bottom: classification of aerosols according to formation and aerodynamic equivalent diameter (from Kwon et al. (2020)).

ported over long distances even to highly populated areas, volcanic dust which constitutes the particulate component of eruptions, and smoke and mineral particles from biomass burning. Natural sources of aerosols include volcanic emissions, dust storms, wildfire smoke, and biological particles such as pollen (Almeida et al., 2006; Anderson et al., 2011). In the context of infectious disease transmission, actions such as coughing or sneezing generate aerosols that spread pathogens (Jones and Brosseau, 2015).

1.1.2 $PM_{2.5}$ health effects

$PM_{2.5}$ affects multiple organ systems, with cardiovascular impacts representing the largest health burden. Cardiovascular diseases account for approximately two-thirds of $PM_{2.5}$-attributable health impacts (Brook et al., 2010; Anderson et al., 2011). $PM_{2.5}$ exposure induces systemic inflammation and oxidative stress through multiple pathways: inflammatory markers directly impair cardiac tissue function, while particulate matter triggers arterial vasoconstriction and endothelial dysfunction (Thangavel et al., 2022; Watkins et al., 2012). These mechanisms elevate blood pressure and heart rate, substantially increasing the risk of arrhythmia, thrombosis, and acute cardiac events (Raza et al., 2013).

Due to its small size, $PM_{2.5}$ penetrates deep into the respiratory system, depositing in the alveolar region where it triggers inflammatory and allergic responses (Anderson et al., 2011). Chronic exposure causes persistent pulmonary inflammation, contributing to the development of bronchitis, Chronic Obstructive Pulmonary Disease (COPD), and asthma (Thangavel et al., 2022; Li et al., 2022b). $PM_{2.5}$ also impairs pulmonary immune function, increasing susceptibility to respiratory infections including pneumonia and elevating mortality from respiratory diseases (Li et al., 2022b; Anderson et al., 2011).

Long-term $PM_{2.5}$ exposure increases the risk of chronic respiratory diseases and lung cancer (Wang et al., 2025). Specific $PM_{2.5}$ components (including sulfates, organic compounds, and heavy metals) act as carcinogens (Harrison et al., 2004; Hamra et al., 2014). Urban aerosols, which predominantly consist of these chemical constituents, present particularly elevated cancer risks. The WHO classifies diesel engine exhaust, a major component of urban PM, as carcinogenic (WHO, 2021). Diesel exhaust particles and associated hydrocarbons (including benzene) increase the risk of both lung and bladder cancer (Thangavel et al., 2022; Hamra et al., 2014; Turner et al., 2017). Cancer risk from $PM_{2.5}$ exposure varies substantially by location, pre-existing health conditions, genetic predisposition, age, and baseline pollution levels, with higher risks observed in more polluted regions (Wang et al., 2025).

$PM_{2.5}$ exposure increases both the incidence and mortality of respiratory viral infections through two mechanisms (Thangavel et al., 2022). First, chronic $PM_{2.5}$

exposure compromises pulmonary immune defenses, reducing host resistance to viral pathogens (Hirota et al., 2015; Morales et al., 2017). Second, evidence suggests that particulate matter may serve as a carrier for viral particles, potentially extending their airborne persistence and transmission range (Frontera et al., 2020), though the epidemiological significance of this mechanism remains under investigation.

Given these wide-ranging health impacts, international organizations have developed progressively stricter air quality guidelines.

1.1.3 Air Quality Guidelines and Directives

The World Health Organization has published Air Quality Guidelines (AQG) since 1987 to translate scientific evidence on health effects into recommended exposure limits. While not legally binding, these guidelines inform national air quality regulations worldwide (Krzyzanowski and Cohen, 2008).

The first WHO AQG (1987) and its 2000 revision addressed 37 common air pollutants (WHO, 2000). The 2005 Global Update (WHO, 2006) represented a major advancement, providing the first globally applicable reference values based on systematic literature review. This update established annual limits of 10 $\mu g/m^3$ for $PM_{2.5}$ and 20 $\mu g/m^3$ for PM_{10}, alongside 24-hour exposure limits.

Since 2005, improved measurement techniques and larger cohort studies have revealed health impacts at lower PM concentrations than previously documented. Advances include higher-resolution satellite observations and improved exposure assessment models that account for individual mobility patterns. Additionally, longer follow-up periods in existing cohorts enabled detection of effects from cumulative low-level exposure that shorter studies could not identify. Research demonstrates no threshold concentration below which $PM_{2.5}$ causes no adverse effects (Krzyzanowski and Cohen, 2008). Beelen et al. (2013) analysed 22 European cohort studies and found significant associations between $PM_{2.5}$ exposure and all-cause mortality even at concentrations below the then-current EU limit of 25 $\mu g/m^3$.

Responding to this evidence, WHO published revised AQGs in 2021 (WHO, 2021), substantially lowering recommended limits. The new annual guidelines specify $PM_{2.5}$ below 5 $\mu g/m^3$ and PM_{10} below 15 $\mu g/m^3$. For short-term exposure, 24-hour averages should remain below 15 $\mu g/m^3$ ($PM_{2.5}$) and 45 $\mu g/m^3$ (PM_{10}), with no more than 3-4 exceedance days annually.

The guidelines also provide interim targets for regions with high baseline pollution. These interim targets establish four progressive levels, allowing highly polluted regions to demonstrate health benefits at each stage while working toward the guideline values. These recommendations reflect systematic reviews of long-term (Chen and Hoek, 2020) and short-term (Orellano et al., 2020) PM exposure

studies (Whaley et al., 2021).

The updated guidelines also address regional disparities in monitoring capacity and pollution levels, particularly between high-income and low- and middle-income countries. WHO noted that low- and middle-income countries often experience higher PM concentrations but have fewer monitoring stations per capita. The 2021 guidelines therefore emphasize the use of low-cost sensors and satellite-based methods to supplement traditional monitoring networks in under-resourced regions.

European Union Implementation

Individual countries establish legally binding air quality standards based on WHO recommendations, typically including reference measurement methods and additional requirements for sensitive locations. In the European Union, the EU Directive 2008/50/EC (EU, 2008) implemented the 2005 WHO guidelines, setting annual limits of 25 $\mu g/m^3$ for $PM_{2.5}$ and 40 $\mu g/m^3$ for PM_{10}. This directive designated gravimetric analysis as the reference method, while permitting validated automatic measurement techniques (Pucer, 2019; Kuklinska et al., 2014).

The revised Ambient Air Quality Directive (EU, 2024) aligns more closely with WHO 2021 guidelines, reducing annual limits to 10 $\mu g/m^3$ ($PM_{2.5}$) and 20 $\mu g/m^3$ (PM_{10}), which represents a reduction of more than 50% for $PM_{2.5}$. The revision mandates increased spatial coverage of monitoring stations through reassessment of minimum sampling point requirements to ensure representativeness of PM measurements. This increase is particularly needed near schools and hospitals. These locations serve vulnerable people, such as children, the elderly, and individuals with pre-existing conditions, who face elevated health risks from PM exposure. Modelling techniques such as chemical transport models and land-use regression approaches are expected to complement fixed monitoring networks.

To meet these stringent limits, reliable measurement techniques are essential.

1.1.4 PM measurement techniques

Accurate PM estimation is crucial for monitoring aerosol exposure. As mentioned above, PM mass concentration is regulated by each country according to WHO guidelines, setting the limit values and the measurement methods. In the following, the main techniques for measuring aerosol mass concentration are presented. Since the number concentration is an important property of fine and ultra-fine particles, we also present the typical measurement techniques to estimate the number concentration and the particle number size distribution.

Mass Concentration

Several air quality directives designate the gravimetric method as the reference standard. This method collects aerosol samples on filters over a fixed period, typically 24 hours. Mass concentration is calculated from the difference in filter weight before and after sampling. Usually, the filter is conditioned at fixed temperature and relative humidity, and the sampling period is 24 hours. For this reason, the identification of fast PM changes during the day is not possible with gravimetric measurements (Kiresova and Guzan, 2022).

Gravimetric techniques are used as reference for the certification of other types of instruments as equivalent to the standard (Charron et al., 2003; Pucer, 2019). The Tapered Element Oscillating Microbalance (TEOM) and the Beta attenuation are widely used alternative methods, allowed by the EU Directives (Aggarwal et al., 2013; Shukla and Aggarwal, 2022; Hauck et al., 2004).

The beta-attenuation technique measures changes in beta-ray intensity before and after passing through a filter to determine the particle mass on the filter (Chueinta and Hopke, 2001). It requires little operator attention and the inaccuracies due to ambient Relative Humidity and local factors can be corrected by region-specific correction and adjusted inlet system (Shukla and Aggarwal, 2022).

The TEOM technique uses a small oscillating glass tube whose oscillation frequency changes with the mass of deposited aerosol particles. Inaccuracies in the measurements can arise from the loss of semi-volatile material as the sample is heated. For this reason, TEOM instruments are usually equipped with a filter dynamics measurement system (FDMS) that measures the semi-volatile fraction of PM (Pucer, 2019). TEOM measurements still need a correction factor that accounts for the effect of relative humidity and temperature (Charron et al., 2003; Hauck et al., 2004)

Number concentration

In recent years, Optical Particle Counters (OPCs) have been employed as part of air quality monitoring networks because of their portability, higher temporal resolution and limited costs with respect to conventional reference instrumentation utilized for PM measurement (Karagulian et al., 2019). OPCs detect the Particle Number concentration (PN) in specific size bins and retrieve the PM mass concentration through an internal algorithm.

1.1.5 Alternative methodologies

The revised EU Directive permits alternative PM estimation methodologies to supplement ground-based measurements. This is especially important in areas where

the sampling points are below the minimum required by the current regulations.

In Europe, there are 3 or 4 ground-based monitors per million inhabitants on average; the situation is worse in other countries (Martin et al., 2019). Global studies that use ground-based measurements of PM refer mainly to data from high-income countries, and as a result the mortality estimates are not predictive for low- and middle-income countries. However, $PM_{2.5}$ concentrations are higher in these counties than in high-income countries, thus needing more studies on health effects of $PM_{2.5}$. The availability of alternative methodologies to estimate $PM_{2.5}$ in these areas is crucial for the correct estimation of risks related to $PM_{2.5}$ (Sharma et al., 2020).

In the last decades, the scientific community has pursued the idea of using satellite observations to increase temporal and spatial resolution of the sparse ground-based networks (Hoff and Christopher, 2009). Aerosol Optical Depth (AOD) is the main parameter of interest in monitoring the atmospheric aerosol content from satellite observations (Wei et al., 2019). Several methodologies exploit AOD datasets from long-term satellite observational records to derive PM at a regional scale (Ma et al., 2021). They will be discussed further in Section 2.2.

The use of alternative techniques to estimate PM exposure has already proven useful in different studies. For example, Cohen et al. (2017) used integrated satellite AOD, chemical transport models, and ground-level PM measurements to estimate the population-weighted $PM_{2.5}$. They analysed the long-term trends of attributable deaths to air pollution ($PM_{2.5}$ and ozone) and estimated that aerosol pollution was the fifth major risk factor of mortality in 2015, with increasing trends over the previous 25 years.

Southerland et al. (2022) used the dataset by Hammer et al. (2020) that integrated multiple satellite AOD observations and ground-based PM measurements with a chemical transport model to provide annual average $PM_{2.5}$ values from 1998 to 2018. They analysed data from over 10000 urban areas globally and found that $PM_{2.5}$ are widely heterogeneous in these areas. An improvement of PM estimates at city level is thus needed.

1.2 Study area

The Po Valley, located in northern Italy, exhibits distinct seasonal variation in aerosol mass concentration. During winter, the frequent stability conditions and low wind velocity tend to favour the trapping and accumulation of pollutants (Carbone et al., 2010). Particle accumulation produces a concentration gradient within the Planetary Boundary Layer (PBL), which correlates with a vertical gradient in relative humidity (Ferrero et al., 2011). The concentration gradient is also linked to a vertical gradient of aerosol light extinction. During winter, aerosol extinction

tends to increase in the lowest levels of the atmosphere and simultaneously to decrease at altitudes higher than 1 km; during spring and summer, the extinction is evenly distributed in the atmospheric column. As a result, during winter more than 80% of AOD refers to particles below 1 km (Barnaba et al., 2010).

The relative composition of PM also varies during the year according to changes in aerosol emissions. Approximately 75% of urban $PM_{2.5}$ in the Po Valley consists of water-soluble inorganic compounds (nitrates and sulfates) and carbon (Ricciardelli et al., 2016). Local emission sources in cities comprise different types of fuel due to traffic and residential heating, which leads to different fractions of Black Carbon and organic compounds during the year (Scotto et al., 2021). In the city of Bologna, at least 40% of $PM_{2.5}$ is due to traffic emissions, 24% is composed of road dust, and 8% is due to biomass burning; the levels of mineral dust, which are usually negligible, often increase in the summer during episodes of desert dust intrusion (Tositti et al., 2013).

In the last decades, MODIS AOD has been used with empirical, statistical and machine learning methodologies to estimate the PM spatial variability in the area. Koelemeijer et al. (2006) and Di Antonio et al. (2023) analysed satellite AOD data and highlighted the contrast between the high atmospheric pollution in the Po Valley compared to nearby areas. Di Nicolantonio et al. (2009) was one of the first studies to implement a semi-empirical methodology, and found a correlation coefficient R^2 of 0.68 and 0.59 between MODIS AOD and daily $PM_{2.5}$, reaching values of 0.7 when using monthly averages. More recent studies (Arvani et al., 2016; Ferrero et al., 2019; Stafoggia et al., 2019) exploited MAIAC AOD product (Lyapustin et al., 2018), retrieved from MODIS observations with a spatial resolution of 1 km x 1 km, to better characterize the spatial variation of PM.

Hygroscopicity is the property of some aerosols to grow in size according to their water uptake, changing their optical properties as well as their mass concentration. A corrective function is needed when relating AOD, retrieved at ambient humidity, to PM, which is measured in controlled environments with RH $< 50\%$. The use of this function should improve the correlation between the two quantities. The main issue is the empirical nature of this function, whose coefficients depend on the local aerosol characteristics (Zieger et al., 2013; Hänel, 1981).

Among recent studies in the area, Ferrero et al. (2019) and Arvani et al. (2016) considered the use of a hygroscopic growth function within their methodologies and found that the results of linear correlation between AOD and PM were not significantly improved. The use of hygroscopic functions will be discussed in Section 2.1.4 and investigated in Section 3.3. The present work explores the possibility of using PM measurements at ambient humidity alongside satellite AOD to obtain a semi-empirical function without the use of hygroscopic functions, thus avoiding the propagation of the uncertainties due to inaccurate humidity corrections.

1.3 Objectives

The preceding sections established that aerosol pollution poses a major threat to human health and that ground-based monitoring networks remain insufficient for global PM coverage. Satellite-based AOD retrievals offer a promising complement to ground measurements, but translating columnar AOD to surface-level $PM_{2.5}$ requires careful consideration of local aerosol properties and atmospheric conditions.

The Po Valley is affected by high levels of aerosol pollution, especially during winter, when meteorological conditions and its enclosed geography limit atmospheric circulation and favour pollutant accumulation (Carbone et al., 2010). When the majority of aerosols are well-mixed near the surface, as is common during Po Valley winters, $PM_{2.5}$ can be estimated from AOD through a linear equation whose coefficients depend on local aerosol optical properties. The present work focuses on this relationship, exploring its sensitivity to key aerosol optical parameters, and to develop a preliminary physics-informed methodology exploiting auxiliary data from a Light Optical Aerosol Counter (LOAC), satellite retrievals, and atmospheric boundary layer measurements.

1.3.1 Thesis structure

This thesis comprises five chapters that progressively develop a physics-informed methodology for relating satellite AOD to ground-level $PM_{2.5}$.

Chapter 1 establishes the context and motivation for this work, reviewing the health impacts of $PM_{2.5}$ pollution, the evolution of air quality standards, and current measurement techniques. It then describes the Po Valley study region and outlines the research objectives.

Chapter 2 develops the theoretical foundation by deriving the relationship between aerosol mass concentration and optical properties, particularly the Aerosol Optical Depth (AOD). This chapter also reviews statistical methodologies previously used in the literature to relate PM and AOD, providing context for the physics-informed approach developed here.

Chapter 3 characterizes the observational data used in this work, including ground-based $PM_{2.5}$ measurements, satellite MAIAC AOD retrievals, particle number size distributions from a LOAC, and mixing layer height estimates from ceilometer measurements. Preliminary data analysis establishes the quality and limitations of available observations.

Chapter 4 presents the core contribution of this thesis: a physics-informed methodology that exploits the theoretical relationships developed in Chapter 2 using the datasets described in Chapter 3. This chapter details the derivation of the mass-specific extinction coefficient from LOAC measurements, presents the resulting $PM_{2.5}$ estimates, and discusses sensitivity to key aerosol optical parameters.

Chapter 5 synthesizes the main findings, highlights the advantages and limitations of the physics-informed approach compared to purely empirical methods, and proposes directions for future development of the methodology.

Appendix A documents the structure of an aerosol optical properties database and provides code for computing optical characteristics of urban aerosol mixtures. While this work was fundamental to developing the physics-informed methodology, it is presented separately to maintain focus on the main study.

Chapter 2

State of the Art

2.1 From Extinction to Mass Concentration

2.1.1 Definition of Relevant Properties

In the framework of Radiative Transfer (RT), aerosols are particles with varying sizes and properties that can scatter or absorb electromagnetic radiation. Particles interact with radiation differently depending on their radius r relative to the wavelength λ of the incoming radiation. For this reason, the size parameter x is defined as

$$x = \frac{2\pi r}{\lambda} \tag{2.1}$$

and different approximations can be used according to its value (Liou, 2002). The optical properties of atmospheric gases are usually computed with the Rayleigh approximation because of their smaller size relative to typical wavelengths of atmospheric radiation. On the other hand, aerosols and clouds are typically computed through the Mie approximation. Mie theory is valid for $x \geq 1$. Typical aerosol radii are in the range $r = 10^{-2} - 10^{1}\mu$m and they interact with Solar and Earth radiation according to their size. Smaller aerosol particles have a greater contribution in the Ultraviolet (UV) and Visible (VIS) range of Solar radiation, while larger particles ($r > 5\mu$m) also contribute to scattering and absorption in the Near Infrared (NIR).

The Lambert-Beer-Bouger Law states that the decrease in the Radiance I_λ[1] of a light beam at wavelength λ, that interacts with matter, is described by an exponential function which depends on the monochromatic optical properties of the medium (Hulst and Van De Hulst, 1981). Considering the incoming Solar

[1] The Radiance or Intensity of radiation is a monochromatic quantity defined in units of energy per unit area, angle, and wavelength (W m$^{-2}sr^{-1}/\mu$m).

radiation at fixed wavelength, the total extinction due to the atmosphere (from the Top of Atmosphere $z = TOA$ to the surface, $z = 0$) can be computed as:

$$I_\lambda(0) = I_\lambda(TOA)\, e^{-\int_0^{TOA} k_{ext}(\lambda) ds}. \tag{2.2}$$

where k_{ext} is the atmospheric **Extinction Coefficient**. The total extinction due to the atmosphere can be divided in the contribution of atmospheric gases and aerosols: $k_{ext,tot} = k_{ext,gas} + k_{ext,aer}$. The integral in the exponent of Eq. 2.2 is defined as the Total Optical Depth of the atmosphere. In the following, we consider only the aerosol component of the optical properties; for instance, we refer to the aerosol Extinction Coefficient as k_{ext}. The **Aerosol Optical Depth** (AOD) is a unitless quantity defined as:

$$AOD(\lambda) = \int_0^{TOA} k_{ext}(\lambda) ds. \tag{2.3}$$

The **Extinction Efficiency** $Q_{ext} = Q_{abs} + Q_{sca}$ is a unitless property depending on the physical properties of the particle (particle radius r) and its optical properties (Refractive Index $RI = n + ik$), as well as the radiation wavelength λ. The **Extinction Cross-section** (in m^2) of a particle of radius r can be written as:

$$\sigma_{ext}(r, RI, \lambda) = Q_{ext}(r, RI, \lambda)\, \pi r^2. \tag{2.4}$$

In the following, we assume a set of representative constant values of RI for the urban aerosol mixture characteristic of the Po Valley. Under this assumption, the dependence on RI is omitted from subsequent expressions and Q_{ext} is treated as a function of λ and r only.

Atmospheric aerosols are usually studied as a mixture of particles with different radii. Rather than describing the extinction properties of each aerosol particle, it is useful to describe the properties of the total aerosol mixture. The **Particle Size Distribution** (PSD) describes the number concentration of particles with radius between r and $r + dr$:

$$n(r) = \frac{dn}{dr}; \tag{2.5}$$

the total Number of particles is the integral of the PSD:

$$\int_{r_1}^{r_2} n(r) dr = N_{tot}. \tag{2.6}$$

The Extinction Coefficient k_{ext} of a particle mixture is obtained by integrating the Extinction Cross-section over the Particle Size Distribution:

$$k_{ext}(\lambda) = \int_{r_1}^{r_2} \sigma_{ext}(r, \lambda) n(r) dr = \int_{r_1}^{r_2} Q_{ext}(r, \lambda) \pi r^2 n(r) dr. \tag{2.7}$$

The Particle Size Distribution of a homogeneous aerosol mixture can be described by a **lognormal** size distribution (Eq. A.1). Aerosol PSDs can be defined as one or a sum of lognormal functions with different parameters depending on the composition of the mixture. For example, urban aerosols PSD can be described by the sum of two or three lognormal functions (Cugerone et al., 2018). Lastly, when considering an aerosol mixture described by a PSD $n(r)$, it is useful to define the Effective Radius:

$$r_{eff} = \frac{\int_{r_1}^{r_2} \pi r^3 n(r) dr}{\int_{r_1}^{r_2} \pi r^2 n(r) dr}. \tag{2.8}$$

We can define the Particle Area, Volume, and Mass Distributions from the PSD. Assuming spherical particles with homogeneous mass density ρ:

$$A(r) = \frac{dn}{dr} 4\pi r^2 \tag{2.9}$$

$$V(r) = \frac{dn}{dr} \frac{4}{3} \pi r^3 \tag{2.10}$$

$$M(r) = \rho V(r) = \frac{dn}{dr} \frac{4}{3} \pi \rho r^3 \tag{2.11}$$

The total mass concentration of an aerosol mixture can be computed by integrating Eq. 2.11:

$$M_{tot} = \int_{r_1}^{r_2} M(r) dr = \frac{4}{3} \pi \rho \int_{r_1}^{r_2} r^3 n(r) dr. \tag{2.12}$$

In the framework of aerosol pollution monitoring, the Mass Concentration is measured in specific size ranges (see Chapter 1). Considering the particle diameter D instead of the radius, the $PM_{2.5}$ of a homogeneous aerosol mixture can be defined as follows:

$$PM_{2.5} = \frac{4}{3} \pi \rho \int_0^{2.5} \left(\frac{D}{2}\right)^3 n(D) dD. \tag{2.13}$$

The aerodynamic diameter is defined as the diameter that the particle would have if spherical, with a mass density $\rho = 1 g/cm^3$ and same settling velocity (Baron and Willeke, 2001). Moreover, the thresholds chosen for PM_1, $PM_{2.5}$ and PM_{10} refer to a collection efficiency of 50% of the sampling systems. This means that PM may contain particles with diameters slightly larger than the nominal value.

2.1.2 Theoretical relationship between AOD and PM

The following formulation is considered the basis of the relationship between AOD and PM, and has been extensively described and used in literature (Koelemeijer et al., 2006; Wang et al., 2009; Hoff and Christopher, 2009). We consider a fixed wavelength in the Visible range (usually 500 or 550 nm). Firstly, we define the **Average Extinction Efficiency** of the aerosol mixture (Hansen and Travis, 1974):

$$\langle Q_{ext,aer} \rangle = \frac{\int_{r_1}^{r_2} Q_{ext}(r)\pi r^2 n(r)dr}{\int_{r_1}^{r_2} \pi r^2 n(r)dr}. \tag{2.14}$$

Eq. 2.14 and Eq. 2.8 (Effective Radius) can be substituted in Eq. 2.7 (Extinction Coefficient) to define the Extinction Coefficient of the aerosol mixture as:

$$k_{ext} = \frac{\langle Q_{ext} \rangle}{r_{eff}} \cdot \int_0^{\infty} \pi r^3 n(r)dr. \tag{2.15}$$

The integral in Eq. 2.15 is related to the mass concentration (Eq. 2.12). For Visible wavelengths, larger particles contribute negligibly to extinction, allowing us to focus on $PM_{2.5}$:

$$k_{ext} = \frac{3\langle Q_{ext} \rangle}{4\rho_{aer} r_{eff}} PM_{2.5}, \tag{2.16}$$

where we considered an average mass density ρ_{aer} for the aerosol mixture. We can invert this equation to obtain:

$$PM_{2.5} = \frac{4}{3} \frac{\rho_{aer} r_{eff}}{\langle Q_{ext,aer} \rangle} k_{ext}. \tag{2.17}$$

2.1.3 Mass-specific Extinction Coefficient

An alternative formulation can be derived by the definition of the Mass Extinction Coefficient (MEC) as the ratio between the Extinction Coefficient and the Mass Concentration (Wang et al., 2014; Hand and Malm, 2007). From Eq. 2.16:

$$m_{ext} = \frac{k_{ext}}{PM} = \frac{3\langle Q_{ext,aer} \rangle}{4\rho_{aer} r_{eff}}. \tag{2.18}$$

The MEC depends on the Refractive Index (RI), the PSD and the mass density ρ_{aer} of the aerosol mixture. It can be computed by Mie theory or estimated with empirical methods, for example by comparing light extinction measurements and PM with a linear regression (Hand and Malm, 2007). When assuming that the aerosol composition and PSD do not vary much during the time of measurement, the variability in MEC values is mainly due to change in ambient conditions (Hand and Malm, 2007; Wang et al., 2014).

A similar formulation from Ensor and Pilat (1971) defines the parameter K independent of mass density:

$$m_{ext} = \frac{k_{ext}}{PM} = \frac{1}{\rho K}. \tag{2.19}$$

Eq. 2.17 can be written as $PM = \rho K \cdot k_{ext}$ by using this formulation, so K can also be defined as:

$$K = \frac{4}{3} \frac{r_{eff}}{\langle Q_{ext,aer} \rangle}. \tag{2.20}$$

The theoretical value of K can be computed by Mie theory. K is primarily a function of the Effective Radius for $r_{eff} > 0.5\mu m$, while for smaller sizes it strongly depends on the imaginary part of RI (Jiang et al., 2019; Gnendiger et al., 2024). For example, Jiang et al. (2019) calculated the values of K for different types of single particle and found that K can differ by more than a factor of three for sizes smaller than $0.3\mu m$.

2.1.4 Linear Approximation

The Aerosol Optical Depth retrieved by remote sensing observations is related to the Extinction Coefficient by Eq. 2.3 and strongly depends on the vertical profile of $k_{ext}(z)$. As a first approximation, if the aerosol composition is homogeneous in the atmospheric column and the aerosols are confined in a layer of width H near the surface, the relationship with the PM measured within the layer is (Koelemeijer et al., 2006):

$$AOD = \int_0^H k_{ext}(z)dz \approx H \cdot k_{ext}(0) = H \cdot \frac{3 \langle Q_{ext,aer} \rangle}{4 \rho_{aer} r_{eff}} PM_{2.5}. \tag{2.21}$$

Secondly, AOD is retrieved at *ambient conditions* and the quantities in Eq. 2.21 depend on the ambient Relative Humidity (RH), while PM is measured at *dry conditions*, usually at controlled values of $RH < 40\%$. Hydrophilic aerosol particles grow in size by absorbing the ambient water vapour as a function of Relative Humidity (RH). As a result, the optical properties and the mass concentration are changed. A hygroscopic function $f(RH)$ is used to account for this mismatch. Not all aerosols are hydrophilic: for example, Black Carbon aerosols, widely present in the Po Valley, are hydrophobic when freshly emitted, and can become hydrophilic when organic or inorganic species condense onto them. Ultimately, the relationship between AOD and PM (as measured by typical monitoring stations) can be approximated as:

$$AOD \approx H \cdot \frac{3 \langle Q_{ext} \rangle}{4 \rho_{aer} r_{eff}} f(RH) PM_{2.5} \tag{2.22}$$

where all properties on the right hand are now considered at dry conditions and the hygroscopic growth is described by $f(RH)$.

Vertical Correction

It is apparent by writing Eq. 2.22 as:

$$PM_{2.5} \approx \frac{4\rho_{aer} r_{eff}}{3 \langle Q_{ext} \rangle f(RH)} \frac{AOD}{H} \tag{2.23}$$

that the maximum height of the aerosol level (H) can greatly change the coefficient between AOD and PM. First studies like Wang and Christopher (2003) and Koelemeijer et al. (2006) underline the need to rescale the total columnar AOD to the effective height of the aerosol layer.

This is especially important when considering the annual variation of the boundary layer height, where the majority of aerosols are trapped. Previous studies (e.g., Wang and Christopher (2003); Wang et al. (2009)) used the Planetary Boundary Layer Height (PBLH) as an estimate of the height H. However, a more precise definition is needed: the Mixing Layer Height (MLH) represents the actively mixed layer where aerosols are homogeneously distributed, which is the condition required by Eq. 2.21. During daytime convective conditions, the MLH is approximately equal to the PBLH, but during nighttime or stable conditions, the PBLH includes residual layers where mixing is suppressed. Therefore, the MLH is the more appropriate parameter for relating columnar AOD to surface $PM_{2.5}$. A detailed discussion of boundary layer structure and MLH determination methods is provided in Chapter 3. The MLH exhibits strong seasonal variation, being low during winter and high during summer.

During winter, aerosols are concentrated near the ground and the values of PM are higher, while in summer the aerosols are diluted and the respective PM values near the ground are lower. This is true especially in urban areas and in particular areas such as the Po Valley in Northern Italy (Ferrero et al., 2011). For example, Barnaba et al. (2010) and Ferrero et al. (2019) found that at least 80% of the total AOD refers to about the first km near the ground, and that AOD and PM measurements have a sort of "phase shift" during the year caused by the change in MLH.

Humidity Correction

Hygroscopic growth depends primarily on the chemical composition of aerosols (Hänel, 1981; He et al., 2015; Liu et al., 2013). Soluble aerosol types such as inorganic salts exhibit greater hygroscopic growth than organic compounds, soot and mineral aerosols. Aerosol size and mixing state also affect the hygroscopic

properties of the mixture. Different parametrizations of $f(RH)$ are available in the literature. Several studies relating satellite AOD and ground-based $PM_{2.5}$ through linear regression have employed the Hänel parametrization.

The Hänel parametrization was developed from light extinction measurements, specifically from scattering and absorption cross-sections measurements (Hänel, 1981). The enhancement of scattering and absorption is described by an empirical **growth function** defined as the ratio between k_{ext} at ambient conditions and at dry conditions (Randriamiarisoa et al., 2006; He et al., 2015):

$$f(RH) = \frac{k_{ext}(RH)}{k_{ext}(RH < 30\%)} = \frac{(1 - RH)^{-\gamma}}{(1 - RH_{ref})^{-\gamma}} \tag{2.24}$$

where γ is the Hänel growth factor and RH is between 0 and 1. RH_{ref} is the reference RH value for dry measurements, usually $RH_{ref} < 0.5$. In literature, several values of γ are available depending on aerosol type or source (eg. Liu et al. (2013); He et al. (2015)). In Italy, Di Nicolantonio et al. (2009) and Arvani et al. (2016) used empirical γ coefficients from Randriamiarisoa et al. (2006) for urban aerosols.

Alternate parametrizations have also been described for this type of studies. For example, Wang et al. (2009) and Wang et al. (2014) compared different forms of $f(RH)$ over several cities of China.

The effectiveness of hygroscopic corrections in the Po Valley remains uncertain. Both Ferrero et al. (2019) and Arvani et al. (2016) found that including the Hänel parametrization did not significantly improve correlation between MODIS AOD and ground-based $PM_{2.5}$ in this region. Several factors may explain this finding. The Po Valley aerosol mixture contains substantial hydrophobic components from traffic emissions, as noted in Chapter 1. This can reduce the overall hygroscopic response of the aerosol population. Additionally, satellite-retrieved AOD refers to the columnar RH that may not adequately represent surface-level humidity conditions throughout the year. The empirical γ coefficients derived for other urban areas may also not be appropriate for the specific aerosol composition and seasonal characteristics of the Po Valley.

In the present work, we try to exploit PM measurements at ambient RH to derive an empirical corrective function to describe the hygroscopic properties of local aerosols (see Section 3.3).

2.2 From Satellite AOD to Ground-based PM

A variety of methods have been successfully employed to estimate PM from satellite AOD. There is no definite answer to which of these methods could work best on a global scale: the performance of each method depends on the region characteristics,

the time period investigated, and the datasets used (Ma et al., 2021). It is largely advised to choose the appropriate methodologies according to the scope of the study, as well as the area of interest (Chen et al., 2019; Sorek-Hamer et al., 2020). For this reason, it is important to perform a brief review of the literature before choosing the methodology.

There are two main approaches to the problem. The **scaling approach** makes use of chemistry models that can simulate both the $PM_{2.5}$ and the AOD given a set of input variables. The parameter $\eta = \frac{PM_{2.5,sim}}{AOD_{sim}}$ is computed from the simulations, and the satellite-derived PM is computed as $PM_{2.5,sat} = \eta AOD_{sat}$. While this approach can be useful when ground measurements are not available, it also has higher prediction errors because it is not calibrated on empirical data: for example, it has issues in characterizing the correct aerosol distribution in space, time, and altitude (Liu et al., 2014; Ma et al., 2021).

The **statistical approach**, on the other hand, aims at training a statistical or machine learning model in order to extend the available PM measurements to nearby areas where satellite observations are present. Training a model requires a larger amount of data and it is not easily applicable in countries with a low number of monitoring networks. However, if a large amount of ground measurements is available, it can estimate PM with greater accuracy and full coverage over the study region (Ma et al., 2021). Statistical methods have also been applied to calibrate and improve the predictions of scaling approach models.

Additionally, several **semi-empirical methodologies** have been studied in literature (eg. Wang et al. (2009, 2014); Di Nicolantonio et al. (2009); Koelemeijer et al. (2006)). Such methodologies are based on the theoretical equations that link AOD and PM as described in the previous section and therefore are of great interest because of the physical significance with respect to other statistical models. For this reason, in the present work we investigate a semi-empirical methodology together with a statistical approach (linear model).

2.2.1 Statistical Approach

Several reviews summarize the main statistical methods employed in different regions of the world and for different purposes. Chu et al. (2016) provided a review of previous studies worldwide with a focus on the type of statistical models and their respective overall accuracy. Ma et al. (2021) provided a review of statistical models used for large-scale and long-term studies. Sorek-Hamer et al. (2020), on the other hand, focused on short-term pollution episodes at small scales.

The simplest statistical methods are linear or multi-linear regression. A linear regression model requires only AOD and few auxiliary variables for the training phase, but the measurements should be taken by spatial representative ground monitors. A linear model is not very accurate when the assumptions for the linear

approximation are not fulfilled: for example, if the aerosol is not confined in the mixing layer, or when the aerosol composition and PSD are not homogeneous in time and space. The average accuracy of this type of models is around ±30% (Hoff and Christopher, 2009).

Multi-linear models use AOD and a variety of auxiliary data to improve the correlation between AOD and PM. As seen in Section 2.1.4, the effective aerosol layer height H and Relative Humidity (RH) are the most important variables to include after AOD. Usually, a multi-linear model assumes a linear relationship between PM and each individual variable and does not account for possible interactions between the variables. A multi-linear model fails to capture complex relationships between variables, such as meteorological variables that are correlated or have a distinct seasonality (Chu et al., 2016).

The model coefficients usually vary in space and time. For this reason, it is not advised to use linear regression in case of long-term studies or when considering a large or heterogeneous region. However, the performance of the linear models improves when considering subsets of data that refer to one location and one season at a time. Chen et al. (2019) provided a comparison between different models in Europe. The models performed better for high pollution levels and high traffic areas. The Stepwise Linear Regressions (SLR) were the linear models that performed best. SLR models use a variable selection algorithm in which only the variables that are statistically significant are kept in the model at each step.

Linear Regression Linear regression was among the first applied methodologies to estimate $PM_{2.5}$ from AOD and it has been used for several years alongside more complex methodologies. Wang and Christopher (2003) compared ground-based $PM_{2.5}$ from EPA and satellite AOD retrieved by MODIS observations, found good values of positive linear correlation ($R^2 = 0.7$), and discussed the factors that most affect the linear AOD-PM relationship. In particular, the two most important factors are apparent from the previous derivation: the aerosol vertical profile described by the mixing height H and the aerosol hygroscopic properties described by the function $f(RH)$.

After the first study by Wang and Christopher (2003), several works applied linear regression methodologies using MODIS AOD in different regions, such as China, Europe, USA, and using datasets referred to one or two years, or even a decade. The R^2 of the resulting models varied from very poor results ($R^2 < 0.2$) to medium results (R^2 between 0.4 and 0.6), and few studies achieved good results ($R^2 > 0.7$). In the majority of cases, the correlations improved when considering data from the same location or region, or filtering by season (Chu et al., 2016).

The previous discussion demonstrates that Linear Regression is not recommended for finding global coefficients to estimate $PM_{2.5}$ from satellite AOD. More

complex and accurate methodologies have been widely used with good results. However, a study in which all variables in Eq. 2.23 can be estimated in a single location can successfully use a Linear Regression. This is the strategy that will be used further in the present work.

2.2.2 Study Definition

Several studies provide general recommendations for the application of a statistical methodology to a particular case study. In the following, we summarize some aspects to take into account when designing a study that involves the correlation of PM and AOD.

Variable selection

Statistical models typically require at least four datasets (Ma et al., 2021): the satellite AOD, the ground PM (daily or hourly time scale), meteorological variables (H and RH, but also other variables such as wind speed, temperature, precipitation) and ancillary variables that depend on the study area (land use information, traffic counts for urban sites, emissions).

Although AOD can be used as the only predictor (e.g. Gupta and Christopher (2008)), meteorological and ancillary variables improve the model especially for studies over larger regions (Ma et al., 2021). It is important to add variables that are physically significant. As seen in Section 2.1.4, ambient humidity influences the particle growth and the AOD needs to be rescaled according to the height of the aerosol layer. Moreover, wind speed and direction influence the spatiotemporal collocation of PM and AOD, while traffic and fire counts are associated with different types of emissions.

Aerosol type has only been considered in a few studies as part of the necessary datasets. Zheng et al. (2017) analyzed how the PM-AOD ratio $\eta = \frac{PM_{2.5}}{AOD}$ varied in China according to several factors; among them, they considered the aerosol types following the classification by Lee et al. (2010) based on AERONET measurements. This classification divides aerosols according to size (fine and coarse aerosols) and absorption properties (from not absorbing to highly absorbing aerosols). The coefficient η varied for different aerosol types during the year.

Ferrero et al. (2019) suggested the use of the PM values from the previous day as additional predictor for studies in Po Valley, to account for the PM accumulation in the region. This can be investigated by considering the autocorrelation function of PM.

The significance of each variable should be assessed in a separate step. This can be done by calculating several statistical parameters (such as the coefficient

of determination R^2, the Root Mean Square Error (RMSE), etc) and comparing their values when considering one variable at a time in the statistical model.

Data processing

When considering an extended study region, it is important to align the different datasets to a common grid. For point ground level data, the spatial and temporal representativeness compared to the grid and the satellite overpass times should be addressed (Sorek-Hamer et al., 2020). Ground-based sites are usually classified according to the distance to anthropogenic sources (e.g. industrial, urban, background, rural, remote, etc.). The vertical representativeness of data is also important as the aerosol vertical profile impacts the AOD in the atmospheric column (Ferrero et al., 2019).

Several spatial interpolation methods have been used in previous studies to align ground PM monitors to the satellite AOD grid. Satellite products usually have irregular grid cells according to the satellite overpass. Level 3 products are temporally averaged and re-gridded to a common 0.1° grid, while products such as MAIAC AOD (Lyapustin et al., 2018) are retrieved on a common grid with different spatial resolution.

Another issue of satellite AOD is the amount of missing data due to clouds and bright surfaces. A variety of statistical and machine learning algorithms have been used to improve the AOD coverage, for example by combining multiple satellite products (Ma et al., 2021).

Our Approach

The literature review presented in this chapter demonstrates that successful $PM_{2.5}$ estimation from satellite AOD requires careful consideration of regional characteristics and appropriate methodologies. Statistical approaches can achieve good correlations when trained on extensive datasets, but they provide limited insight into the physical processes governing the AOD-PM relationship. Scaling approaches based on chemical transport models avoid the need for ground-based calibration but suffer from uncertainties in simulating aerosol vertical distribution and composition. Semi-empirical methodologies, grounded in the theoretical framework developed in Section 2.1, preserve the physical basis of the AOD-PM relationship while incorporating observational data.

The Po Valley presents characteristics that make it particularly suitable for a physics-informed approach. As described in Chapter 1, winter atmospheric conditions favor aerosol trapping within a well-defined boundary layer (Barnaba et al., 2010; Ferrero et al., 2019). These conditions fulfil the assumption required by Eq. 2.21, where aerosols are confined to a layer of height H near the surface with

relatively homogeneous composition.

However, to implement the theoretical relationship in Eq. 2.23, several challenges remain. The uncertainties associated with hygroscopic corrections in the Po Valley, as discussed in Section 2.1.4, suggest that generic parametrizations may not adequately capture the behaviour of the local aerosol mixture. The substantial contribution from traffic emissions introduces hydrophobic components that complicate the application of empirical growth functions derived for other urban environments. Additionally, the aerosol optical properties ($\langle Q_{ext} \rangle$, r_{eff}, ρ_{aer}) in Eq. 2.23 are typically treated as unknown fitting parameters in statistical approaches or assumed from aerosol type classifications. A more rigorous approach would estimate these quantities from direct measurements of aerosol size distributions and composition.

The methodology developed in this thesis addresses these challenges by exploiting auxiliary measurements to constrain the physical parameters in Eq. 2.23 rather than relying on empirical fitting or generic assumptions. This physics-informed approach maintains explicit connections between measured quantities and theoretical predictions. Each term in the equation is either measured directly (AOD, $PM_{2.5}$, MLH) or derived from auxiliary observations of aerosol microphysical properties. The framework also enables sensitivity analysis to quantify how uncertainties in individual parameters affect $PM_{2.5}$ estimates, providing insight into the dominant sources of variability in the AOD-PM relationship specific to the Po Valley.

Chapter 3 characterizes the observational datasets required to implement this approach, including ground-based $PM_{2.5}$ measurements, satellite AOD retrievals, mixing layer height estimates, and aerosol microphysical measurements. Chapter 4 presents the complete physics-informed methodology and the resulting $PM_{2.5}$ estimates for the study region.

Chapter 3

Preliminary studies

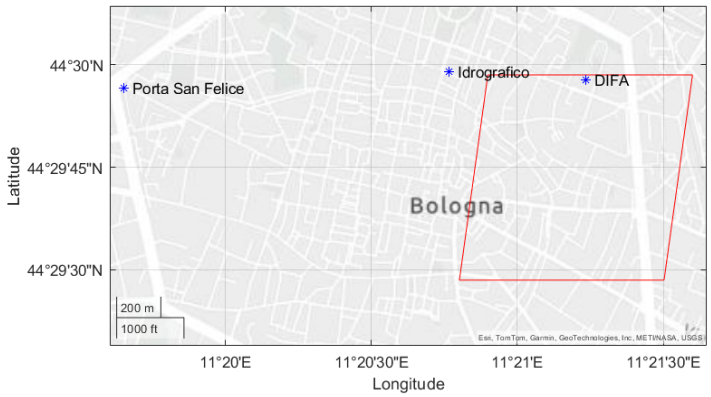

Figure 3.1: Locations of ground-based measurements (blue markers) and the chosen AOD cell (red box). Base map courtesy of Esri, TomTom, Garmin, GeoTechnologies, Inc, METI/NASA, USGS.

This chapter presents the observational datasets and preliminary analyses that form the foundation for the physics-informed AOD-PM methodology developed in Chapter 4.

The physics-informed approach requires three essential components: satellite-retrieved aerosol optical depth (AOD), ground-based $PM_{2.5}$ measurements, and auxiliary observations to constrain the aerosol microphysical and optical properties that link these quantities. As established in Chapter 2, the theoretical relationship between AOD and surface $PM_{2.5}$ (Eq. 2.23) depends on the mixing layer height (MLH), effective radius (r_{eff}), extinction efficiency ($\langle Q_{ext,aer} \rangle$), and mass density ($\rho_{aer}$) of the local aerosol mixture.

Firstly, we describe the primary dataset used to implement the methodology: satellite AOD from MODIS, particle number and mass measurements from

a Light Optical Aerosol Counter (LOAC), and mixing layer height from a co-located ceilometer. Auxiliary datasets are used for validation and interpretation, including meteorological observations, reference $PM_{2.5}$ measurements, and aerosol optical properties from AERONET.

Before applying the theoretical framework, several preliminary investigations are necessary. Section 3.2 characterizes the LOAC measurements throughout the study period (February-September 2023), examining how episodic events such as precipitation and desert dust transport affect particle size distributions, effective radius, and compositional properties. These events must be identified and excluded from the AOD-PM analysis to ensure the assumptions underlying Eq. 2.23 remain valid.

Section 3.3 investigates the relationship between ambient $PM_{2.5}$ and Relative Humidity to characterize hygroscopic effects in the study region. This analysis motivates a key methodological decision: directly relating satellite AOD (retrieved at ambient humidity) to LOAC $PM_{2.5}$ (measured at ambient humidity), thereby avoiding the need for hygroscopic corrections while enabling subsequent derivation of growth factors through comparison with dry reference measurements.

The chapter concludes with a discussion of dataset limitations and their implications for the physics-informed methodology presented in Chapter 4.

3.1 Datasets

In this section, we present all the data used in the present work. We distinguish between the dataset used for the application of our methodology and the auxiliary data useful for analysis and interpretation of results. Tables 3.1 and 3.2 summarise the instrumental setup, while Figure 3.1 shows the location of the ground-based stations and the satellite AOD grid cell. The main dataset consists of (Table 3.1):

- Satellite AOD obtained with MAIAC algorithm at 1 km x 1 km spatial resolution;
- Data measured by a LOAC operated under ambient conditions at the Department of Physics and Astronomy (DIFA) of the University of Bologna (lat: 44.499, lon: 11.354), including: $PM_{2.5}$, Particle Number (PN) concentration in 19 size bins (0.2-30 μm), and particle type classification;
- Mixing Layer Height (MLH) measured by a ceilometer co-located with the LOAC at DIFA.

Auxiliary data comprises (Table 3.2):

- Relative Humidity and Precipitation from the meteorological station Bologna Idrografico (lat: 44.499, lon: 11.346), located 0.6 km from DIFA;

- Daily reference "dry" $PM_{2.5}$ from ARPAE station Porta San Felice, measured using a TEOM instrument (lat: 44.499, lon: 11.328), located 2.1 km from DIFA;
- MLH obtained from radiosoundings performed at IGRA station San Pietro Capofiume (lat: 44.654, lon: 11.623), located 27 km from DIFA;
- Ångström Exponent (AE) from AERONET stations of Modena (lat: 44.629, lon: 10.948) and San Pietro Capofiume[1] (lat: 44.650, lon: 11.620), located, respectively, 35 and 27 km from DIFA.

Variable	**Source**	**Resolution**	**Location**
AOD (550 nm)	MAIAC/MODIS	1-4 day^{-1}, 1 km^2	Grid cell
$PM_{2.5}$, PN, type	LOAC	1 min, point	DIFA
MLH	Ceilometer CL31	16 s, 10 m vert.	DIFA

All data: February-September 2023.

Table 3.1: Main dataset used to apply the methodology.

Variable	**Station**	**Resolution**	**Distance**[a]
RH, Precipitation	ARPAE BI[b]	30 min / hourly	0.6 km
$PM_{2.5}$ (dry)	ARPAE PSF[c] (TEOM)	Daily ave.	2.1 km
MLH (validation)	IGRA SPC[d]	Daily (12:00 UTC)	27 km
Ångström Exp.	AERONET MO/SPC[e,d]	2 min	27-35 km

[a]From DIFA. [b]Bologna Idrografico. [c]Porta San Felice. [d]San Pietro Capofiume (IGRA and AERONET sites are not co-located). [e]Modena.

Table 3.2: Auxiliary data used for analysis and interpretation of results.

3.1.1 LOAC data

All OPC instruments are highly affected by high Relative Humidity, cloudy conditions, and precipitation events (eg. Crilley et al. (2018)). Recent studies recommend performing measurements with these sensors under low time resolutions (hourly and daily averages) and clean sky conditions (Brattich et al., 2020). Usually, a calibration function is needed to account for Relative Humidity and Temperature, especially when the instruments are operated at ambient conditions (Brattich et al., 2020; Gualtieri et al., 2024; Karagulian et al., 2019).

[1]The IGRA and AERONET sites in San Pietro Capofiume are not co-located.

Size Bin	Bin Edges (μm)	Bin Center (μm)	Size Class
1	0.2–0.3	0.25	
2	0.3–0.4	0.35	1
3	0.4–0.5	0.45	
4	0.5–0.6	0.55	
5	0.6–0.7	0.65	2
6	0.7–0.85	0.775	
7	0.85–1	0.925	
8	1–2	1.5	3
9	2–3	2.5	
10	3–5	4	
11	5–7.5	6.25	
12	7.5–10	8.75	4
13	10–12.5	11.25	
14	12.5–15	13.75	
15	15–17.5	16.25	5
16	17.5–20	18.75	
17	20–22.5	21.25	
18	22.5–25	23.75	6
19	25–30	27.5	

Table 3.3: LOAC size bin definition and classification scheme. Size bins are grouped into six size classes for particle type identification.

Particle Type	Droplet	Salt	Mineral	Carbon
Absorption[a]	Transparent	Low	Medium	High
Mass density (g/cm^3)	0[b]	2.2	2.2	1.6

[a]Absorption classification at 650 nm wavelength based on scattering angle ratios.
[b]Water droplets are excluded from PM calculations.

Table 3.4: Mass density values used by LOAC algorithm for each particle type classification. These values are applied to compute PM_1, $PM_{2.5}$, and PM_{10} from particle number concentrations.

The LOAC (Light Optical Aerosol Counter), presented in Renard et al. (2016), retrieves the Particle Number (PN) concentration (cm^{-3}) in 19 size bins for particle diameters between 0.2 and 30 μm (Table 3.3) using laser beams at 650 nm wavelength.

By using two scattering angles (12° and 60°) it also determines the degree of absorption of the detected particle, from transparent to highly absorbing (at 650 nm). This estimate is used to classify the particles, divided in six size classes (Table 3.3) and in four types:

- droplet: transparent particles,
- salt: lowly absorbing particles,
- mineral: medium absorbing particles,
- carbon: highly absorbing particles.

From the PN measurements and the particle type, the PM_1, $PM_{2.5}$, and PM_{10} ($\mu g/m^3$) are estimated with an internal algorithm that uses a suitable value of particle mass density (g/cm^3) according to particle type (Table 3.4).

LOAC data is available from February to September 2023. The 1-minute dataset, including $PM_{2.5}$ and PN, is screened with a Hampel filter on a 10-minute window (Liu et al., 2004) to remove outliers.

PN is an approximation of the PSD calculated within the size bin edges:

$$PN_i \approx \int_{r_i}^{r_{i+1}} n(r)dr \quad i = 1, ..., 19 \tag{3.1}$$

where r_i and r_{i+1} are half the values of the bin edges for size bin i (see Table 3.3). By inverting Eq. 3.1, we can calculate an estimate of the PSD, dividing each PN_i by the half width of the corresponding size bin i:

$$n_i \approx \frac{PN_i}{\Delta r_i}, i = 1, ..., 19 \tag{3.2}$$

where $\Delta r_i = r_{i+1} - r_i$.

We use the 1-minute PN data to compute r_{eff} with a discretized equation based on Eq. 2.8:

$$r_{eff,LOAC} \cong \frac{\sum_i PN_i R_i^3}{\sum_i PN_i R_i^2} \quad i = 1, ..., 19. \tag{3.3}$$

Lastly, the particle type information is aggregated hourly with a statistical approach, as advised in Renard et al. (2016). We aggregate the 1-minute particle

type classification in hourly counts of each type x ("droplet", "salt", "mineral", "carbon") and each size class j (from 1 to 6), and calculate the Number Ratio as:

$$NR_{j,x} = \frac{counts_{j,x}}{counts_{j,tot}} \tag{3.4}$$

where $counts_{tot}$ is the total number of identified particles for each size class in an hour.

For a given size class, the Number Ratios represent the average aerosol composition in terms of fraction or percentage of each particle type.

3.1.2 Satellite AOD

AOD is one of the main aerosol optical parameters retrieved by several satellite instruments, alongside the Ångström Exponent and Fine Mode Fraction (Shin et al., 2019; Wei et al., 2019). Depending on each instrument wavelength range or sensor type, different algorithms have been developed to retrieve the AOD.

Over half the literature on the estimation of PM from satellite AOD has used AOD retrieved from MODIS (Moderate Resolution Imaging Spectroradiometer) (Shin et al., 2019) because of the longer operational period (MODIS Terra from 1999 and MODIS Aqua from 2002). However, the satellites Terra and Aqua have ended their designed lifespan, and other reliable satellite AOD should be used in the future. Several algorithms have been developed to retrieve AOD from MODIS data. The operational algorithms are presented in Levy et al. (2013). A newer operational algorithm, MAIAC (Lyapustin et al., 2018) retrieves AOD on land at high spatial resolution. In the present work, we choose MAIAC AOD for the correlation with PM for several reasons.

MAIAC AOD is retrieved at 550 nm from MODIS observations at high spatial resolution (1 km x 1 km) on a fixed grid. It has a better performance over bright surfaces compared to other algorithms and has been previously applied over urban areas (Qin et al., 2021). In case of anthropogenic aerosols, AOD below 0.12 can be overestimated. AOD uncertainty indicated in the product files is related to surface brightness. A value below 0.05 allows the algorithm to perform a standard retrieval (Rogozovsky et al., 2023; Qin et al., 2021). A 5% uncertainty value can be used for the single retrieval value. More information on the retrieval can be found in Lyapustin et al. (2018). Intense pollution cases in urban areas within the Po Valley, especially in very high polluted cities such as Milan and Turin, can be sometimes interpreted as clouds and filtered out (Arvani et al., 2016).

Co-location of AOD and ground-based data at DIFA site is performed on the fixed grid used in MAIAC retrievals. The cell containing the DIFA location is selected (Figure 3.1). This grid cell refers to the innermost part of Bologna historical centre, characterised by medium-bright surfaces, traffic and low industrial

emissions. The AOD data is acquired for the whole period covered by the LOAC dataset (February-September 2023). AOD is retrieved only in the absence of clouds over the grid cell, so the number of missing data over the year varies according to the number of cloudy days and precipitation events. The total number of satellite overpasses in the study period is 985, but only 26.8% is characterized by a successful AOD retrieval. The available retrievals are few during April and May (15-16%) and more frequent in August (41%).

Considering the AOD retrievals co-located with LOAC measurements, AOD uncertainty due to surface brightness is lower than 0.045 with a median of 0.016, and AOD values are lower than 0.45 with a median of 0.14. This means that the retrievals used in the following analysis are computed with the standard algorithm, and likely not affected by underestimation.

3.1.3 Mixing Layer Height

In Eq. 2.21, it is assumed that the aerosols are well mixed and confined in a layer of height H. In the following section, we briefly present the structure of the lower part of the troposphere and define the possible ways to identify such layer in the case of urban areas. Lastly, we present which datasets we will use further in the present work.

The Planetary Boundary Layer (PBL) is the atmospheric layer directly influenced by surface processes such as convection, turbulence, surface friction, etc. The PBL Height (PBLH) defines the separation between the PBL and the free troposphere (Stull, 2012). During the day, aerosols and other pollutants are dispersed inside the PBL due to turbulent mixing processes and are constrained in the PBL due to the lower turbulent mixing in the free troposphere above (Hayden et al., 1997). In this case, there is a strong gradient in the vertical aerosol concentration at the PBLH level, and the Mixing Layer (ML), that is the layer in which the aerosols are well-mixed, is almost identical to the PBL. There is still an "entrainment" zone where air from the free troposphere interacts with that inside the PBL. This is why in some works, the PBLH is used as a substitute of the ML Height (MLH).

During the night the turbulence decreases, leading to the formation of a lower ML near the surface and a Residual Layer (RL) above, characterized by reduced mixing. In this case, the vertical aerosol concentration presents at least two gradients and the PBLH corresponds to the height of the Residual Layer. During the transition periods of early morning and evening, it is difficult to determine the PBLH with accuracy because of the rapid changes in the vertical gradients (Dang et al., 2019; Stull, 2012).

The determination of the PBLH and the MLH and their difference during the day is of great importance for the study of the surface concentration of aerosols and

other pollutants (Liu et al., 2022). The 70% of AOD globally is related to aerosols within the PBL (Bourgeois et al., 2018). During the night, a large fraction of aerosols remains in the RL, leading to the formation of PBL aerosols the following day (Liu et al., 2020; Shi et al., 2020).

Moreover, the relationship between AOD and PM near the ground depends on the MLH. Variations in aerosol vertical distribution deeply influence the AOD-PM relationship and as such, it is important to monitor the variation of MLH on a yearly scale.

A variety of techniques can be used to estimate the PBLH and MLH. Radiosoundings are the most common methodology, with generally long datasets worldwide. Radiosondes measure the vertical profiles of temperature, humidity, pressure, and wind speed with high precision, and provide indirect estimates of the MLH. However, radiosondes are highly vulnerable to wind speed and direction and are generally launched only once or twice a day (Liu et al., 2019).

Remote sensing methodologies have been considered a valid alternative in the past decades due to the possibility of a continuous operation and consequently a high temporal resolution. Lidar (LIght Detection And Ranging) techniques are widely used worldwide and provide vertical aerosol profiles with high temporal resolution and wide spatial coverage, as several lidar networks have been established worldwide (Liu et al., 2019).

Lidar instruments emit a laser beam at fixed wavelength (in the UV, VIS or Near IR range) and detect the light backscattered by the atmosphere at different heights in the form of Range-Corrected Signal (RCS) which is converted in backscatter and extinction coefficient profiles. The PBLH can be derived with the assumption that the backscatter signal has a strong negative gradient at the PBLH level, and that the entrainment zone between the ML and the free troposphere is represented as significant temporal variations in the lidar signal (Liu et al., 2019; Melfi et al., 1985; Munkel et al., 2006; Hooper and Eloranta, 1986). Ceilometers are also widely used because of their compact size and lowered costs compared to conventional lidar instruments (Julaha et al., 2024). Their measurement principle is the same as lidar (Munkel et al., 2006).

One of the simplest methods for estimating PBLH from lidar or ceilometer measurements is the gradient method, in which the MLH is estimated as the height of the greatest negative gradient in the aerosol backscatter signal. In reality, the backscatter profiles are complex and more than one strong gradient is present, so this method requires a robust way to choose the "right" value of MLH (Liu et al., 2022; Eresmaa et al., 2012).

Satellite observations can also be used to estimate the PBLH. For example, the CALIPSO (Cloud-Aerosol Lidar and Infrared Pathfinder Satellite Observations) satellite mission was designed to provide vertically resolved measurements

of aerosols and clouds (Winker et al., 2010). The lidar instrument CALIOP (Cloud-Aerosol Lidar with Orthogonal Polarization) is the primary instrument on board of CALIPSO and it could identify aerosol and cloud layers and their optical and microphysical properties (Winker et al., 2009). CALIPSO retrievals have been validated with ground-based lidar measurements in different atmospheric conditions (e.g., Mamouri et al. (2009); Tesche et al. (2013); Mioche et al. (2010)). However, the CALIPSO mission has ended on August 2023 (Winker, 2025).

Lastly, reanalysis models provide estimates of PBLH by assimilating a great number of observational and modelling data. ERA5 is a fifth-generation ECMWF reanalysis model produced by the Copernicus Climate Change Service (C3S). The definition of the PBLH provided by the model corresponds to the MLH, and it is confirmed by analyses such as in Julaha et al. (2024). Reanalyses tend to underestimate the MLH during summer and overestimate it during winter. Among the different reanalysis datasets, ERA5 generally aligns more closely with ceilometer observations, even though some diurnal variability processes are still poorly represented (Julaha et al., 2024).

Determination of the MLH dataset

A Vailsala CL31 ceilometer mounted on the rooftop of DIFA provides continuous measurements of the backscatter signal profile up to 7.5 km, with vertical resolution of 10 m and temporal resolution of 16 s (Munkel et al., 2006). The instrument's internal algorithm applies the gradient method to detect MLH from local minima in the vertical gradient of the backscatter coefficient.

The ceilometer reports up to three potential MLH values per profile, which we refer to as Level 1, 2, and 3 from lowest to highest altitude. These represent the most prominent negative gradients in the backscatter profile, corresponding to different atmospheric layer boundaries. Level 1 typically represents the MLH during the day and the nocturnal boundary layer (as in Liu et al. (2022)); level 2 often corresponds to the nocturnal residual layer; level 3, if present, may indicate additional elevated layers due to a complex aerosol stratification. In presence of low-level clouds and during precipitation, the reported Levels do not represent the true MLH. The challenge is to select which level best represents the daytime mixing layer height to relate AOD to the surface $PM_{2.5}$. To establish selection criteria, we compared ceilometer-derived MLH values with independent radiosonde measurements from the nearest IGRA (Integrated Global Radiosonde Archive) station (Durre et al., 2006, 2018) at San Pietro Capofiume (SPC) (lat: 44.654, lon: 11.623), located 27 km from DIFA. SPC radiosondes data spans over 30 years of measurements (1986-present); the radiosoundings are usually performed at 12:00 UTC (daytime).

The structure of the MLH varies during the day, and satellite overpasses cor-

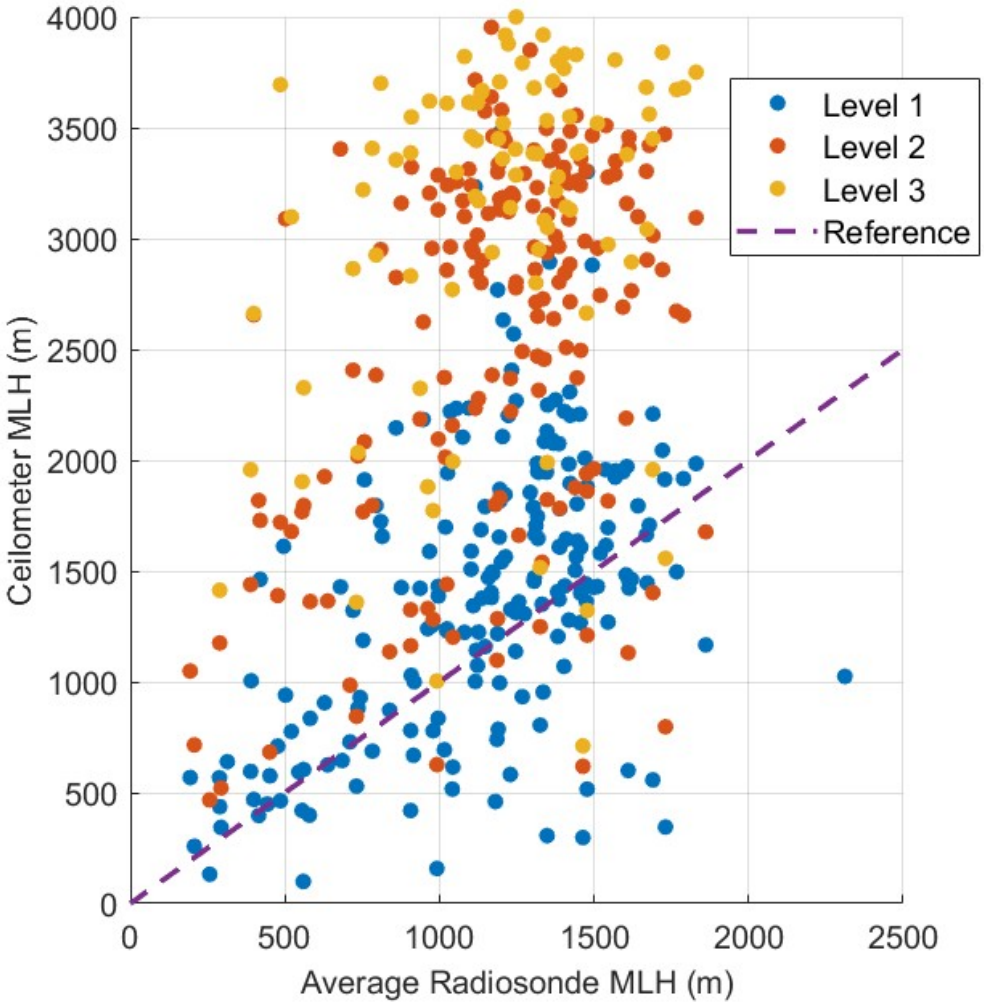

Figure 3.2: Comparison of the average hourly MLH at 12:00, between reference IGRA radiosonde and ceilometer data (levels 1, 2 and 3). The dashed line represents a perfect agreement between the two.

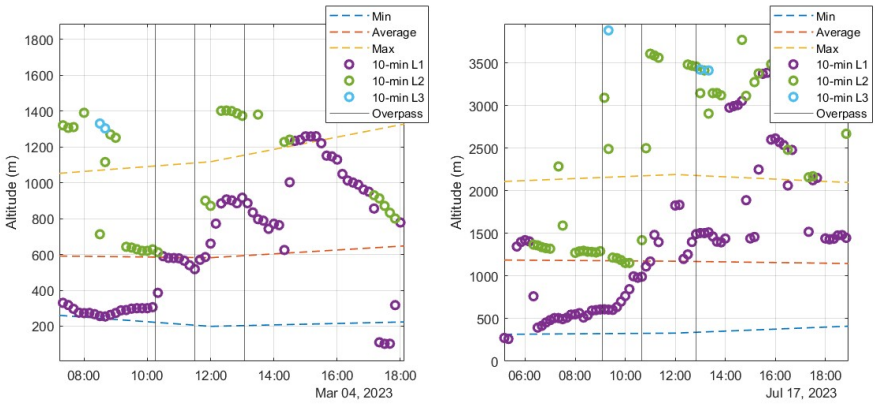

(a) (b)

Figure 3.3: Diurnal evolution of ceilometer-derived MLH on two representative days: (a) March 4, 2023 (cold season) and (b) July 17, 2023 (warm season). Colored dots show 10-minute averages for the three ceilometer levels (L1, L2, L3). The dashed lines represent the 2020-2025 average, minimum, and maximum radiosonde MLH at 12:00 UTC for each calendar day, linearly interpolated between consecutive days for comparison with ceilometer measurements. Vertical lines mark satellite overpass times.

respond to different vertical stratification. In the first hours of the day, when the MLH is not fully formed, L1 and L2 represent the stable nocturnal layer and the residual layer respectively. In Figure 3.2, we compare hourly-averaged ceilometer MLH (all three levels) and radiosonde MLH (average of 2020-2025 data for each calendar day), both at 12:00 UTC. At this hour, the diurnal MLH is formed and is best represented by L1 (Pearson's linear correlation coefficient R = 0.5). L2 and L3 correspond to elevated layers and systematically overestimate MLH (R = 0.44 and 0.26, respectively).

To select the appropriate MLH value for each satellite overpass, we calculated the 2020-2025 average MLH from radiosonde data for each calendar day and the relative standard deviation. For each satellite overpass time, we systematically identified the ceilometer data (L1, L2 or L3) whose 10-minute average is closest to the average MLH. Figure 3.3 illustrates two representative cases, comparing radiosonde (linear interpolation of measurements at 12:00 UTC) and ceilometer data (10-minute averages): Marth 4th (cold season) and July 17th (warm season). In both cases, in the early morning there is a clear distinction between the stable layer (represented by L1), closer to the surface, and the residual layer (represented by L2). The first level gradually mixes during the day and the MLH values become closer to the radiosonde average at 12:00. The selection algorithm chooses the

ceilometer level closest to the climatological reference: L2 for early overpasses when the residual layer dominates, transitioning to L1 as the convective boundary layer develops.

3.1.4 Auxiliary data

In this work, we also use quality-proofed data from the local environmental agency (ARPAE) (ARPAE, 2025): 30-minute Relative Humidity and hourly Precipitation Rate are measured from the closest meteorological station, Bologna Idrografico (lat: 44.499, lon: 11.346), located 0.62 km from DIFA; daily "dry" $PM_{2.5}$ from ARPAE Porta San Felice station (lat: 44.499, lon: 11.328), located 2.1 km from DIFA. In Figure 3.1 the stations are shown alongside DIFA and the AOD cell from satellite. The reference $PM_{2.5}$ is measured with a TEOM instrument.

Lastly, we use data from AERONET (AERONET, 2025), a global network of ground-based sunphotometers that measure AOD and related variables (Holben et al., 1998). AERONET nearest stations are in the urban area of Modena (lat: 44.629, lon: 10.948) and in the rural area of San Pietro Capofiume (lat: 44.650, lon: 11.620).

3.2 LOAC Data Analysis

In the following, we analyse the LOAC dataset of PN, $PM_{2.5}$, Effective Radius, and particle type. We examine how meteorological conditions during the measurement period impacted these variables and discuss the implications for aerosol optical properties.

The period considered in this study (February-September 2023) was characterized by particular variability in the meteorological conditions affecting the study area.

The month of May 2023 was affected by three severe rainfall events (May 2, 16, and 17), with cumulative daily rainfall values higher than 100 mm registered by the Bologna Idrografico meteorological station. Other minor rainfall events occurred throughout the measurement period. Desert dust intrusions were frequent during the months of June and July. Data from AERONET nearest stations of Modena and San Pietro Capofiume highlight that, during that time, the Ångström exponent α was below 0.5 in June and below 0.6 in July. Low values of α are associated with desert dust transport which is frequent in Italy during summer, with dust plumes that also reach the Po Valley and Bologna (Mazzola et al., 2010).

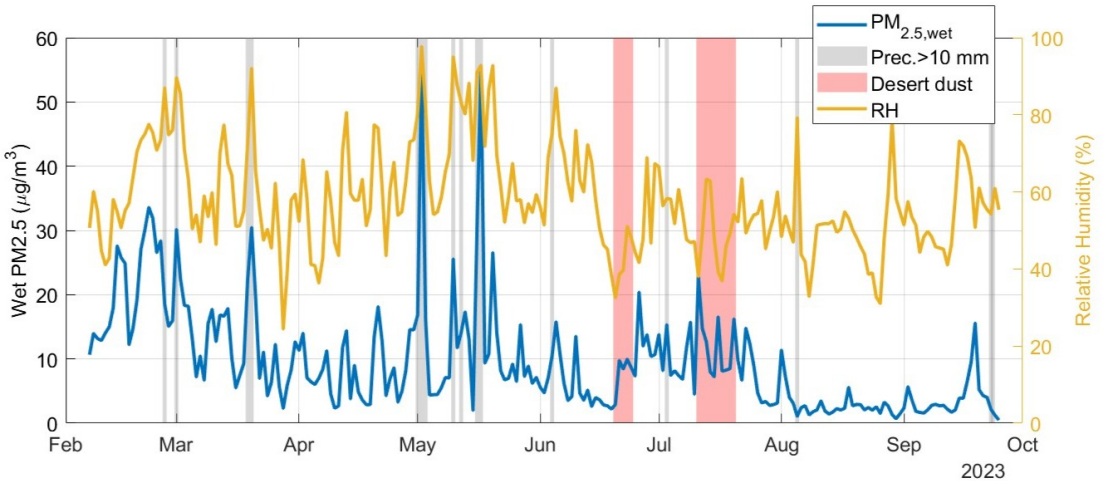

Figure 3.4: Daily "wet" $PM_{2.5}$ from LOAC (blue line) and daily RH from Bologna Idrografico (yellow line). Grey areas refer to days with total precipitation higher than 10 mm and red areas to desert dust transport.

3.2.1 $PM_{2.5}$ and Particle Number Variability

Figures 3.4 and 3.5 show how these meteorological conditions affected the LOAC measurements. Figure 3.4 shows the daily $PM_{2.5,wet}$ and the corresponding daily RH from Bologna Idrografico. Precipitation events with total rainfall greater than 10 mm are highlighted in grey, while desert dust transport cases are highlighted in red.

As noted in Brattich et al. (2020), LOAC measurements are affected by the hygroscopic growth of particles under precipitation events and high RH conditions. This is apparent from the daily values of $PM_{2.5}$ recorded during the study period, which are all below 35 $\mu g/m^3$ except for observation records during precipitation events, in which $PM_{2.5,wet}$ reaches values above 50 $\mu g/m^3$. As the algorithm for the PM calculation excludes particles identified as water droplets, these values correspond to aerosol particles grown in size due to high RH.

Figure 3.5 shows the daily cumulative PN in the first four size ranges used by the LOAC for the classification of particle types. The fifth and sixth ranges show the same behaviour as the fourth, so they are not shown. In these plots, too, we highlight in grey and in red respectively the precipitation events with total rainfall greater than 10 mm and the desert dust intrusions.

All size ranges are affected by precipitation events, as visible from the spikes in PN concentration during the grey-highlighted periods. Desert dust intrusions appear to affect mostly the first two size ranges (particles with diameters between 0.2 and 0.9 μm). This is because desert dust transport over the study area mainly

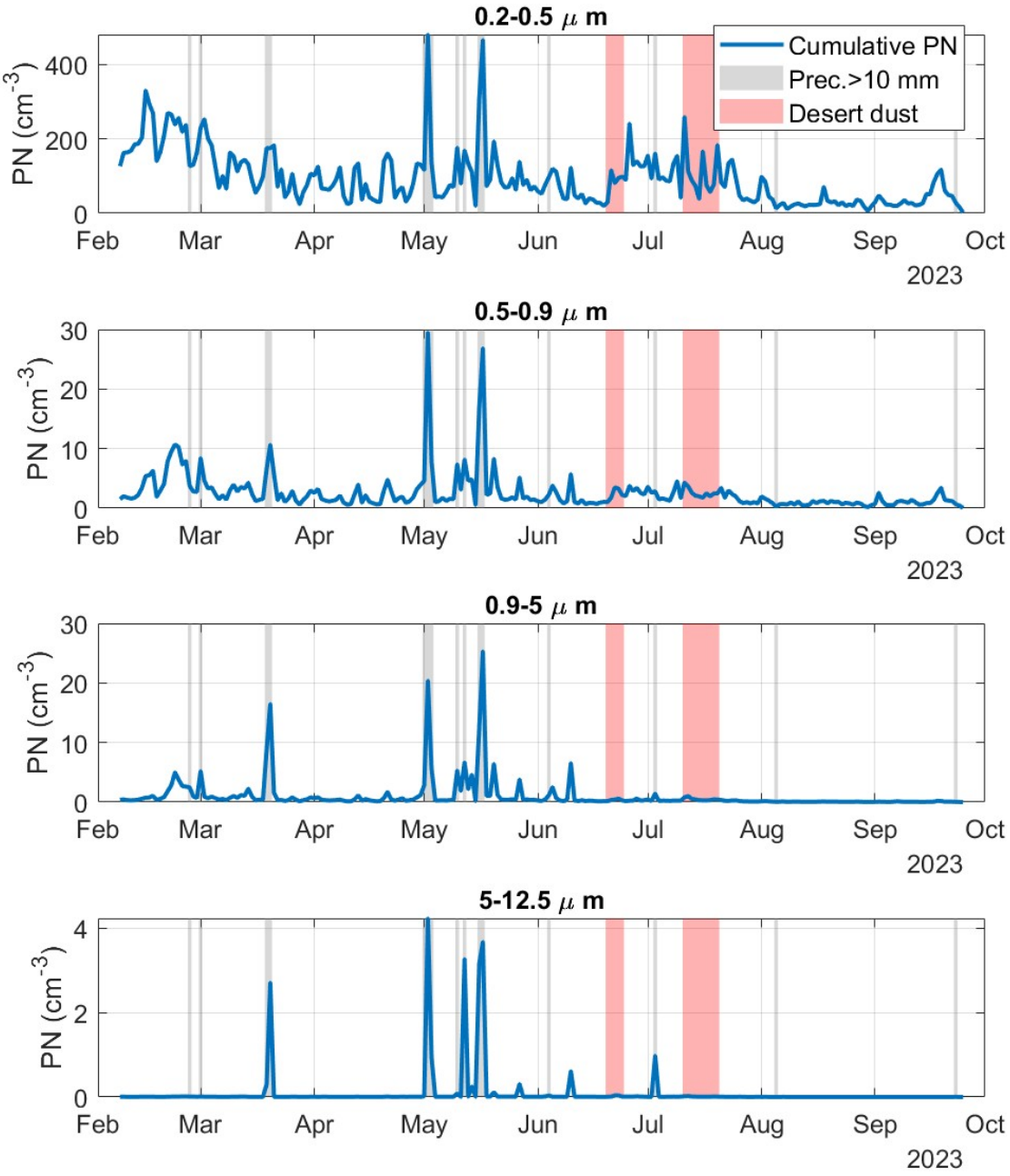

Figure 3.5: Daily PN in the size ranges used for the classification of particle types. The grey areas represent precipitation events with total rainfall greater than 10 mm, while the red areas correspond to desert dust transport.

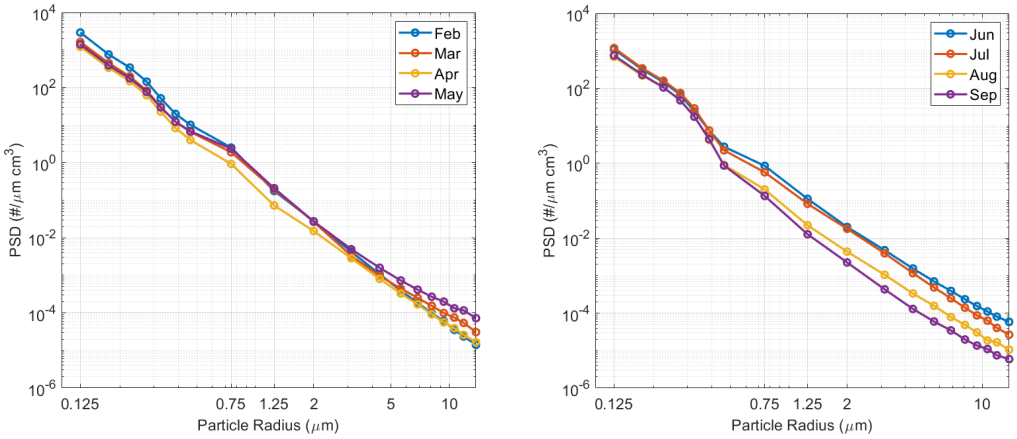

(a) (b)

Figure 3.6: Monthly PSD averages from LOAC PN measurements (logarithmic scales for x and y axis). (**a**) February to May. (**b**) June to September. A clear increase in particles with radius greater than 1 μm is observed during June and July compared to other months, corresponding to desert dust intrusion periods.

occurs at high altitude and is detected by columnar measurements such as α. Only a fraction of desert dust ends up being trapped and mixed within the PBL. The relatively modest increase in coarse particle concentrations at the surface, compared to the strong columnar signal, reflects several processes (Huang et al., 2019; Mazzola et al., 2010): gravitational settling removes larger particles during long-range transport and limits their residence time near the surface; stable stratification above the mixing layer can inhibit efficient downward mixing of elevated dust layers; and long-range dust transport from source regions such as the Sahara preferentially carries particles in the accumulation and fine coarse modes (0.1-5 μm), while the coarsest particles (>10 μm) deposit closer to source regions.

3.2.2 PSD, Effective Radius and particle type

Figure 3.6 shows the monthly average PSDs during the measurement period. The change in PSD shape due to higher concentrations of large particles is visible from the monthly averages. During June and July (Figure 3.6b), there is a clear increase in particles with radii greater than 1 μm compared to the distributions during February-May (Figure 3.6a).

Figure 3.7 shows the daily Effective Radius throughout the measurement period, with the same precipitation and dust transport events highlighted as in the previous figures.

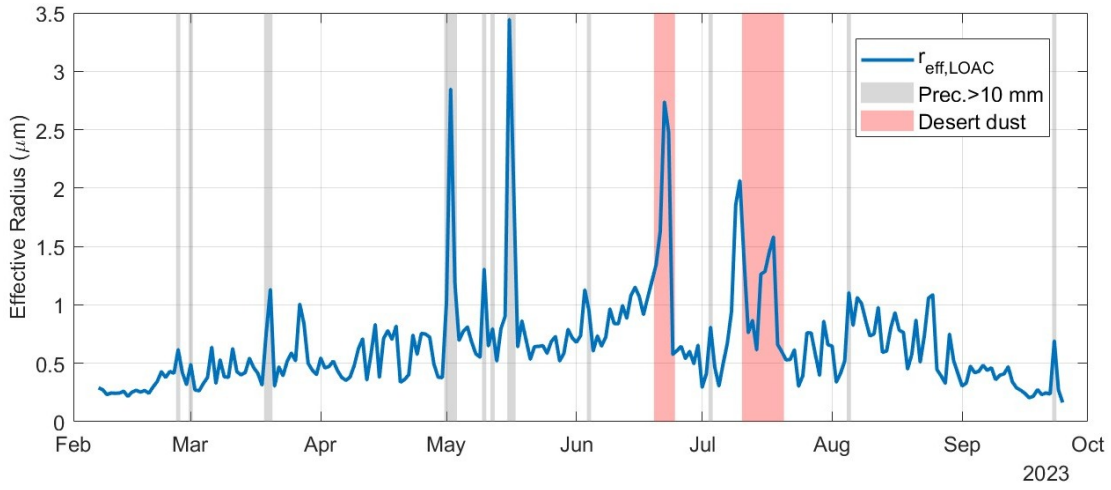

Figure 3.7: Daily Effective Radius computed from PN data. The grey areas refer to days with total precipitation greater than 10 mm, while the red areas correspond to desert dust transport.

Under typical conditions (excluding precipitation and dust events), the Effective Radius is constantly smaller than than 0.6 μm during the measurement period, reflecting the dominance of accumulation-mode particles characteristic of urban aerosol pollution. There is no clear seasonal trend in background r_{eff} values.

During precipitation events, r_{eff} shows values larger than 2 μm on May 2 and May 16, corresponding to the days with the highest rainfall. These elevated values result from hygroscopic growth of particles at very high RH conditions. The calculated hourly averages of r_{eff} have an uncertainty of 20% on average, while during precipitation and desert dust events uncertainties are always higher than 50% because of strong fluctuations within the hour.

During desert dust intrusions, r_{eff} shows values higher than 1.5 μm between June 19-22, and July 9-11 and 15-18, consistent with the AERONET data indicating low Ångström exponent during these periods. The moderate r_{eff} increase during dust events (compared to precipitation events) confirms that only a fraction of the dust column detected by AERONET mixes down to the surface level where the LOAC samples.

Figure 3.8 shows the monthly Number Ratios. Only the first three size ranges are shown, consisting of particles with diameters between 0.2 and 5 μm. Particles in the fourth size range (5-12.5 μm) consist of water droplets or unidentified types. Particle types in the two largest size ranges (12.5-40 μm) are mostly not identified due to measured PN concentrations lower than 0.01 cm^{-3}.

The "salt" type (in red) dominates in the first size range (0.2-0.5 μm, Figure

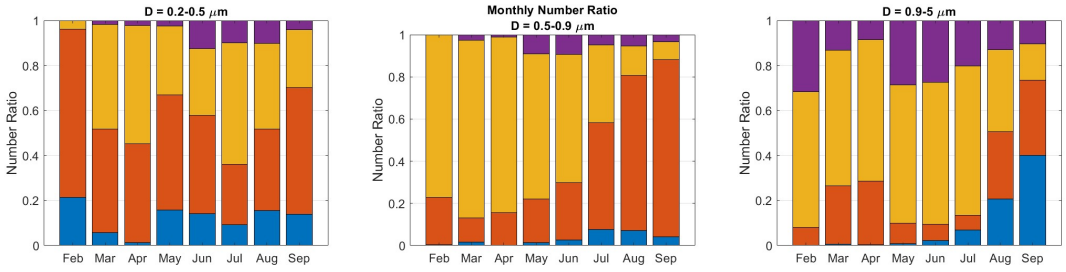

(a) $0.2 - 0.5\mu m$ (b) $0.5 - 0.9\mu m$ (c) $0.9 - 5\mu m$

Figure 3.8: Monthly Number Ratio of the detected particle types in the first 3 size classes. Blue = droplet, Red = salt, Yellow = mineral, Purple = carbon.

3.8a), with values of NR between 40% and 70% throughout the measurement period, while the "mineral" type (in yellow) ranges between 30% and 50%, with higher values in April and July. The "carbon" type accounts for less than 15%, and there is a consistent presence of droplets throughout the period, with values less than 15% except during February (20%) and April (almost absent).

In the second size range (0.5-0.9 μm, Figure 3.8b), the "mineral" type is dominant with NR between 60% and 80% from February to June. From July onward, the "salt" type increases and reaches NR values between 40% and 90%. The "carbon" type is present for less than 10%. Water droplets account for less than 10%, with minimal presence during February and April.

Lastly, in the third size range (0.9-5 μm, Figure 3.8c), the "mineral" type is the most common, with NR always greater than 50% apart from September, when water droplets rise to 40%. The "salt" and "carbon" types account for the remaining 10-25% in varying relative fractions.

Despite the seasonal variability in particle type ratios, the broad compositional categories remain relatively stable throughout the year, suggesting that the aerosol mixture in Bologna contains substantial fractions of both hygroscopic inorganic components and absorbing carbonaceous material. This compositional information is crucial to estimate the local aerosol optical properties, as explained in the next Chapter.

3.2.3 Discussion

The strong sensitivity of LOAC measurements to both precipitation and desert dust events has important implications for the AOD-$PM_{2.5}$ analysis presented in Chapter 4.

Days with precipitation events are excluded from the AOD-$PM_{2.5}$ analysis in Chapter 4. Not only is AOD not retrieved during rainy days due to cloud cover,

but the $PM_{2.5}$ values are highly affected by hygroscopic growth and wet removal processes. The sudden increases in both $PM_{2.5,wet}$ (Figure 3.4) and r_{eff} (Figure 3.7) during precipitation events are uncorrelated to increase in AOD, and confirm that these conditions are non-representative of a typical AOD-PM relationship.

Days with $r_{eff} > 1$ μm indicate the presence of coarse particles from dust transport. The AOD during these events is the sum of near-surface AOD, correlated with surface-level $PM_{2.5}$, and higher-altitude AOD due to elevated dust layers, which is uncorrelated with surface PM. In our study, we are unable to separate the two contributions (for example, by calculating height-dependent AOD from aerosol extinction profiles). This is why we also exclude dust transport days from the AOD-$PM_{2.5}$ analysis in the next Chapter. The particle type analysis (Figure 3.8) shows increased "mineral" fractions during June-July, providing independent confirmation of dust presence that complements the r_{eff} and AERONET Ångström Exponent data.

The Effective Radius uncertainty provides a useful quality control flag for identifying periods with rapid changes in aerosol composition. High r_{eff} uncertainties (>30%) indicate unstable conditions, for example in the case of dust intrusion episodes. In the analysis presented in Chapter 4, we apply uncertainty thresholds to select only data with stable aerosol properties suitable for establishing a reliable AOD-$PM_{2.5}$ relationship.

These episodic events, while complicating the analysis, demonstrate the value of continuous OPC measurements in identifying periods when standard AOD-$PM_{2.5}$ relationships may not be valid. Moreover, LOAC auxiliary data (PN, r_{eff}, particle type) enable the calculation of the key parameters needed to establish a physics-based relationship between AOD and $PM_{2.5}$ in Chapter 4.

3.3 Variation of PM with RH

In this section, we analyze the variation of LOAC $PM_{2.5}$ with ambient humidity to characterize hygroscopic effects and assess the feasibility of deriving a hygroscopic correction function for the study area. Understanding the $PM_{2.5}$-RH relationship is important for two reasons: (1) it helps interpret the differences between ambient ("wet") $PM_{2.5}$ measured by the LOAC and standard dry $PM_{2.5}$ measurements, and (2) it provides insight into aerosol composition and water uptake behaviour, which influence both PM mass and aerosol optical properties.

3.3.1 Seasonality of PM and RH

We begin by analyzing the seasonal and diurnal variability of LOAC $PM_{2.5,wet}$ and ambient Relative Humidity measured at the Bologna Idrografico meteorological

station. Figure 3.9 shows the monthly hourly variation of $PM_{2.5,wet}$ and RH (left panels) together with the respective monthly averages for the entire measurement period (right panels).

Seasonal Patterns

The monthly averages reveal distinct seasonal trends. RH exhibits a clear seasonal cycle with higher values in February (around 60%) and gradually decreasing in the summer, with August having the lowest monthly value (50%). The anomalously high RH during May (around 70% in monthly average and higher than 80% in the early morning) results from the severe rainfall events that affected the Emilia-Romagna region, as discussed in Section 3.2.

$PM_{2.5,wet}$ shows a pronounced decrease from February (monthly average ∼20 $\mu g/m^3$) to April (∼10 $\mu g/m^3$), followed by relatively stable values until September. This seasonal pattern reflects the combined influence of (1) emission changes, with the reduction of residential heating emissions as temperatures increase; (2) meteorological conditions, as the shallow, stable winter boundary layers transition to deeper, more turbulent spring/summer conditions; (3) temperature-dependent chemical processes enabled with higher temperatures during summer (such as evaporation of semi-volatile species); (4) wet removal during the frequent precipitation during spring and summer.

Diurnal Patterns

To quantify the diurnal variation systematically, we calculate the relative deviation of each hourly value from its 24-hour moving average:

$$Dif_{PM}(h) = \frac{PM(h) - PM_{24h}}{PM_{24h}} \tag{3.5}$$

where $PM(h)$ is the hourly value and PM_{24h} is the 24-hour moving average centered on hour h. The same quantity is calculated for RH. We then compute the monthly average of $Dif_{PM}(h)$ and $Dif_{RH}(h)$ for each hour to visualize how the diurnal pattern changes throughout the year.

Figure 3.10 presents these monthly-averaged diurnal deviations as heatmaps, where columns represent months (February = 2 to September = 9) and rows represent hours (00:00 = 0 to 23:00 = 23). Colors indicate the fractional deviation from the daily mean, with warm colors (red/yellow) indicating values above the daily average and cool colors (blue) indicating values below average.

The diurnal variability differs markedly between RH and $PM_{2.5,wet}$. RH follows a consistent daily cycle throughout the measurement period: maximum values occur during early morning (05:00-09:00) when temperatures are lowest, followed

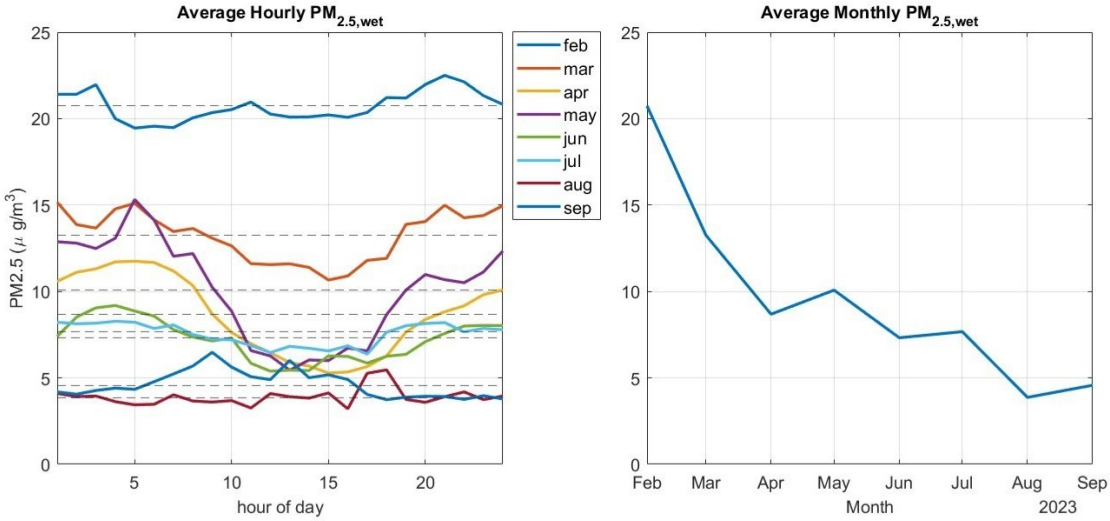

(a) $PM_{2.5,wet}$

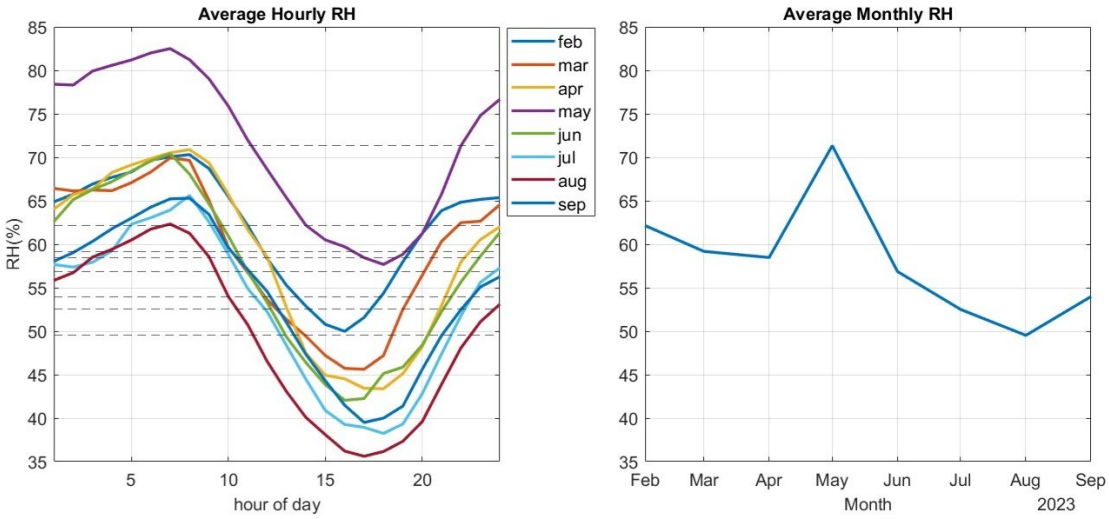

(b) *RH*

Figure 3.9: Diurnal and seasonal variability of $PM_{2.5,wet}$ and RH during the measurement period (February-September 2023). Left panels: average hourly variation for each month (colored lines). Right panels: monthly mean values. Note the consistent diurnal RH cycle throughout the year (b) versus the month-dependent $PM_{2.5,wet}$ diurnal variation (a), which is pronounced only during March-May.

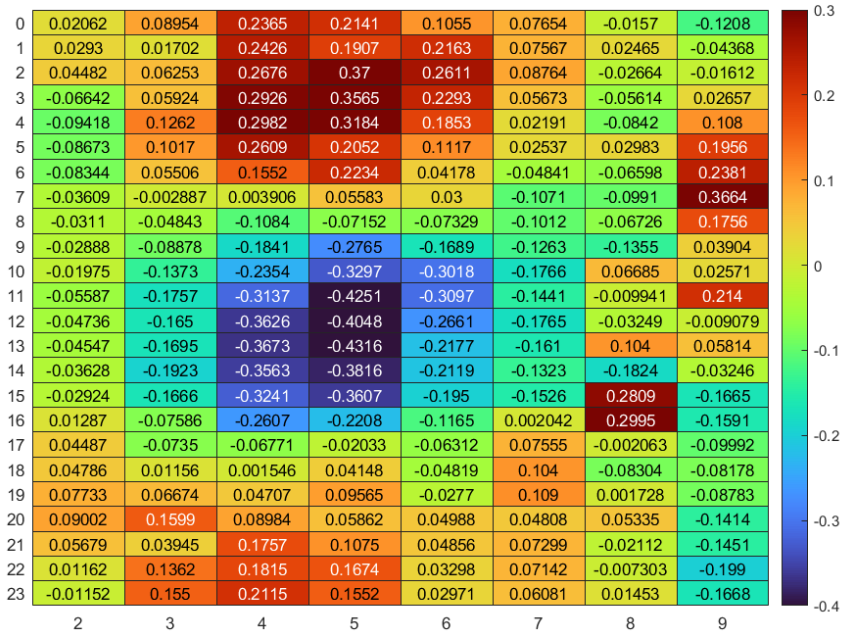

(a) $PM_{2.5,wet}$

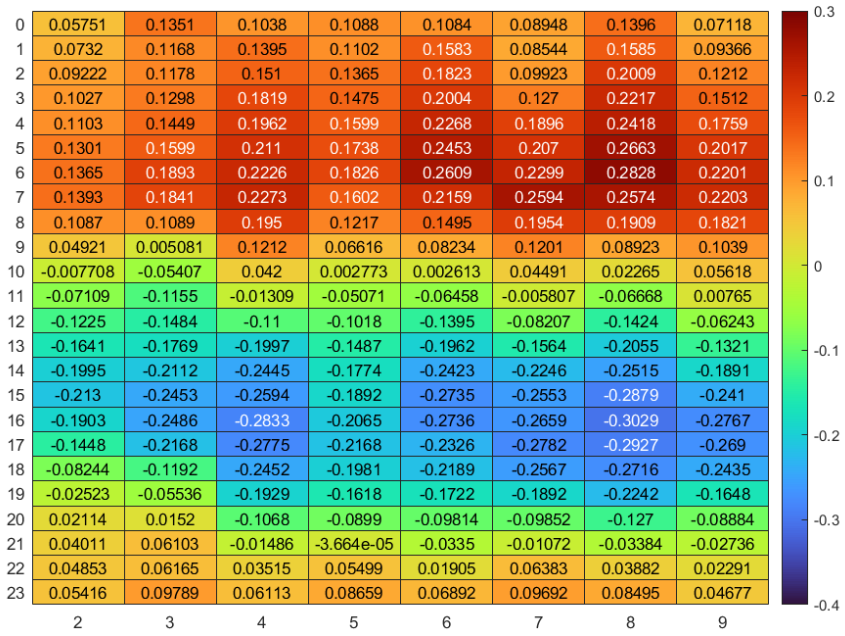

(b) *RH*

Figure 3.10: Relative diurnal variation from the 24-hour moving average for each month, for (a) $PM_{2.5,wet}$ and (b) RH. Columns: months from February (2) to September (9). Rows: hours from midnight (0) to 23:00 (23).

by a steady decrease to minimum values in afternoon (15:00-17:00) when solar heating peaks and temperature is highest. This pattern is stable across all months, with only the average value varying (larger values in February and May than in spring and summer).

In contrast, $PM_{2.5,wet}$ exhibits pronounced diurnal variation only during April and May, and to a lesser extent in March. During these months, $PM_{2.5,wet}$ shows maximum values late at night (02:00-05:00) and minimum values during late morning to early afternoon (10:00-15:00). For the remaining months (February, June-September), the diurnal variation is weak or absent, with hourly values fluctuating within a narrow range around the daily mean.

Temporal Offset Between PM and RH Cycles

The observed temporal offset between the diurnal cycles of $PM_{2.5,wet}$ (if present) and RH indicates the dependence of daily $PM_{2.5,wet}$ variation on other processes.

The late-morning $PM_{2.5,wet}$ minimum coincides with the period of rapid boundary layer growth due to surface heating. During this time, the mixing layer height increases, causing efficient vertical dilution of surface pollutants. This boundary layer dilution effect may dominate over hygroscopic processes during the late morning hours.

Additional factors contributing to $PM_{2.5,wet}$ diurnal variability include: (1) difference in traffic emissions, with the rush hour peaks (07:00-09:00 and 18:00-20:00) introducing fresh primary aerosols; (2) diurnal variations in wind speed and direction that can affect both dilution and regional transport; (3) secondary aerosol formation rates peaking when solar radiation is strongest; (4) evaporation of semi-volatile species (e.g., ammonium nitrate, semi-volatile organic compounds) during warmer afternoon hours.

3.3.2 PM-RH Hysteresis

To investigate the relationship between $PM_{2.5,wet}$ and RH, we examine the scatter of hourly $PM_{2.5,wet}$ versus hourly RH for each month.

Figure 3.11 shows the presence of hysteresis cycles from March to June. The relationship between $PM_{2.5,wet}$ and RH follows different trajectories depending on whether humidity is increasing (nighttime into morning, from yellow to blue) or decreasing (afternoon into evening, from cyan to green). For a given RH value, $PM_{2.5,wet}$ tends to be higher during the humidification phase (increasing RH during evening and night) than during the dehumidification phase (decreasing RH during morning and afternoon).

The width of the hysteresis varies by month. April and May show the most pronounced loops, probably because of the higher precipitation in this period.

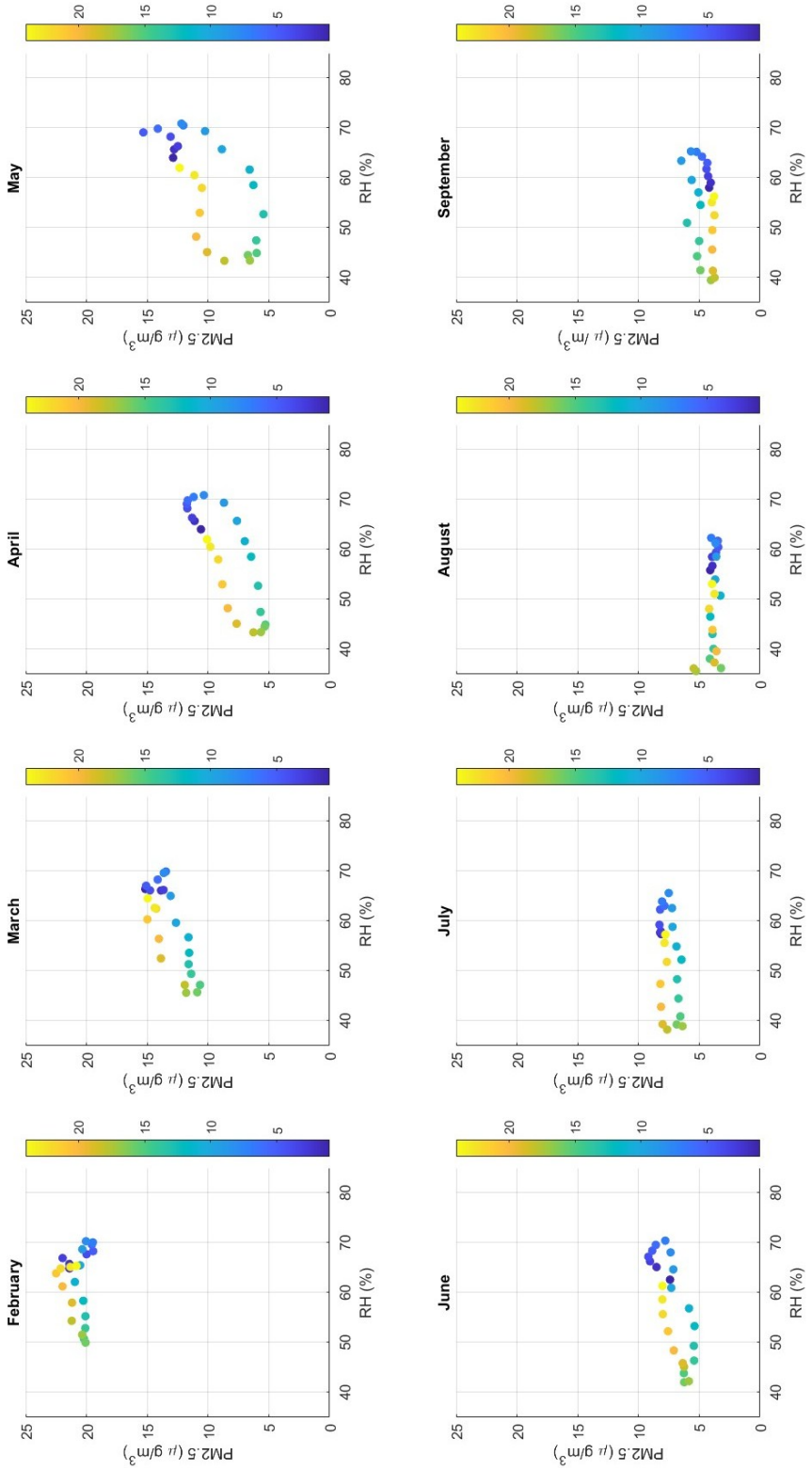

Figure 3.11: Hourly $PM_{2.5,wet}$ versus RH for each month (February-September 2023). Points are color-coded by hour of day to show the diurnal cycle trajectory (blue to cyan: midnight to midday; green to yellow: midday to midnight).

March shows smaller loops possibly because of the contribution of hydrophobic carbonaceous aerosols, which may also explain the absence of a similar hysteresis structure in February.

June shows a weakening of the hysteresis, suggesting a transition toward summer conditions, where the change in chemical composition (as mentioned previously in Section 3.2) and atmospheric processes make $PM_{2.5,wet}$ uncorrelated to RH changes. Desert dust intrusions during June and July introduce mineral particles with low hygroscopicity, while the increased temperature favour the evaporation of semi-volatile aerosols and the increased solar radiation produces variations in secondary aerosol formation independent of RH. Moreover, during summer the aerosols are diluted in deeper mixing layers, and atmospheric instability may dominate over hygroscopic processes.

This hysteresis behaviour has previously been documented in aerosol scattering coefficients and mass concentration (Randriamiarisoa et al., 2006; Ferrero et al., 2019). When RH increases, dry crystalline particles (particularly inorganic salts, such as ammonium sulfate and ammonium nitrate) remain in solid phase until reaching the Deliquescence Relative Humidity (DRH). When RH decreases, the water-soluble compounds remain as supersaturated solution droplets until they reach the Crystallization Relative Humidity (CRH), which is lower than the DRH. When Relative Humidity values are between DRH and CRH, particles may exist in either solid or liquid states depending on their recent humidity history. During humidification starting from low RH, particles remain solid until reaching DRH. During dehumidification from high RH, particles remain aqueous until reaching CRH. This creates the observed hysteresis loop.

The presence of pronounced hysteresis during March-May provides strong evidence that Po Valley aerosols during this period are dominated by semi-volatile inorganic salts (primarily ammonium sulfate and ammonium nitrate). This is consistent with chemical composition studies showing 75% of $PM_{2.5}$ consists of water-soluble inorganic compounds (Ricciardelli et al., 2016) and source apportionment studies indicating large secondary inorganic aerosol contributions during spring (Tositti et al., 2013).

3.3.3 Hygroscopic Growth Function

Having established that hygroscopic effects are significant during winter-spring months, we now attempt to quantify these effects by fitting an empirical hygroscopic growth function to the data. The objective is to determine whether a simple parametrization can describe the observed $PM_{2.5,wet}$-RH relationship and to compare the derived parameters with literature values for similar aerosol types.

The variation of $PM_{2.5}$ with RH can be expressed as:

$$PM_{2.5,wet}(RH) = f(RH) \cdot PM_{2.5,dry} \tag{3.6}$$

where $f(RH)$ is the hygroscopic growth function and $PM_{2.5,dry}$ represents the mass concentration under dry conditions (RH $< 50\%$). The function $f(RH)$ depends primarily on aerosol chemical composition.

We use the Hänel parametrization (Hänel, 1981), which has been widely applied to describe hygroscopic growth of aerosol optical properties (see also Section 2.1.4). Recalling Eq. 2.24

$$f(RH) = \left(1 - \frac{RH}{100}\right)^{-\gamma}, \tag{3.7}$$

where γ is the Hänel exponent, an empirical coefficient that depends on aerosol type, we fit our data to the function:

$$Y = a(1 - X)^b \tag{3.8}$$

where $X = RH/100$, a is a normalization constant (theoretically $a \approx 1$) and $b = -\gamma$ is the fitted exponent.

Since co-located dry $PM_{2.5}$ measurements are not available at DIFA, we cannot directly determine $f(RH)$ or $PM_{2.5,dry}$. Instead, we normalize $PM_{2.5,wet}$ values for each month by the minimum value observed during that month, $PM_{2.5,wet,min}$. Similar to the definition in Eq. 2.24:

$$Y = \frac{PM_{2.5,wet}}{PM_{2.5,wet,min}} \approx \frac{f(RH)}{f(RH_{min})} \tag{3.9}$$

We perform least-squares fits using daily-averaged $PM_{2.5,wet}$ and RH for each month separately. The goodness of fit is assessed using the coefficient of determination (R^2) and Root Mean Square Error (RMSE). To facilitate comparison with previous studies, we also calculate the standard metric:

$$f(80\%) = a\left(1 - \frac{80}{100}\right)^b \tag{3.10}$$

which represents the ratio of wet to dry $PM_{2.5}$ at RH $= 80\%$.

Results

Figure 3.12 shows the fitted functions (red lines) overlaid on the daily-averaged data (blue points) for each month. Table 3.5 summarizes the fitted parameters, uncertainties, goodness-of-fit metrics, and derived $f(80\%)$ values.

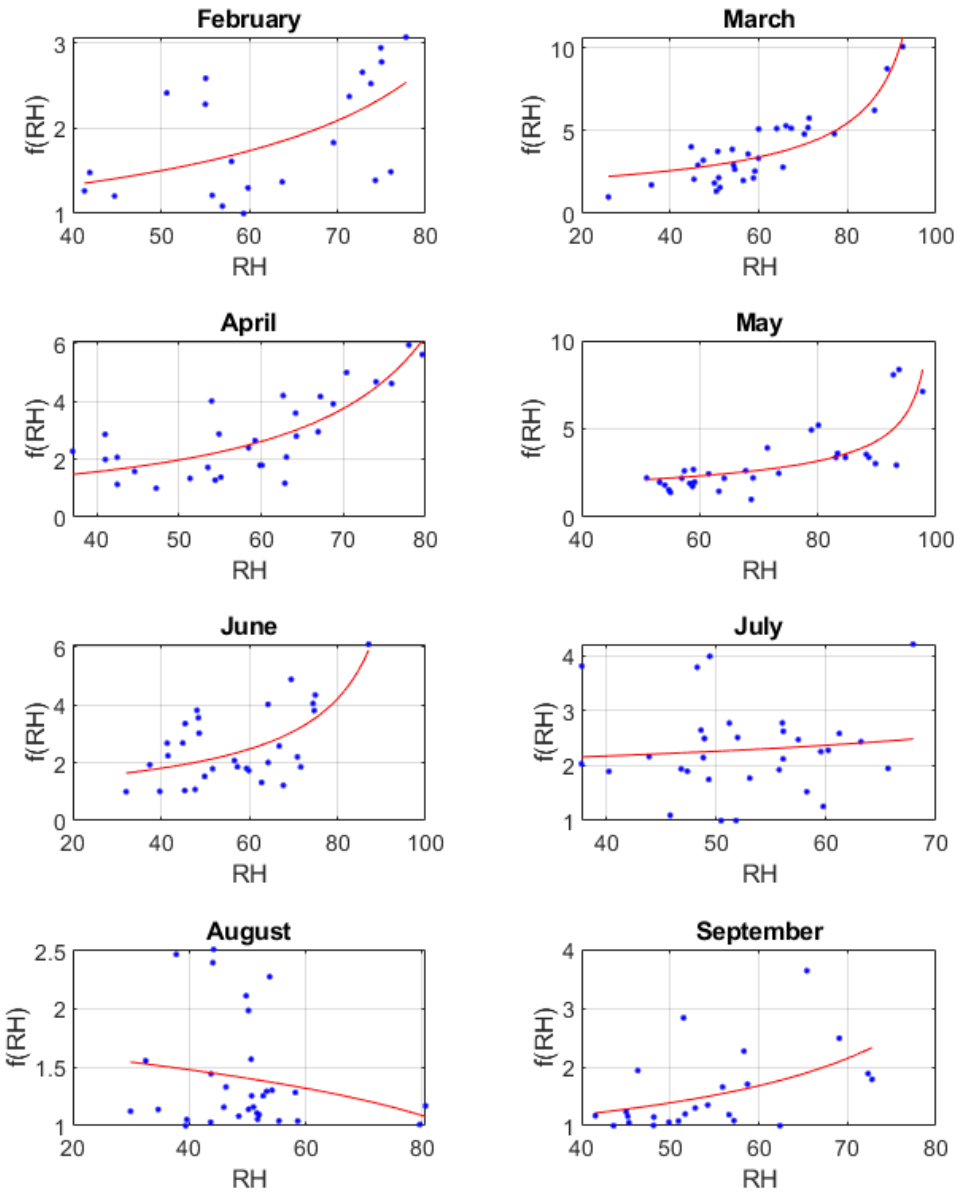

Figure 3.12: Results of Hänel function fits (Eq. 3.8) for each month. Blue points: daily-averaged normalized $PM_{2.5,wet}$ versus RH. Red lines: fitted functions. Only March-May show reasonable fits ($R^2 > 0.5$); other months show poor fits due to weak or absent $PM_{2.5,wet}$-RH correlation.

Month	a	b	R^2	RMSE	$f(80\%)$
Feb	$0.960 \pm 56\%$	$-0.647 \pm 73\%$	0.303	0.591	$2.72 \pm 52\%$
Mar	$1.828 \pm 20\%$	$-0.681 \pm 18\%$	**0.766**	3.578	$5.47 \pm 40\%$
Apr	$0.826 \pm 40\%$	$-1.259 \pm 26\%$	**0.667**	2.577	$6.27 \pm 33\%$
May	$1.552 \pm 31\%$	$-0.445 \pm 28\%$	**0.585**	4.058	$3.18 \pm 79\%$
Jun	$1.221 \pm 37\%$	$-0.769 \pm 38\%$	0.410	2.801	$4.21 \pm 23\%$
Jul	$1.955 \pm 64\%$	$-0.212 \pm 383\%$	0.008	2.683	$2.75 \pm 93\%$
Aug	$1.707 \pm 38\%$	$+0.280 \pm 190\%$	0.045	1.275	$1.09 \pm 102\%$
Sep	$0.771 \pm 61\%$	$-0.850 \pm 77\%$	0.233	1.630	$3.03 \pm 65\%$

Table 3.5: Monthly Hänel function fit results for hygroscopic growth analysis. Fitted function: $Y = a(1-X)^b$ where $X = RH/100$ and $Y = PM_{2.5,wet}/PM_{2.5,wet,min}$. The Hänel hygroscopicity parameter is $\gamma = -b$. Bold rows indicate acceptable fits ($R^2 > 0.5$). Uncertainties represent 95% confidence bounds from least-squares regression.

The fitting results show strong month-to-month variability in both goodness-of-fit and derived parameters. March, April, and May yield reasonable fits, with R^2 values of 0.77, 0.67, and 0.59, respectively. These are the same months showing pronounced diurnal $PM_{2.5,wet}$ variation and clear hysteresis loops (Figures 3.10 and 3.11). The fitted exponents correspond to Hänel coefficients $\gamma = 0.68$, 1.26, and 0.45, all positive as expected for hygroscopic growth.

February and June show weak correlations ($R^2 = 0.30$ and 0.41), while July-September show essentially no correlation ($R^2 < 0.25$). August exhibits a positive exponent b (negative γ), which is physically unrealistic and indicates that the Hänel function cannot describe the data. The poor fits during summer months are consistent with the weak $PM_{2.5,wet}$-RH correlation shown in Figure 3.11.

Even for the best-fit months (March-April), relative uncertainties on the fitted coefficients range from 18-40%, and uncertainties on the derived $f(80\%)$ values are 33-40%. For months with poor fits, uncertainties exceed 100%, rendering the fitted values meaningless.

Interpretation and Comparison with Literature

The derived $f(80\%)$ values during months with acceptable fits (March-May) (5.47, 6.27, and 3.18, respectively) are higher than typically reported for urban aerosols but fall within the range expected for aerosols dominated by hygroscopic inorganic salts. To interpret the values of $f(80\%)$ obtained by our fits, we compare them with literature ranges compiled by Cheng et al. (2008) and Liu et al. (2013):

- $f(80\%) = 1.0\text{-}1.13$ for dust aerosols (nearly non-hygroscopic),
- $f(80\%) = 1.1\text{-}1.2$ for fresh biomass burning aerosols,
- $f(80\%) = 1.4\text{-}1.6$ for anthropogenic aerosols (mixed urban pollution),
- $f(80\%) = 1.58\text{-}1.81$ for polluted marine aerosols,
- $f(80\%) = 1.8\text{-}2.3$ for clean marine aerosols (sea salt dominant).

These values were retrieved in empirical studies, conducted in a short time and selected locations. There is no definitive classification to assign specific values to each aerosol mixture. Day and Malm (2001) found $f(80\%) \approx 2$ for aerosol mixtures dominated by inorganic salts, and $f(80\%) \approx 1.2$ for mixtures with higher fractions of organic carbon compounds and soil. Randriamiarisoa et al. (2006) investigated an urban area in France and found $f(80\%) > 2$ ($\gamma > 1$) for periods with anthropogenic aerosols high in inorganic salt content, and $f(80\%) \approx 1 - 1.4$ ($\gamma < 0.5$) associated with high content of biomass burning aerosols.

Marine aerosol values, dominated by inorganic salts, can serve as proxies for continental aerosols rich in inorganic salts such as ammonium sulfate and ammonium nitrate. For example, Ferrero et al. (2019) retrieved empirical values of $f(RH)$ in Milan (Po Valley), and found $f(80\%) \approx 1.8$ for winter and $f(80\%) \approx 1.2$ for summer, interpreted as different mixtures of inorganic salts and pollution.

Our derived March-April values ($f(80\%) = 5.5\text{-}6.3$) exceed these literature ranges, suggesting systematic overestimation. Several factors may contribute to this overestimation.

Firstly, we normalized $PM_{2.5,wet}$ by the monthly minimum value, assuming this minimum can represent "dry" conditions. The data analysis reveals RH rarely drops below 40-50% in Bologna, even during minimum RH periods. We can accept this approximation, as the "dry" $PM_{2.5}$ is measured at RH = 50%, and the Hänel parametrization is often defined as the ratio between the extinction coefficient at ambient RH and at a reference RH = 40-50% (see also Eq. 2.24). However, the monthly minim value of $PM_{2.5,wet}$ may not occur during the lowest RH value for the month, inflating the empirical $f(80\%)$ value.

Secondly, the hygroscopic growth function attributes all $PM_{2.5,wet}$ variability to RH changes, but other factors (emissions, boundary layer dynamics, chemistry) contribute significantly, as discussed in the previous analysis. Lastly, the Hänel parametrization does not account for hysteresis cycles; we partly account for this by using daily values of RH and PM, thus deriving an average function that does not capture the daily variability.

Despite these limitations, the fitted values provide useful qualitative insights. The successful fits during March-May and failed fits during July-September confirm that hygroscopic effects dominate only during certain seasons, consistent with

compositional changes. Even accounting for potential overestimation, the large $f(80\%)$ values during March-April indicate strong hygroscopic growth, consistent with inorganic-salt-dominated aerosols. The fitted Hänel exponents (γ = 0.45-1.26) fall within the range reported by Randriamiarisoa et al. (2006) for similar aerosol types. While the absolute values are unreliable, the results suggest that applying literature-based hygroscopic corrections for inorganic-dominated mixtures ($f(80\%) \approx 2.0$) is reasonable for the Po Valley during winter-spring, as also found by Ferrero et al. (2019).

Given these limitations, rather than attempting to derive site-specific hygroscopic corrections with large uncertainties, the physics-informed methodology (Chapter 4) takes a different approach: directly relating satellite AOD (at ambient RH) to LOAC $PM_{2.5,wet}$ (at ambient RH), thereby avoiding hygroscopic corrections entirely. This "wet-to-wet" comparison is more robust and eliminates the need for uncertain empirical correction functions.

3.4 Conclusions

This chapter presented a comprehensive analysis of the datasets used in the physics-informed AOD-$PM_{2.5}$ methodology, with particular emphasis on characterizing LOAC measurements and their relationship to meteorological conditions and hygroscopic effects.

3.4.1 Key Findings

The LOAC measurements revealed distinct responses to episodic meteorological events. Precipitation events caused dramatic increases in both $PM_{2.5,wet}$ (>50 $\mu g/m^3$) and effective radius (>2 μm) due to hygroscopic growth, while desert dust intrusions during June-July produced elevated effective radius increases (up to 8 μm). Under typical conditions, the effective radius remained below 0.6 μm, reflecting accumulation-mode-dominated urban aerosol. Particle type analysis showed that "salt" and "mineral" types dominate fine particles (70-90%) throughout the year, with seasonal variations reflecting changes in dust transport and secondary aerosol formation.

The ceilometer-derived MLH required careful selection among multiple detected levels, guided by comparison with climatological radiosonde data. The dynamic selection algorithm identified appropriate MLH values for the majority of satellite overpasses, with L2 selected during early morning (residual layer) and L1 during midday (convective boundary layer).

The $PM_{2.5}$-RH analysis demonstrated strong seasonal dependence of hygroscopic effects. Clear hysteresis cycles during March-May provide evidence of

inorganic-salt-dominated aerosols, consistent with chemical composition studies. Quantitative hygroscopic corrections could not be reliably derived due to methodological limitations (lack of co-located dry $PM_{2.5}$, normalization artifacts, influence of non-RH factors), but qualitative insights support literature-based values ($f(80\%) \approx 2$) for winter-spring conditions.

3.4.2 Implications for the Methodology

The preliminary studies presented in this chapter inform several key methodological decisions in Chapter 4.

Firstly, we exclude data from days with precipitation and dust transport events. To filter the data systematically, we apply uncertainty threshold on r_{eff} and $PM_{2.5,wet}$ to select stable aerosol conditions.

Secondly, the inability to derive robust hygroscopic corrections, combined with evidence that hygroscopic effects are significant but complex, justifies directly relating satellite AOD (at ambient RH) to LOAC $PM_{2.5,wet}$ (at ambient RH) without intermediate corrections. This approach is more robust than applying empirical hygroscopic functions with large uncertainties.

Lastly, the LOAC auxiliary data (PN and particle type classification) enable the calculation of aerosol physical, chemical and optical properties (r_{eff}, $\langle Q_{ext,aer} \rangle$ and ρ_{aer}) that account for compositional variability. This physics-informed approach is expected to improve the AOD-$PM_{2.5}$ correlation compared to methods assuming constant aerosol properties.

Chapter 4

Physics-informed AOD-PM Framework

This chapter applies the AOD-PM theoretical relationship presented in Chapter 2 to develop and validate a physics-informed methodology for estimating ground-level $PM_{2.5}$ from satellite AOD. The approach exploits LOAC measurements analysed in Chapter 3 together with co-located satellite AOD from MODIS, Mixing Layer Height from a ceilometer, and LOAC-derived aerosol properties. We investigate whether incorporating physically based aerosol parameters improves correlation compared to simple empirical approaches, and we assess the importance of correcting systematic biases in LOAC-derived effective radius calculations.

4.1 Objectives

This chapter has three primary objectives: (1) address the LOAC lower detection limit which excludes ultra-fine particles; (2) compute the theoretical AOD-PM coefficient using LOAC-derived aerosol properties; (3) study the linear correlation between AOD and PM.

The LOAC lower size detection limit (0.2 μm diameter) excludes ultra-fine particles that contribute significantly to particle number concentration and optical properties (Figure 1.1). Before applying our methodology, we quantify this bias through numerical simulations and develop a correction algorithm for the Effective Radius, which is the most affected optical parameter.

Then, we estimate the three aerosol properties required to calculate the theoretical coefficient $A = \frac{4\rho_{aer}r_{eff}}{3\langle Q_{ext,aer}\rangle}$: Effective Radius from PN measurements, average Extinction Efficiency from particle type classification and Mie theory, and average mass density from particle type fraction.

Finally, we are able to compare linear correlations between $PM_{2.5}$ and satellite

AOD in three cases: (a) without auxiliary data, (b) with LOAC-derived coefficient A, and (c) with corrected Effective Radius. This quantifies the improvement gained by incorporating physical aerosol properties.

To our knowledge, this represents the first study to directly use optical particle counter measurements to derive the theoretical coefficient between satellite AOD and ground-level PM, providing a physically interpretable alternative to purely empirical or statistical approaches.

4.2 Effective Radius Correction

The LOAC detects particles with diameters between 0.2 and 30 μm, corresponding to radii from 0.1 to 15 μm. This range is adequate for PM calculations, which depend on the volume size distribution (Eq. 2.10), but it introduces a systematic bias in Effective Radius calculations.

The Effective Radius is defined as the ratio of the third to the second moments of the PSD (Eq. 2.8), making it sensitive to the complete particle number distribution. Ultra-fine particles with radii below 0.1 μm, though negligible for mass calculations, can represent a large fraction of total PN in urban environments. When these particles are not detected, the calculated r_{eff} shifts toward larger values.

Since r_{eff} appears directly in the theoretical coefficient A (Eq. 4.5), any systematic bias will propagate to PM estimates. Before applying Eq. 4.5, we must quantify and correct this bias.

4.2.1 Numerical simulations

In order to quantitatively study the difference between the theoretical values of r_{eff} and the respective values calculated from LOAC PN data, we perform some numerical simulations of PSD for different urban aerosol mixtures. The code used to simulate the urban aerosol PSDs is described in Appendix A.2.

The Effective Radius is independent of the total number of particles, so we consider PSDs normalized to 1 particle per cm^3. The PSD can be estimated from the PN measurements as explained in Section 3.1.1 (Eq. 3.2). Figure 4.1a shows an example of experimental Number, Area and Volume Distributions, calculated by discretization of Eqs. 2.9-2.10. For smaller particles (radii between 0.1 and 1 μm), the Number Distribution is about two orders of magnitude higher than the Volume Distribution; for larger particles (radii between 1 and 15 μm), the Number Distribution is about five orders of magnitude lower than the Volume Distribution.

We calculate the theoretical PSDs of several urban aerosol mixtures based on the OPAC parametrization (Eq. A.6, Hess et al. (1998)). We consider particle

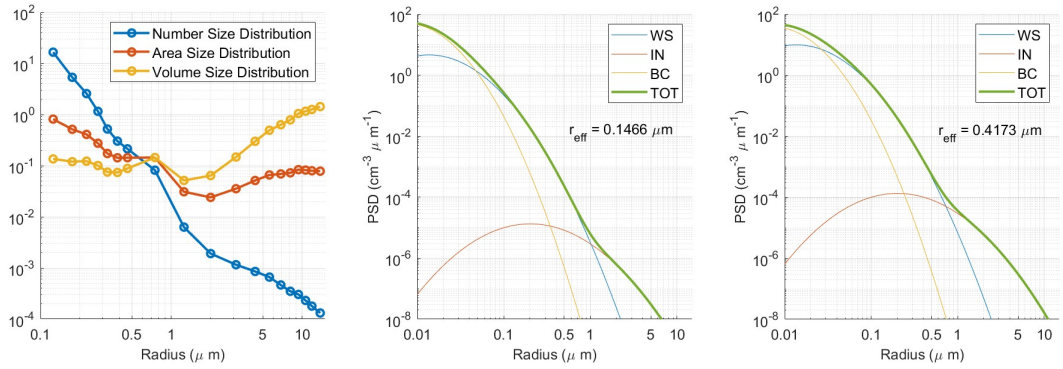

(a) (b) (c)

Figure 4.1: (a) Comparison between normalized Number ($\mathrm{cm}^{-3}\mu\mathrm{m}^{-1}$), Area ($\mathrm{cm}^{-3}\mu\mathrm{m}^{2}\mu\mathrm{m}^{-1}$), and Volume ($\mathrm{cm}^{-3}\mu\mathrm{m}^{3}\mu\mathrm{m}^{-1}$) size distributions from LOAC data. (b-c) Example of PSD numerical simulations. The PSD is composed of Soluble (WS), Insoluble (IN) and Soot (BC). Different Number Ratios (NR). The theoretical Effective Radius is also shown. (b) more smaller particles: $\mathrm{NR}_{WS} = 18\%$, $\mathrm{NR}_{IN} = 10^{-3}\%$, $\mathrm{NR}_{BC} = 82\%$. (c) more larger particles: $\mathrm{NR}_{WS} = 38\%$, $\mathrm{NR}_{IN} = 10^{-2}\%$, $\mathrm{NR}_{BC} = 62\%$.

radii from 0.05 to 20 μm. In Figure 4.1 b and c we show two examples, with different Number Ratios, with their respective values of r_{eff}.

Using the OPAC parametrization of the PSD, we calculate the PN with Eq. 3.1 and the Effective Radius with Eq. 3.3. This should approximate what the LOAC would measure in an idealized scenario (without considering instrumental errors and the LOAC response function). Figure 4.2 compares the OPAC PSDs and r_{eff} values with the simulated LOAC PSDs and $r_{eff,LOAC}$ for the same examples of Figure 4.1b and c. It is apparent that $r_{eff,LOAC}$ overestimates the theoretical value of the Effective Radius.

The magnitude of overestimation depends on two factors: (1) the LOAC's lower detection limit at 0.1 μm radius, and (2) the shape of the size distribution. The degree of overestimation is greater when the ratio of particle concentrations below versus above 0.1 μm is higher.

4.2.2 Correction Algorithm

To correct for the missing ultra-fine particles, we extrapolate the size distribution below the LOAC detection limit. We hypothesize an additional size bin (bin "0") covering diameters 0.1-0.2 μm and estimate the particle number concentration PN_0 in this bin using the measured concentrations in the first four LOAC bins.

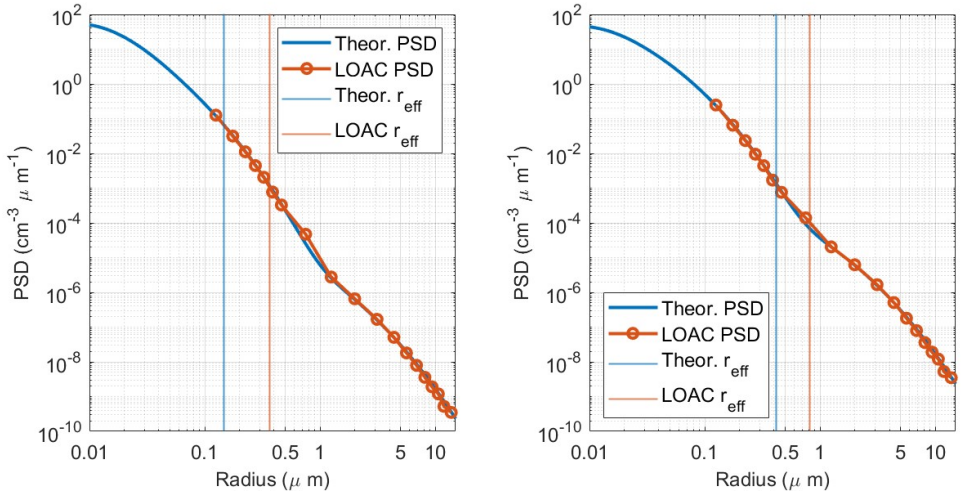

Figure 4.2: Comparison between the theoretical PSDs in Figure 4.1 and the idealized LOAC PSD. Vertical lines represent the Effective Radius calculated respectively with Eq. 2.8 and Eq. 3.3.

The extrapolation uses a second-order polynomial fit in log-log space between bin centre radius r_i and particle size distribution $n_i = PN_i/\Delta r_i$. This approach relies only on the measured data, as the theoretical PSD is used only for validation, not for the extrapolation itself. This ensures the method can be applied to real LOAC measurements.

Table 4.1 shows the results of the extrapolation for the two examples represented in Figure 4.2. In both cases the Effective Radius is overestimated by the LOAC: in the first case (higher fraction of smaller particles), $r_{eff,LOAC}$ is about 1.5 the theoretical value, and in the second case (higher fraction of larger particles),

Case	r_{eff}	$r_{eff,LOAC}$	$r'_{eff,LOAC}$	$\frac{r'_{eff,LOAC}}{r_{eff,LOAC}}$	$\Delta r_{eff,LOAC}$	$\Delta r'_{eff,LOAC}$
1	0.1466	0.3645	0.1729	0.47	+148%	+18%
2	0.4173	0.8134	0.3740	0.46	+194%	-10%

Table 4.1: Extrapolation results for the two examples in Figure 4.2. r_{eff} is the theoretical value from OPAC PSD; $r_{eff,LOAC}$ is the value computed from the simulated LOAC PN with Eq. 3.3; $r'_{eff,LOAC}$ is the corrected value computed with the addition of the extrapolated PN_0. The relative errors between the theoretical and the approximated values are also reported.

it is almost double the theoretical value. Meanwhile, the value of $r'_{eff,LOAC}$, that is the Effective Radius calculated with the extrapolation of PN_0, is within 20% of the theoretical value, respectively higher and lower in the two cases.

4.3 Computation of aerosol properties

4.3.1 Effective Radius from LOAC Measurements

The Effective Radius is computed from LOAC 1-minute PN measurements using the discretized form in Eq. 3.3 and calculating the hourly averages with standard deviation as uncertainty. The r_{eff} data analysis has already been presented in Section 3.2.2. Here, we apply the extrapolation methodology developed in Section 4.2 to compute the corrected Effective Radius $r'_{eff,LOAC}$ for all hourly measurements. The ratio $r'_{eff,LOAC}/r_{eff,LOAC}$ provides insight into the magnitude of the LOAC size-limit bias in real urban conditions:

- 43% of cases: ratio between 0.5-0.7
- 43% of cases: ratio between 0.7-0.9
- 8% of cases: ratio ≈ 1 (correction negligible)
- <1% of cases: ratio > 1 (outliers, likely missing PN data)

These results are consistent with the simulations (Table 4.1, column 4), where ratios of 0.46-0.47 were obtained. This suggests that the correction methodology successfully reduces the systematic overestimation to levels comparable to the simulation validation.

For typical urban aerosol conditions in Bologna, $r'_{eff,LOAC}$ is approximately 60-70% of the uncorrected value. Uncertainties remain comparable (20-30% for normal conditions, >50% during precipitation/dust events) because they reflect temporal variability within each hour rather than the systematic bias we have corrected.

4.3.2 Average Mass Density

The average mass density of the aerosol mixture is calculated as a weighted average using Number Ratios computed from particle type classification and nominal mass densities from the LOAC algorithm:

$$\rho_{aer} \cong \frac{\sum_i PN_i(m_1 NR_{1,i} + m_2 NR_{2,i} + m_3 NR_{3,i})}{\sum_i PN_i} \quad i = 1, ..., 19 \qquad (4.1)$$

where m_x is the nominal mass density for particle type x (constant across all size bins) and $NR_{x,i}$ is the Number Ratio of particle type x in size bin i (Eq. 3.4).

The LOAC algorithm uses identical mass density values for "salt" and "mineral" types, both higher than the value for "carbon" type (Table 3.4). Consequently, ρ_{aer} is negatively correlated with the carbon particle fraction, particularly $\mathrm{NR}_{1,carbon}$ in the first size class where particle number concentrations are highest (Figure 3.5).

Unlike r_{eff}, the mass density is not strongly affected by precipitation events or desert dust episodes because we exclude the droplet classification. Temporal variability in ρ_{aer} reflects changes in the salt/mineral versus carbon mixture, which varies with emission sources (traffic vs. residential heating vs. biomass burning).

4.3.3 Average Extinction Efficiency

The LOAC particle type classification is based on absorption properties inferred from scattering measurements. Renard et al. (2010) demonstrated that the LOAC prototype could distinguish particles with different imaginary parts of the refractive index (k) at 650 nm. Renard et al. (2016) established the classification algorithm using laboratory measurements of atmospheric aerosol samples with known composition.

We associate each LOAC type with a corresponding aerosol component from the OPAC (Optical Properties of Aerosols and Clouds) database (Hess et al., 1998). OPAC is widely used for aerosol radiative transfer calculations and provides size-resolved optical properties based on Mie theory for various aerosol types. For urban environments, OPAC defines mixtures of water-soluble, insoluble, and soot components (see also Appendix A.1).

The matching is based on absorption characteristics at the LOAC laser wavelength (650 nm):

- "salt" LOAC type → "Water Soluble" OPAC type (RH = 50%)
- "mineral" LOAC type → "Insoluble" OPAC type
- "carbon" LOAC type → "Soot" OPAC type

These three components adequately represent the urban aerosol mixture in the Po Valley, which is dominated by anthropogenic emissions with negligible contributions from sea salt or biogenic particles (Ricciardelli et al., 2016; Tositti et al., 2013).

For each OPAC aerosol type, we compute the single-particle extinction efficiency $Q_{ext,x}(r)$ as a function of radius using Mie theory at the AOD wavelength

(550 nm). Details of the Mie calculations are provided in Appendix A.1. We integrate $Q_{ext,x}(r)$ over each LOAC size bin to obtain bin-averaged values:

$$Q_{x,i} = \frac{\int_{r_i}^{r_{i+1}} Q_{ext,x}(r)dr}{\Delta r_i}. \tag{4.2}$$

The mixture-averaged extinction efficiency is then calculated by discretizing Eq. 2.14 using LOAC particle number concentrations and type fractions:

$$\langle Q_{ext,aer} \rangle \cong \frac{\sum_i PN_i R_i^2 (Q_{1,i} NR_{1,i} + Q_{2,i} NR_{2,i} + Q_{3,i} NR_{3,i})}{\sum_i PN_i R_i^2}. \tag{4.3}$$

Like ρ_{aer}, the extinction efficiency depends primarily on the particle type fractions in the first size class, where both PN and scattering cross-sections are largest. Specifically, $\langle Q_{ext,aer} \rangle$ correlates positively with $\mathrm{NR}_{1,salt}$ and negatively with $\mathrm{NR}_{1,mineral}$ due to their different optical properties.

4.3.4 Uncertainties

The Effective Radius uncertainty is the standard deviation of the hourly-averaged 1-minute calculations, typically 20-30% under normal conditions.

For ρ_{aer} and $\langle Q_{ext,aer} \rangle$, the single-particle values (m_x and $Q_{x,i}$) are taken from literature/models and have no assigned uncertainty. The Number Ratio is derived from categorical 1-minute classifications with no quantitative uncertainty estimate. Therefore, uncertainties in ρ_{aer} and $\langle Q_{ext,aer} \rangle$ propagate primarily from the PN measurement uncertainties.

The composed uncertainty on the theoretical coefficient A is dominated by the r_{eff} uncertainty due to its relatively large variability (20-30%) compared to the temporal stability of ρ_{aer} and $\langle Q_{ext,aer} \rangle$.

4.4 Linear regressions

4.4.1 Theoretical framework

The approximate linear relationship between $\mathrm{PM}_{2.5}$ and AOD at ambient conditions, derived in Chapter 2.1.4, can be written as:

$$PM_{2.5,wet} \approx A \frac{AOD}{MLH} \tag{4.4}$$

where the theoretical coefficient A is:

$$A = \frac{4 \rho_{aer} r_{eff}}{3 \langle Q_{ext,aer} \rangle} \tag{4.5}$$

This approximation holds when aerosols are well-mixed below the mixing layer height (MLH) and the AOD is dominated by fine-mode particles, conditions typically satisfied in urban areas like Bologna (see also Section 1.2).

All three quantities in A are estimated from LOAC measurements: effective radius r_{eff} from particle size distributions, average mass density ρ_{aer} from particle type classification, and average extinction efficiency $\langle Q_{ext,aer} \rangle$ from particle type and Mie scattering calculations.

4.4.2 Statistical Methods

In the present study, we investigate the linear correlation between LOAC $PM_{2.5,wet}$ and the PM estimated using satellite AOD, corrected with the MLH, and the LOAC-derived estimated of A (Eq. 4.5).

We first calculate the **Pearson's linear correlation coefficient** R. R assumes values between -1 and 1, where 1 means a perfect positive linear correlation between two variables, 0 means no correlation, and -1 a perfect negative linear correlation. Considering positive values, R greater than 0.5 means a strong linear correlation, R between 0.3 and 0.5 means a moderate linear correlation, while R between 0 and 0.3 a weak linear correlation. R is calculated with the MATLAB function *corr* with a 95% confidence level.

We calculate R between $PM_{2.5,wet}$ and AOD in different cases:

- without auxiliary data: $\frac{AOD}{MLH}$
- with the estimated A (all auxiliary data): $A\frac{AOD}{MLH}$
- adding one auxiliary variable at a time: (1) adding the effective radius: $\frac{AOD}{MLH} r_{eff,LOAC}$ and (2) adding the average extinction efficiency: $\frac{AOD}{MLH} \frac{r_{eff,LOAC}}{\langle Q_{ext,aer} \rangle}$. When adding the average mass density, we obtain again the second case.

Secondly, we perform a linear regression with the function

$$Y = aX + b \tag{4.6}$$

with $Y = PM_{2.5,wet}$ and $X = A\frac{AOD}{MLH}$. The linear slope a is close to 1 if the estimated PM calculated with Eq. 4.4 is an accurate estimate of the measured PM. It also means that the calculated A is a good estimate of the linear coefficient between the PM and the scaled AOD. The offset b accounts for other effects, such as the different spatial representativeness between point measurements (from the LOAC and the ceilometer) and the 1 km x 1 km spatial resolution of the AOD.

We perform the linear fit with the MATLAB function *fitlm*, which calculates the linear coefficient with 95% confidence bounds and a set of coefficients to measure the goodness of fit. We consider the **Coefficient of Determination** R^2,

which represents how much the independent variable X explains the variance of Y. We also consider the **Root Mean Square Error** (RMSE), which represents the variance of the residuals and is a good measure to compare different linear models. Lastly, we consider the **Standard Error** (SE) of the linear coefficients a and b, which is a measure of their uncertainty.

For comparison, we perform the linear regression in the "without auxiliary data" scenario and using reference dry $PM_{2.5}$ from the ARPAE station Porta San Felice.

4.4.3 Dataset

The relative uncertainty of AOD retrieved by the MAIAC algorithm is 0.05 (Lyapustin et al., 2018), so the uncertainty assigned to AOD is $\Delta AOD = 0.05 \cdot AOD$. The MLH uncertainty is the maximum between the ceilometer measurement uncertainty of 10 m and the standard deviation of the 10-minute average. The uncertainty assigned to $X = \frac{AOD}{MLH}$ is composed with the relative uncertainty rule:

$$\frac{\Delta X}{X} = \sqrt{0.05^2 + \left(\frac{\Delta MLH}{MLH}\right)^2}. \tag{4.7}$$

The uncertainty assigned to $A\frac{AOD}{MLH}$ is computed in a similar way.

As the $PM_{2.5}$ and Effective Radius are hourly averaged from the 1-minute LOAC data, we assign the standard deviation as uncertainty for both variables.

A single dataset is obtained from different sources. We consider the AOD retrieval time as dataset index. The dataset is composed of AOD, MLH, $PM_{2.5,wet}$, r_{eff}, $\langle Q_{ext,aer} \rangle$, ρ_{aer}, A, and RH. All variables except AOD are time-averaged and associated with the closest AOD observation. To ensure consistency and avoid biases introduced by data gaps, only complete rows of the dataset are considered in the linear regressions and calculation of statistical coefficients. This approach reduces the sample size, but preserves the physical consistency of co-located measurements, which is essential for our physics-informed approach. Imputation methods were not employed, as they would introduce artificial correlations between variables and undermine the direct physical relationship between AOD and ground-based PM that we seek to characterize.

Noise and outliers are addressed using a Hampel filter applied to the LOAC data, as previously mentioned.

For LOAC measurements during periods with available AOD, relative uncertainties average 36% for $PM_{2.5,wet}$ and 22% for r_{eff}, with typical values below 40% and 30% respectively. During precipitation and dust events, uncertainties exceed 50% due to high temporal variability.

To ensure data reliability, we apply the following quality filters:

- $PM_{2.5,wet}$: standard deviation < 3 $\mu g/m^3$ and relative uncertainty $< 20\%$;
- AOD: $0.01 <$ AOD < 0.35 (avoid low-AOD retrieval errors and cloud contamination);
- $\frac{AOD}{MLH}$: relative uncertainty $< 20\%$;
- For the "auxiliary data" cases: absolute uncertainty on $X < 2$ $\mu g/m^3$.

These filters exclude most data from May and September and portions of June-July. Final sample sizes: 56 observations without auxiliary data, 49 observations with auxiliary data.

4.4.4 Results

Without auxiliary data

First, we perform the linear regression with $Y = PM_{2.5,wet}$ and $X = \frac{AOD}{MLH}$, without adding auxiliary information.

The Pearson's correlation coefficient R is 0.56 (out of 1), indicating the presence of a linear correlation between the two variables. The linear regression function has $RMSE = 4.28$ $\mu g/m^3$ and $R^2 = 0.31$. The linear function is $Y_1 = 7.26 + 0.28 \cdot X$. The residuals are normally distributed around 0, with a median of -0.06. The linear function is shown in Figure 4.3a with the selected data points. As expected, the relationship between the variables does not show any clear dependence on RH, suggesting that there is no need for a hygroscopic correction factor.

For comparison, we perform linear regression using daily "dry" $PM_{2.5}$ from the reference ARPAE station Porta San Felice in the same temporal window. As $PM_{2.5}$ data is obtained from reference instruments, we assume that the uncertainty is always below 20%. We assume that the MLH does not change significantly between the station and DIFA, therefore using MLH obtained from the ceilometer. The selected AOD refers to the cell whose centre is closest to the ground-based station.

To obtain daily averages of $X = \frac{AOD}{MLH}$, we first compute the fraction and then average daily the available data. In this case, the regression is performed on 102 data points between February and September 2023.

The value of R is 0.1558, indicating the absence of linear correlation. As it is apparent from Figure 4.3b, "dry" $PM_{2.5}$ and the corrected AOD seem uncorrelated, and there is no correlation with the respective RH value (daily averaged). The linear function is $Y_1' = 10 + 0.15X_1'$ with $R^2 = 0.0243$ and $RMSE = 6.17$ $\mu g/m^3$.

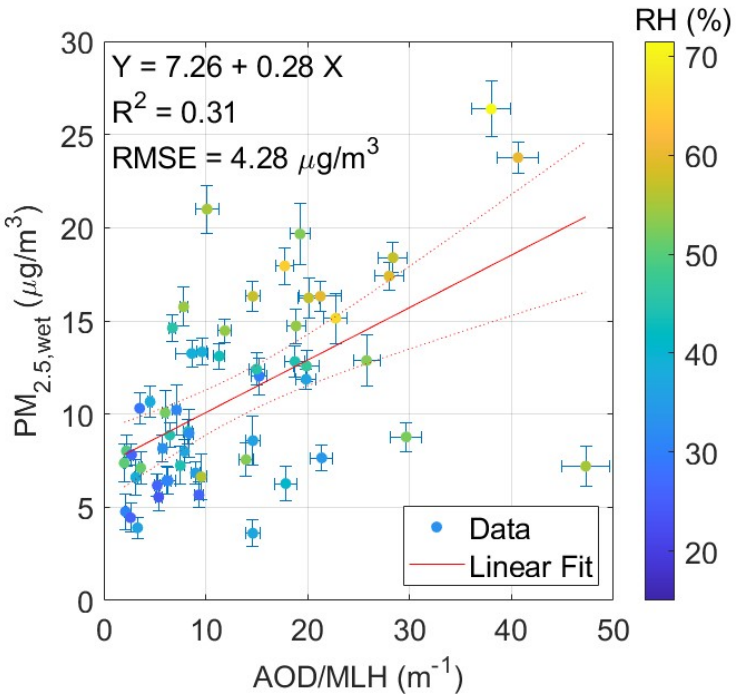

(a)

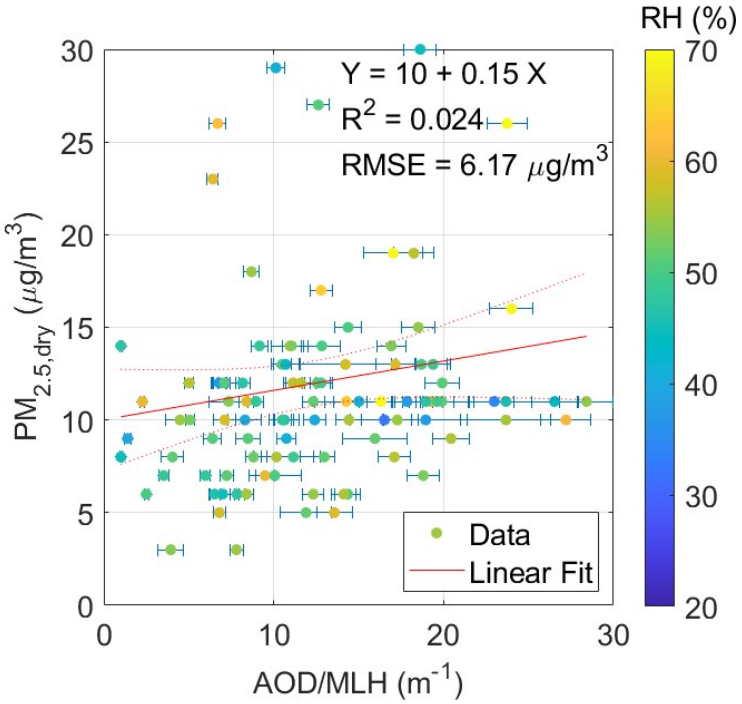

(b)

Figure 4.3: Results from the linear regressions. (**a**) Linear regression between $Y = PM_{2.5,wet}$ and $X = \frac{AOD}{MLH}$ (no auxiliary data). (**b**) Linear regression between $Y' = PM_{2.5,dry}$ and $X' = \frac{AOD}{MLH}$ (daily averages). In the two cases, data points are color-coded with the average hourly and daily RH respectively.

Auxiliary data	R	R^2	**RMSE**	a **(SE)**	b **(SE)**
None	0.5587	0.312	4.28	0.282 + 40%	7.26 + 26%
All (r_{eff})	0.7610	0.579	3.11	0.812 ± 24%	6.27 ± 23%
All (r'_{eff})	0.7337	0.538	3.03	**1.042**± 27%	6.38±23%

Table 4.2: Results from the linear regressions with the function $Y = aX + b$, where $Y = PM_{2.5,wet}$ and X depends on which auxiliary data is used. The regressions were performed on 49 data points apart from the first, which was performed on 56 data points. The coefficients a and b are listed with Standard Error (SE) with 95% confidence bounds.

With auxiliary data

We perform the linear regressions between $\mathrm{PM}_{2.5,wet}$ measured by LOAC and calculated as $X = \frac{4\rho_{aer} r_{eff}}{3\langle Q_{ext,aer}\rangle} \frac{AOD}{MLH}$.

The Pearson's correlation coefficient is 0.76, indicating a greater linear agreement between the variables. The linear regression function has $RMSE = 3.11$ μg/m^3 and $R^2 = 0.58$, which indicates a better linear fit. The linear function, presented in Figure 4.4a, is $Y = 6.27 + 0.81 \cdot AX$.

As we have seen previously, the Effective Radius calculated from LOAC PN measurements is usually overestimated with respect to the theoretical one. For this reason, we perform a linear regression with the corrected values $r'_{eff,LOAC}$. In this case, the slope of the linear function reaches a value of $a = 1.04$ with $R^2 = 0.54$, $RMSE = 3.03$ μg/m^3 and $R = 0.73$ (shown in Figure 4.4b).

In both cases, the distribution of the residuals has a normal shape that is slightly negatively skewed; with an average close to 0 and a median of -0.2. Scatterplot analysis (not shown) of the residuals (estimated - empirical PM values) evidences no dependence on any of the involved parameters ($\mathrm{PM}_{2.5,wet}$, AOD, MLH, r_{eff}, $\langle Q_{ext,aer}\rangle$, and ρ_{aer}).

Table 4.2 summarizes the linear correlation results obtained in each case considered so far. The values of the offset b in all linear functions are compatible with each other within confidence bounds. This means that the offset depends on other factors, such as the difference between the point measurements (LOAC and ceilometer data) and the satellite AOD retrieval (with a footprint of 1 km^2). Theoretically, the slope of the linear function between $\mathrm{PM}_{2.5,wet}$ and $X = A\frac{AOD}{MLH}$ should be close to 1, as A represents the theoretical slope that relates $\mathrm{PM}_{2.5}$ to AOD and should account for all the variability.

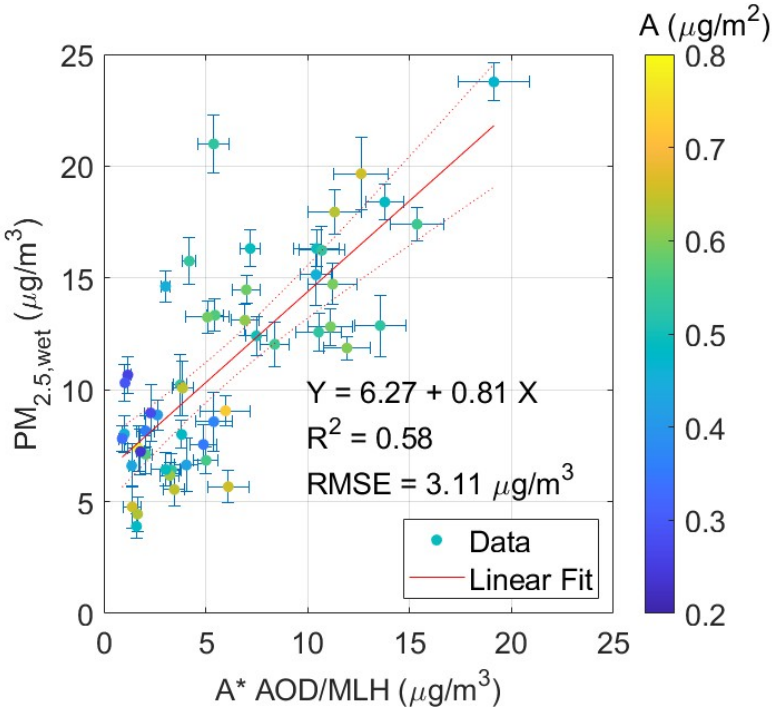

(a)

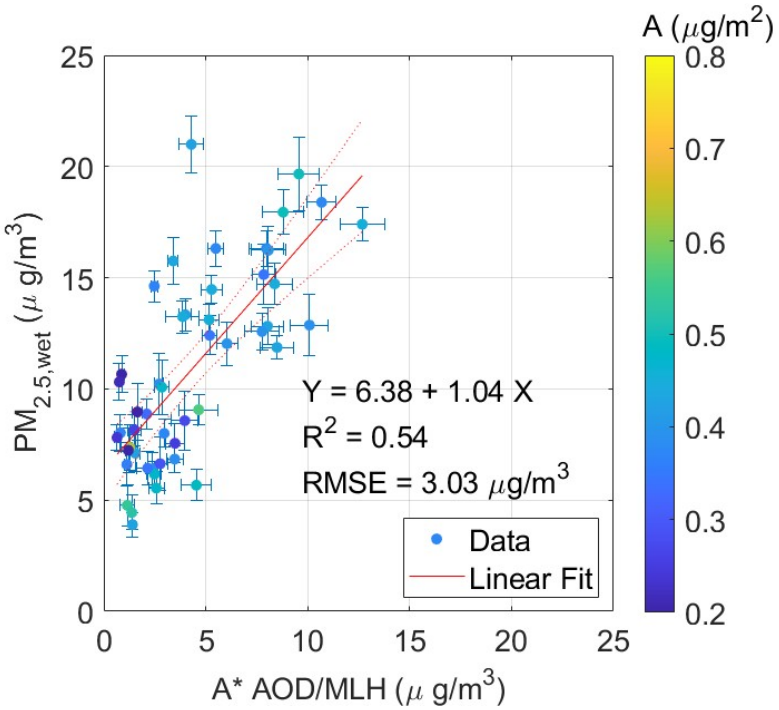

(b)

Figure 4.4: Results from the linear regressions with auxiliary data. (**a**) Linear regression between $Y = PM_{2.5,wet}$ and $A\frac{AOD}{MLH}$. (**b**) Linear regression between $Y = PM_{2.5,wet}$ and $A_1\frac{AOD}{MLH}$, where A_1 is computed with the new values of r_{eff}. In both cases, the data points are color-coded with the respective values of A and A_1.

Variable importance assessment

Lastly, we assess the variable importance of r_{eff}, $\langle Q_{ext,aer} \rangle$ and ρ_{aer} by adding one variable at a time to $X = \frac{AOD}{MLH}$ and comparing the Pearson's coefficient values. Each time we add one variable, we select only the data with relative uncertainty lower than 20%.

We consider the linear correlation coefficient R = 0.5587 between $PM_{2.5,wet}$ and $X = \frac{AOD}{MLH}$ as the starting point. We multiply by r_{eff} and obtain R = 0.5992 between $PM_{2.5,wet}$ and $X = \frac{AOD}{MLH} r_{eff}$. Secondly, we multiply by $\langle Q_{ext,aer} \rangle$ and obtain R = 0.6082. Lastly, we multiply by $\frac{4}{3}\rho_{aer}$ and obtain R = 0.6103 between $PM_{2.5,wet}$ and $X = A\frac{AOD}{MLH}$. The last value is lower than the one obtained in the previous analysis because in this case we have considered data points with uncertainties greater than 2 μg/m^3 on X.

4.4.5 Discussion

The Pearson's correlation coefficient $R = 0.56$ shows that the "wet" hourly $PM_{2.5}$ is linearly correlated to AOD, even without using information about aerosol properties, while the MLH is always considered. For comparison, the correlation between AOD and "dry" $PM_{2.5}$ from reference ground-based measurements only has a coefficient $R = 0.16$, indicating the absence of a linear correlation. We note that the temporal resolution of "dry" $PM_{2.5}$ is lower than that of the LOAC-derived, "wet" $PM_{2.5}$, which can partially explain the lower value of R. It also underlines the need for reference data with a better temporal resolution.

The "wet" $PM_{2.5}$ is representative of the mass concentration of the particulate matter in humidity conditions, consistent with the AOD satellite measurement. The analysed data show that higher values of both $PM_{2.5,wet}$ and AOD are generally associated to higher values of RH, contrary to "dry" $PM_{2.5}$ which is measured at fixed RH values lower than 50%. By using PM observations taken at ambient humidity, we can correlate PM and AOD without the use of hygroscopic corrections. This is an element of novelty with respect to previous works on the same topic, while reaching results comparable to previous studies (Koelemeijer et al., 2006; Di Nicolantonio et al., 2009; Ferrero et al., 2019; Arvani et al., 2016). A hygroscopic correction is still needed to calculate the "dry" $PM_{2.5}$ from the "wet" $PM_{2.5}$ calculated from AOD with this method.

The correlation between $PM_{2.5,wet}$ and $\frac{AOD}{MLH}$ shows no significant dependence on the time of day within our sampling window (9AM-2PM). Analysis of Terra (morning) vs. Aqua (afternoon) overpasses revealed comparable scatter in both cases, despite the expected MLH evolution during this period (not shown). This suggests that the normalization by MLH adequately accounts for diurnal boundary layer variations within the satellite overpass timeframe.

The substantial improvement when incorporating the physics-informed coefficient (R increases from 0.56 to 0.76) confirms that local aerosol microphysical properties significantly affect the AOD-PM relationship. The coefficient of determination $R^2 = 0.58$ is comparable to previous studies (Di Nicolantonio et al., 2009; Wang et al., 2009), with the important advantage that our linear function remains valid across the entire study period (February-September) without requiring seasonal tuning or monthly calibration.

The slope of the linear function in this case is 0.82, which is lower than the perfect fit value of 1. This means that the applied corrections do not fully relate the measured and the calculated $PM_{2.5,wet}$. This is an expected conclusion due to the high relative uncertainty of the calculated A, which in turn is due to the high relative uncertainty of r_{eff}.

By repeating the linear regression with an alternative calculation of r_{eff}, the slope of the linear function reaches a value of 1.04 while maintaining a comparable goodness of fit ($R^2 = 0.54$), relative error on coefficients ($24 - 27\%$), and Pearson's coefficient ($R = 0.73$). The alternative r_{eff} is calculated by extrapolating Particle Number concentration for smaller particles, which are not measured by the LOAC, but are not negligible in the computation of aerosol optical properties. The new r_{eff} values are lower than the original ones while maintaining comparable uncertainties. A better estimate of r_{eff} allows us to compute more accurately the parameter A to compute the $PM_{2.5}$ from satellite AOD.

The assessment of variable importance shows that the uncertainty assigned to r_{eff} and X greatly impacts the linear correlation. By considering X data with relative uncertainties lower than 20%, the Pearson's linear coefficient increases by 5% from considering $X = \frac{AOD}{MLH}$ to $X = A\frac{AOD}{MLH}$: in particular, adding r_{eff} increases R by 4%, while adding also $\langle Q_{ext,aer} \rangle$ and ρ_{aer}, increases R by another 1%. For comparison, considering an absolute uncertainty lower than 2 $\mu g/m^3$ for both $Y = PM_{2.5,wet}$ and $X = A\frac{AOD}{MLH}$, R increases by another 15%, with a total of 20% increase from 0.56 to 0.76.

Our methodology takes into account the theoretical relationship between PM mass concentration and total aerosol extinction, and is able to correlate them with a slope close to 1. Similarly to previous studies, an offset is needed in the linear correlation to account for factors other than aerosol properties and meteorology (e.g., local traffic).

An appropriate correction is also needed to compare the "wet" $PM_{2.5}$ retrieved from satellite data with standard measurements of "dry" $PM_{2.5}$. It should consist of an empirical function whose coefficients are related and fine-tuned in accordance with the aerosols features of the considered location.

4.5 Conclusions

In the present work, we analysed $PM_{2.5}$ data obtained at ambient humidity ("wet" $PM_{2.5}$) from a LOAC optical particle counter and co-located satellite AOD retrieved at high spatial resolution. The use of "wet" $PM_{2.5}$ instead of the standard "dry" $PM_{2.5}$ provides a direct comparison between ground-based PM and satellite AOD without the need for empirical hygroscopic correction functions. This resulted in a moderate linear correlation between $PM_{2.5}$ and AOD normalized by the mixing layer height (Pearson's linear coefficient R = 0.56), while no significant correlation was found when using reference "dry" $PM_{2.5}$ measurements.

In addition, the exploitation of aerosol microphysical and optical properties derived from LOAC measurements (particle size distribution, effective radius, extinction efficiency, and mass density) enabled the estimation of a theoretical coefficient linking $PM_{2.5}$ and AOD at ambient conditions. When this physics-informed coefficient was included in the analysis, the linear correlation substantially improved (R = 0.76). This confirms that explicitly accounting for aerosol properties enhances the physical consistency and robustness of satellite-based PM estimates, and allows the same linear relationship to be applied across different seasons without requiring seasonal tuning. Although the analysed period (February–September 2023) does not cover a full annual cycle, the results demonstrate a stable linear behaviour across a wide range of meteorological conditions and aerosol regimes. Extending the temporal coverage will be essential to assess the long-term applicability of the proposed methodology and its sensitivity to inter-annual variability.

When using OPC data, the lower limit in particle size detection causes an overestimation of the Effective Radius, which needs to be addressed depending on the instrument characteristics and the local aerosol environment. In this study, the effective radius was corrected by extrapolating particle number concentrations for sizes below the LOAC detection limit (0.2 μm). The corrected Effective Radius, which is on average 70% smaller than the original one, improved the agreement between measured and satellite estimated $PM_{2.5}$, yielding regression slopes closer to the theoretical value of one. This highlights the central role of the effective radius in physically linking aerosol optical and mass properties.

Finally, while the present approach enables the estimation of ambient ("wet") $PM_{2.5}$ from satellite observations without hygroscopic corrections, an additional step is required to relate these estimates to regulatory dry $PM_{2.5}$ measurements. In this context, the proposed framework provides a promising basis for indirectly deriving aerosol hygroscopic growth factors by coupling satellite-based wet $PM_{2.5}$ with co-located dry PM observations. This perspective opens new opportunities for characterizing aerosol–humidity interactions from space and for improving air quality assessments in regions with limited ground-based monitoring.

Chapter 5

Conclusions

This thesis developed and validated a physics-informed methodology for estimating ground-level $PM_{2.5}$ from satellite-derived AOD in urban areas, applied to Bologna (Po Valley) during February-September 2023. The methodology addresses fundamental limitations in existing PM-AOD correlation approaches: firstly, by using measurements at ambient humidity to eliminate empirical hygroscopic corrections; secondly, by deriving the PM-AOD linear coefficient from aerosol microphysical properties (effective radius, extinction efficiency, mass density) within a physically consistent theoretical framework.

5.1 Summary and main contributions

5.1.1 Research context and motivation

The World Health Organization recognizes air pollution as the single largest environmental threat to human health, with Particulate Matter $PM_{2.5}$ exposure linked to cardiovascular disease, respiratory illness, and lung cancer. Despite these severe health impacts, ground-based PM monitoring networks remain insufficient for global coverage, with only 3-4 monitors per million inhabitants in Europe and even sparser coverage in low- and middle-income countries where pollution is often highest. Satellite-based Aerosol Optical Depth (AOD) retrievals offer a promising complement, but translating columnar AOD to surface $PM_{2.5}$ requires careful consideration of local aerosol properties and atmospheric conditions.

The primary challenge in existing methodologies is the measurement mismatch. Satellite AOD is retrieved at ambient Relative Humidity (RH), while standard PM measurements are performed under dry conditions ($RH < 50\%$). To relate AOD to PM, we need an hygroscopic correction function whose empirical coefficients depend strongly on local aerosol characteristics, limiting transferability across re-

gions. Studies in the Po Valley found that incorporating such corrections did not significantly improve correlations, while most existing methodologies require seasonal recalibration.

Rather than applying empirical hygroscopic corrections, the presented methodology exploits $PM_{2.5}$ measurements obtained at ambient RH from an Optical Particle Counter, the Light Optical Aerosol Counter (LOAC). This enabled the direct comparison with satellite AOD without hygroscopic corrections.

Secondly, statistical and machine learning methods often treat the AOD-PM relationship as a black box, lacking physical interpretability and requiring extensive training data or seasonal recalibration. This methodology estimates the linear coefficient based on the theoretical relationship between aerosol mass concentration and optical properties. Three key aerosol properties were derived from LOAC measurements: effective radius from particle size distributions, average mass density from particle type classification, and average extinction efficiency from particle type fractions and Mie theory.

5.1.2 Methodological developments and main results

Implementing the physics-informed approach included several technical challenges.

1. Optical particle counter operation at ambient conditions. Using the LOAC at ambient humidity enabled direct comparison with satellite AOD, but required careful quality control to exclude precipitation and dust events that cause anomalous $PM_{2.5}$ and Effective Radius values.

2. Derivation of aerosol optical properties. Computing the theoretical coefficient required estimating effective radius, extinction efficiency, and mass density from LOAC particle number concentrations (0.2-30 μm) and particle type classification. Extinction efficiency values were obtained by matching LOAC particle types to OPAC aerosol components using Mie theory.

3. Correction for detection limit bias. The LOAC's lower detection limit (0.2 μm diameter) excludes ultrafine particles that contribute significantly to optical properties but negligibly to mass. Numerical simulations revealed uncorrected effective radius overestimates the true value by factors of 1.5-2. An extrapolation methodology was developed that reduced this systematic error from 150-200% to 10-20%.

4. Careful uncertainty quantification. Systematic quality filtering was applied to exclude precipitation events, dust intrusions, and unstable aerosol conditions, reducing the dataset from 985 satellite overpasses to 49-56 high-quality observations but substantially improving correlation.

After addressing these challenges, the presented methodology achieved substantial results. Direct comparison between PM and AOD at ambient RH yielded

a moderate linear correlation (R = 0.56), while no meaningful correlation (R = 0.16) was found using standard dry $PM_{2.5}$ measurements.

Incorporating aerosol microphysical properties improved correlation from R = 0.56 to R = 0.76, representing a 36% increase and nearly doubling the explained variance (R^2 from 0.31 to 0.58). When using the corrected Effective Radius, the linear regression slope reached 1.04 ± 0.27, essentially achieving the theoretical value of unity. Without the correction, the slope was 0.81, systematically underestimating $PM_{2.5}$ variability by 20%.

The methodology maintained consistent performance throughout the measurement period (February-September 2023) without requiring seasonal calibration, unlike previous studies that derive seasonal coefficients. The same linear relationship remained valid across diverse meteorological conditions and aerosol regimes.

Sensitivity analysis confirmed the Effective Radius as the dominant parameter (increasing R by 4%), with extinction efficiency and mass density providing secondary contributions (additional 1%). Careful uncertainty quantification proved critical for achieving optimal performance. Lastly, the persistent linear regression offset of approximately 6 $\mu g/m^3$ across all formulations likely arises from spatial resolution mismatch between satellite observations (1 km^2) and point measurements.

5.2 Limitations and future perspectives

Several limitations suggest directions for future development.

The measurement period excludes autumn and winter months (October-January) when Po Valley pollution is highest, and all measurements are from a single location. Extension to full annual cycles and multiple sites would assess year-round applicability and spatial heterogeneity.

Moreover, alternative data sources could be used, such as particle size distributions from AERONET aerosol inversions, scanning mobility particle sizers, or other instruments, enabling assessment of robustness and identification of optimal instrument combinations. Upcoming satellite missions (Sentinel-4, MAIA) will provide higher spatial and temporal resolution AOD retrievals. Geostationary platforms offer particular promise for capturing diurnal AOD variations and improving temporal matching with ground measurements.

The Effective Radius correction is specific to the LOAC detection limit. Different optical particle counters would require adapted corrections. Additionally, particle type classification provides limited compositional information; direct chemical measurements would better constrain hygroscopic and optical properties.

The estimated linear coefficient A could be incorporated into machine learning models, combining physical interpretability with the flexibility to capture complex

non-linear relationships while maintaining physical constraints.

While the approach estimates ambient $PM_{2.5}$ without hygroscopic corrections, relating these estimates to regulatory dry $PM_{2.5}$ measurements requires additional steps. The methodology could benefit from coupling wet $PM_{2.5}$ with co-located dry PM observations to derive hygroscopic growth factors.

5.3 Concluding remarks

This thesis demonstrates that explicitly accounting for aerosol microphysical and optical properties, combined with ambient-condition measurements that naturally incorporate hygroscopic effects, significantly enhances the physical consistency and robustness of satellite-based $PM_{2.5}$ estimates. The physics-informed methodology achieves performance comparable to previous semi-empirical approaches in the Po Valley while offering greater temporal stability, physical interpretability, and independence from empirical hygroscopic corrections.

The key finding is that using PM measurements at ambient humidity eliminates the need for uncertain hygroscopic correction functions while maintaining good correlation with satellite AOD. When combined with aerosol microphysical properties derived from optical particle counter measurements, the methodology achieves correlation coefficients ($R = 0.76$) and regression slopes (1.04) that validate the theoretical framework. The correction for optical particle counter detection limit bias proved essential, highlighting an important consideration for any methodology employing such instruments.

The work contributes to ongoing efforts to expand PM monitoring capabilities beyond traditional ground-based networks, with particular relevance for regions where air quality monitoring infrastructure remains limited despite elevated pollution levels. The lower cost and portability of optical particle counters, compared to reference instrumentation, may enable deployment of the auxiliary measurements needed for the physics-informed methodology in areas where traditional monitoring is not feasible.

By providing a physically grounded framework for relating satellite AOD to ground-level PM, this research advances the use of satellite remote sensing for air quality assessment and public health applications. The methodology is particularly suited to urban areas and regions like the Po Valley where aerosols are well-mixed below a well-defined boundary layer, but the general framework can be extended to other locations with similar instrumentation and aerosol characteristics.

Future work should focus on extending temporal coverage to full annual cycles, validating the approach across multiple urban sites with different aerosol characteristics, and developing operational implementations that can provide real-time PM estimates for air quality management and public health warning systems.

Appendix A

Aerosol Optical Properties

In the following chapter, we present two works that complement the thesis.

Firstly, we describe the structure of a database of optical properties, which comprises aerosol and cloud particles.

Secondly, we describe a code to calculate the PSD properties of an aerosol mixture based on the aerosol model present in the Global Aerosol Data Set (Kopke et al., 1997; Hess et al., 1998).

A.1 Aerosol Properties Database

The knowledge of realistic optical properties is crucial when using Radiative Transfer models to simulate the effects of cloud or aerosol layers. A better characterization of clouds and aerosols improves the retrieval and classification algorithms applied to satellite data with the aim of identifying scattering and absorbing layers in the atmosphere and their radiative effect.

The optical properties included in this database have been used in recent studies to simulate high resolution measurements in the Infrared range, by sensors such as IASI (Masiello et al., 2024; Donat et al., 2024; Serio et al., 2024). The development of the database has also been involved in the CASIA project related to CAIRT mission (ASI-CASIA, 2024).

For each particle type, the appropriate spectral Refractive Index, Particle Radius range, and PSD parameters are chosen from the literature. Then, the single particle properties are computed with the code Scattnlay, described in Peña and Pal (2009). Lastly, the Bulk properties are computed by integration of single particle properties over the chosen PSD. An additional step is the parameterization of selected Bulk properties as a grade 6 polynomial. The particle mass density ρ is also included in the database as it is necessary to calculate the total ratiative effects. Table A.1 summarizes all particle types, with the respective RI, Radii,

PSD parameters and mass density.

A.1.1 Optical Properties

Particles

The aerosol particles included in the database are the following:

- Soluble aerosols at $RH = 50\%$;
- Insoluble aerosols;
- Black carbon (soot);
- Mineral dust;
- Volcanic ash (pumice and andesite ash), both uncoated and coated with ice.

where Soluble, Insoluble and Black Carbon are used to calculate the urban aerosol properties in A.2.

Other particles included are the following:

- Ice clouds (four different habits of irregular shaped ice crystals);
- Water and mixed clouds (spherical particles made up of water and of water coated with ice);
- Polar Stratospheric Clouds (three different types of spherical or irregular shaped particles made of ice of ternary solutions, with a lognormal PSD);
- Sub-Visible Cirri (spherical or irregular shaped ice particles with an exponential PSD).

Single Particle Properties

The single particle properties are computed with the code Scattnlay (Peña and Pal, 2009). This code performs calculations of optical properties according to Mie theory and considering spherical particles. With this code it is possible to compute properties for multi-layered spheres, for example particles coated by ice or water.

The input variables for the computation are the spectral Refractive Index (RI) of the particle with associated wavelengths λ, and the particle radius R. The size parameter $x = \frac{2\pi R}{\lambda}$ is computed as a requirement for the Scattnlay code. We choose the appropriate radii values according to the typical dimensions of the selected particle type, in order to compute the properties for a set of chosen particle radii. The outputs of the Scattnlay code are:

Particle Type	**RI + ρ**	**Single Particle**	**PSD**
Soluble	$\rho = 1.8\ g/cm^3$ Hess et al. (1998)	$R = 10^{-4} - 25\mu m$	$r_{eff} = 0.01 - 20\mu m$ $\sigma = 0.53$
Insoluble	$\rho = 2\ g/cm^3$ Hess et al. (1998)	$R = 10^{-4} - 25\mu m$	$r_{eff} = 0.01 - 20\mu m$ $\sigma = 0.53$
Black Carbon	$\rho = 1\ g/cm^3$ Twitty and Weinman (1971)	$R = 10^{-4} - 25\mu m$	$r_{eff} = 0.01 - 20\mu m$ $\sigma = 0.69$
Mineral Dust	$\rho = 2.6\ g/cm^3$ Volz (1972)	$R = 10^{-4} - 25\mu m$	$r_{eff} = 0.01 - 20\mu m$ $\sigma = 0.73$
Volcanic Ash 1	$\rho = 1.92\ g/cm^3$ Volz (1973)	$R = 10^{-4} - 25\mu m$	$r_{eff} = 0.01 - 20\mu m$ $\sigma = 0.53$
Volcanic Ash 2	$\rho = 2.7\ g/cm^3$ Pollack et al. (1973)	$R = 10^{-4} - 25\mu m$	$r_{eff} = 0.01 - 20\mu m$ $\sigma = 0.53$
Volcanic Coated	$\rho = 1.92\ g/cm^3$ Volz (1973), Warren and Brandt (2008)	$R = 10^{-4} - 25\mu m$	$r_{eff} = 0.01 - 20\mu m$ $\sigma = 0.53$
Ice clouds	$\rho = 0.92\ g/cm^3$ Yang et al. (2012)	$D = 1 - 5000\mu m$	$r_{eff} = 2 - 200\mu m$ $\sigma = 0.1$
Water clouds	$\rho = 1\ g/cm^3$ Downing and Williams (1975)	$R = 0.01 - 100\mu m$	$r_{eff} = 0.5 - 30\mu m$ $\sigma = 0.1$
Mixed clouds	Downing and Williams (1975) Warren and Brandt (2008)	$R = 0.01 - 40\mu m$	$r_{eff} = 0.5 - 30\mu m$ $\sigma = 0.1$

Table A.1: Summary of particle types present in the database and the respective input parameters for the computation. **Aerosol particles**: RI wavelength range is $\lambda = 0.2 - 40\mu m$; particles are considered spherical; PSD is a lognormal (Eq. A.1). **Cloud particles:** RI wavelength range is $\lambda = 3.5 - 200\mu m$; particles are spherical (water and mixed clouds) or have a particular shape; PSD is a gamma (Eq. A.2).

- Extinction, scattering and absorption efficiencies: Q_{ext}, Q_{sca}, Q_{abs};
- Asymmetry parameter: g;
- Single Scattering Albedo (SSA): ω_0;
- Phase matrix: P_{11}.

The projected area A and the particle volume V are also computed. Note that the optical cross-sections σ are obtained by the efficiencies Q by multiplication with the cross-sectional area A as in Eq. 2.4. Moreover, the coefficients k (such as k_{ext} considered for aerosols in Chapter 2.1 onward) are obtained from σ by multiplication with the concentration of the particles in the layer, or integration by the PSD as in Eq. 2.7.

Bulk Properties

The single particle properties are integrated over a Particle Size Distribution (PSD) whose parameters depend on the particle type. For aerosol particles, we assume a lognormal PSD:

$$n(r) = \frac{n_0}{\sqrt{2\pi}\sigma r} \exp \frac{-\ln (r/r_0)^2}{2\sigma^2} \tag{A.1}$$

where the associated parameters are the width or scale σ and the modal radius r_0. The Effective Radius r_{eff}, as already defined in Eq. 2.8, is used as an index in the database; it is related to the modal radius by the relation $r_{eff} = r_0 e^{\frac{5}{2}\sigma^2}$.

For cloud particles, we assume a gamma PSD:

$$n(D) = n_0 D^{\mu} e^{-\lambda D} \tag{A.2}$$

where μ is the shape parameter (different for ice and water clouds), λ is the slope parameter, n_0 is the normalization factor and D is the maximum dimension of the cloud particle (which corresponds to the diameter for regular spherical particles). In this case, the Effective Radius is defined as half the Effective Dimension:

$$D_{eff} = \frac{3}{2} \frac{\int V(D) n(D) dD}{\int A(D) n(D) dD} \tag{A.3}$$

where $V(D)$ and $A(D)$ are the volume and cross-sectional area of the particle, respectively.

All the optical properties are computed and normalized to a PSD of 1 particle per cm^3.

The bulk properties included in the database are:

- Projected cross-sectional area (μm^2),
- Volume (μm^3),
- Extinction and Absorption Efficiencies (adimensional),
- Extinction and Absorption Cross-sections (μm^2),
- Single Scattering Albedo (adimensional),
- Asymmetry Parameter (adimensional),
- Phase Function (adimensional).

All the properties apart from A and V are wavelength dependent, and the Phase Function is also dependent on the scattering angle Θ.

Parametrization of Bulk properties

In some applications, it is useful to describe the optical properties as parametrized quantities. Retrieval codes require knowledge of the Jabobian matrix of each parameter, which can be easily obtained by their analytical form. Moreover, it can be useful to reduce the size of the datasets when dealing with a lot of data.

The parametrization used in the dataset is a 6th grade polynomial depending on the Effective Radius, for each wavenumber:

$$p_i = \Theta_{i,0} + \Theta_{i,1}x + \Theta_{i,2}x^2 + \Theta_{i,3}x^3 + \Theta_{i,4}x^4 + \Theta_{i,5}x^5 + \Theta_{i,6}x^6 \tag{A.4}$$

where p_i is the bulk property Q_{ext}, ω_0 or b, $\Theta_{i,j}$ are the coefficients, determined with a least-square approach. The parameter x is defined as:

$$x = \frac{1}{r_{eff} + t} \tag{A.5}$$

where t is a translation constant included to avoid non-physical values and to maximize the coefficient of determination R^2 of the fit.

The parametrization accuracy for each case is assessed by comparing the original property and the property computed by using the respective parameters and values of r_{eff}. For each wavelength, the goodness of fit is described by the percentage residuals, the RMSE, and the R^2. In general, for aerosol particles the RMSE is below 10^{-2} for every wavelength, $R^2 > 0.99$, and the residual percentages are below 3% apart from particular cases, in which they are below 10%. A more thorough analysis is not the scope of the present work.

A.2 Urban aerosol PSDs

In the following, we describe the code to calculate the urban aerosol PSDs used in Chapter 4.2 to compare the theoretical values of Effective Radius with the ones calculated from LOAC measurements.

A.2.1 Code description

This code calculates the PSD, Effective Radius and bulk optical properties of an urban aerosol mixture defined in input. It can also calculate the theoretical PM2.5 and PM10 in a unitary atmospheric level (for example, near the surface) with the defined mixture. It also calculates an idealized LOAC measurement by integration of the PSD within the LOAC size bins (Table 3.3).

The Urban aerosol mixture is defined as in the OPAC database (Kopke et al., 1997) as a mixture of Soluble and Insoluble aerosol types with the addition of Black Carbon. Other aerosol types can be included for particular case studies, such as Mineral Dust to study cases of dust transport. All the properties and PSD parameters used in the code have been included in the Aerosol Database in Section A.1.

The code requires the total Particle Number concentration N_{tot} (cm^{-3}) as well as the mixing ratios, in percentages, of each aerosol type. The mixing ratios are equivalent to the Number Ratios defined in Eq. 3.4, with the difference that in this case only one value is needed for all radii.

Each aerosol type has its own set of fixed parameters for the computation of the theoretical PSD as defined in Eq. A.1, normalized to 1 particle per cm^3. The particle radii used to compute the partial PSDs are 450 values in the range $0.05 - 20\mu m$. The partial PSDs $n_i(r)$ are summed with the respective mixing ratio mix_i and multiplied by N_{tot} to compute the theoretical PSD of the aerosol mixture:

$$n(r) = N_{tot} \sum_i n_i(r)\, mix_i. \tag{A.6}$$

The theoretical Effective Radius can be calculated by integration using Eq. 2.8.

A LOAC measurement can be simulated assuming a flat distribution in each size bin, integrating the PSD values within the bin edges defined in Table 3.3 as in Eq. 3.1. The LOAC Effective Radius can then be calculated as in Eq. 3.3 and compared to the theoretical value.

Bibliography

AERONET (2025). Aerosol Robotic Network (AERONET) homepage. https://aeronet.gsfc.nasa.gov/new_web/index.html. Accessed 2025-06-30.

Aggarwal, S. G., Kumar, S., Mandal, P., Sarangi, B., Singh, K., Pokhariyal, J., Mishra, S. K., Agarwal, S., Sinha, D., Singh, S., Sharma, C., and Gupta, P. K. (2013). Traceability issue in pm2.5 and pm10 measurements. *MAPAN*, 28(3):153–166.

Almeida, S. M., Pio, C. A., Freitas, M. C., Reis, M. A., and Trancoso, M. A. (2006). Source apportionment of atmospheric urban aerosol based on weekdays/weekend variability: evaluation of road re-suspended dust contribution. *Atmospheric Environment*, 40(11):2058–2067.

Anderson, J. O., Thundiyil, J. G., and Stolbach, A. (2011). Clearing the air: A review of the effects of particulate matter air pollution on human health. *Journal of Medical Toxicology*, 8(2):166–175.

ARPAE (2025). Arpae Emilia-Romagna. https://www.arpae.it/it. Accessed 2025-06-30.

Arvani, B., Pierce, R., Lyapustin, A., Wang, Y., Ghermandi, G., and Teggi, S. (2016). Seasonal monitoring and estimation of regional aerosol distribution over po valley, northern italy, using a high-resolution maiac product. *Atmospheric Environment*, 141:106–121.

ASI-CASIA (2024). ASI-CASIA – CAIRT: Analisi e Sinergia con IASI-NG (CASIA) — Istituto di Scienze dell'Atmosfera e del Clima. https://www.isac.cnr.it/en/projects/asi-casia-cairt-analisi-e-sinergia-con-iasi-ng-casia.

Barnaba, F., Putaud, J., Gruening, C., dell'Acqua, A., and Santos, S. D. (2010). Annual cycle in co-located in situ, total-column, and height-resolved aerosol observations in the po valley (italy): Implications for ground-level particulate

matter mass concentration estimation from remote sensing. *Journal of Geophysical Research Atmospheres*, 115(D19).

Baron, P. A. and Willeke, K. (2001). *Aerosol measurement: principles, techniques, and applications*. John Wiley & Sons.

Beelen, R., Raaschou-Nielsen, O., Stafoggia, M., Andersen, Z. J., Weinmayr, G., Hoffmann, B., Wolf, K., Samoli, E., Fischer, P., Nieuwenhuijsen, M., Vineis, P., Xun, W. W., Katsouyanni, K., Dimakopoulou, K., Oudin, A., Forsberg, B., Modig, L., Havulinna, A. S., Lanki, T., Turunen, A., Oftedal, B., Nystad, W., Nafstad, P., Faire, U. D., Pedersen, N. L., Östenson, C.-G., Fratiglioni, L., Penell, J., Korek, M., Pershagen, G., Eriksen, K. T., Overvad, K., Ellermann, T., Eeftens, M., Peeters, P. H., Meliefste, K., Wang, M., Bueno-De-Mesquita, B., Sugiri, D., Krämer, U., Heinrich, J., Hoogh, K. D., Key, T., Peters, A., Hampel, R., Concin, H., Nagel, G., Ineichen, A., Schaffner, E., Probst-Hensch, N., Künzli, N., Schindler, C., Schikowski, T., Adam, M., Phuleria, H., Vilier, A., Clavel-Chapelon, F., Declercq, C., Grioni, S., Krogh, V., Tsai, M.-Y., Ricceri, F., Sacerdote, C., Galassi, C., Migliore, E., Ranzi, A., Cesaroni, G., Badaloni, C., Forastiere, F., Tamayo, I., Amiano, P., Dorronsoro, M., Katsoulis, M., Trichopoulou, A., Brunekreef, B., and Hoek, G. (2013). Effects of long-term exposure to air pollution on natural-cause mortality: an analysis of 22 european cohorts within the multicentre escape project. *The Lancet*, 383(9919):785–795.

Bhandari, J., China, S., Chandrakar, K. K., Kinney, G., Cantrell, W., Shaw, R. A., Mazzoleni, L. R., Girotto, G., Sharma, N., Gorkowski, K., Gilardoni, S., Decesari, S., Facchini, M. C., Zanca, N., Pavese, G., Esposito, F., Dubey, M. K., Aiken, A. C., Chakrabarty, R. K., Moosmüller, H., Onasch, T. B., Zaveri, R. A., Scarnato, B. V., Fialho, P., and Mazzoleni, C. (2019). Extensive soot compaction by cloud processing from laboratory and field observations. *Scientific Reports*, 9:11824.

Bourgeois, Q., Ekman, A. M. L., Renard, J.-B., Krejci, R., Devasthale, A., Bender, F. A.-m., Riipinen, I., Berthet, G., and Tackett, J. L. (2018). How much of the global aerosol optical depth is found in the boundary layer and free troposphere? *Atmospheric chemistry and physics*, 18(10):7709–7720.

Brattich, E., Bracci, A., Zappi, A., Morozzi, P., Di Sabatino, S., Porcù, F., Di Nicola, F., and Tositti, L. (2020). How to Get the Best from Low-Cost Particulate Matter Sensors: Guidelines and Practical Recommendations. *Sensors*, 20(11):3073.

Brook, R. D., Rajagopalan, S., Pope, C. A., Brook, J. R., Bhatnagar, A., Diez-Roux, A. V., Holguin, F., Hong, Y., Luepker, R. V., Mittleman, M. A., Peters,

A., Siscovick, D., Smith, S. C., Whitsel, L., and Kaufman, J. D. (2010). Particulate matter air pollution and cardiovascular disease. *Circulation*, 121(21):2331–2378.

Brunekreef, B. and Holgate, S. T. (2002). Air pollution and health. *The Lancet*, 360(9341):1233–1242.

Carbone, C., Decesari, S., Mircea, M., Giulianelli, L., Finessi, E., Rinaldi, M., Fuzzi, S., Marinoni, A., Duchi, R., Perrino, C., Sargolini, T., Vardè, M., Sprovieri, F., Gobbi, G., Angelini, F., and Facchini, M. (2010). Size-resolved aerosol chemical composition over the italian peninsula during typical summer and winter conditions. *Atmospheric Environment*, 44(39):5269–5278.

Charron, A., Harrison, R. M., Moorcroft, S., and Booker, J. (2003). Quantitative interpretation of divergence between pm10 and pm2.5 mass measurement by teom and gravimetric (partisol) instruments. *Atmospheric Environment*, 38(3):415–423.

Chen, J., De Hoogh, K., Gulliver, J., Hoffmann, B., Hertel, O., Ketzel, M., Bauwelinck, M., Van Donkelaar, A., Hvidtfeldt, U. A., Katsouyanni, K., Janssen, N. A., Martin, R. V., Samoli, E., Schwartz, P. E., Stafoggia, M., Bellander, T., Strak, M., Wolf, K., Vienneau, D., Vermeulen, R., Brunekreef, B., and Hoek, G. (2019). A comparison of linear regression, regularization, and machine learning algorithms to develop Europe-wide spatial models of fine particles and nitrogen dioxide. *Environment International*, 130:104934.

Chen, J. and Hoek, G. (2020). Long-term exposure to pm and all-cause and cause-specific mortality: A systematic review and meta-analysis. *Environment International*, 143:105974.

Cheng, Y., Wiedensohler, A., Eichler, H., Heintzenberg, J., Tesche, M., Ansmann, A., Wendisch, M., Su, H., Althausen, D., and Herrmann, H. (2008). Relative humidity dependence of aerosol optical properties and direct radiative forcing in the surface boundary layer at Xinken in Pearl River Delta of China: An observation based numerical study. *Atmospheric Environment*, 42(25):6373–6397.

Chu, Y., Liu, Y., Li, X., Liu, Z., Lu, H., Lu, Y., Mao, Z., Chen, X., Li, N., Ren, M., Liu, F., Tian, L., Zhu, Z., and Xiang, H. (2016). A review on predicting ground PM2.5 concentration using satellite aerosol optical depth. *Atmosphere*, 7(10):129.

Chueinta, W. and Hopke, P. K. (2001). Beta gauge for aerosol mass measurement. *Aerosol Science and Technology*, 35(4):840–843.

Cohen, A. J., Brauer, M., Burnett, R., Anderson, H. R., Frostad, J., Estep, K., Balakrishnan, K., Brunekreef, B., Dandona, L., Dandona, R., Feigin, V., Freedman, G., Hubbell, B., Jobling, A., Kan, H., Knibbs, L., Liu, Y., Martin, R., Morawska, L., Pope, C. A., Shin, H., Straif, K., Shaddick, G., Thomas, M., Dingenen, R. V., Donkelaar, A. V., Vos, T., Murray, C. J. L., and Forouzanfar, M. H. (2017). Estimates and 25-year trends of the global burden of disease attributable to ambient air pollution: an analysis of data from the global burden of diseases study 2015. *The Lancet*, 389(10082):1907–1918. https://doi.org/10.1016/s0140-6736(17)30505-6.

Crilley, L. R., Shaw, M., Pound, R., Kramer, L. J., Price, R., Young, S., Lewis, A. C., and Pope, F. D. (2018). Evaluation of a low-cost optical particle counter (Alphasense OPC-N2) for ambient air monitoring. *Atmospheric measurement techniques*, 11(2):709–720.

Cugerone, K., De Michele, C., Ghezzi, A., Gianelle, V., and Gilardoni, S. (2018). On the functional form of particle number size distributions: influence of particle source and meteorological variables. *Atmospheric chemistry and physics*, 18(7):4831–4842.

Dang, R., Yang, Y., Hu, X.-M., Wang, Z., and Zhang, S. (2019). A review of techniques for diagnosing the Atmospheric Boundary Layer Height (ABLH) using Aerosol LIDAR data. *Remote Sensing*, 11(13):1590.

Day, D. E. and Malm, W. C. (2001). Aerosol light scattering measurements as a function of relative humidity: a comparison between measurements made at three different sites. *Atmospheric Environment*, 35(30):5169–5176.

Di Antonio, L., Di Biagio, C., Foret, G., Formenti, P., Siour, G., Doussin, J.-F., and Beekmann, M. (2023). Aerosol optical depth climatology from the high-resolution maiac product over europe: differences between major european cities and their surrounding environments. *Atmospheric chemistry and physics*, 23(19):12455–12475.

Di Nicolantonio, W., Cacciari, A., and Tomasi, C. (2009). Particulate matter at surface: Northern italy monitoring based on satellite remote sensing, meteorological fields, and in-situ samplings. *IEEE Journal of Selected Topics in Applied Earth Observations and Remote Sensing*, 2(4):284–292.

Donat, F., Fabbri, E., Maestri, T., Martinazzo, M., Masin, F., Proietti Pelliccia, G., Cassini, L., Masiello, G., Liuzzi, G., and Serio, C. (2024). The cloud identification and classification (CIC) algorithm for high spectral resolution observations in the far-and mid-infrared part of the spectrum. In *Remote Sensing of Clouds and the Atmosphere XXIX*, volume 13193, page 1319302. SPIE.

Downing, H. D. and Williams, D. (1975). Optical constants of water in the infrared. *Journal of Geophysical Research Atmospheres*, 80(12):1656–1661.

Durre, I., Vose, R. S., and Wuertz, D. B. (2006). Overview of the Integrated Global Radiosonde Archive. *Journal of Climate*, 19(1):53–68.

Durre, I., Yin, X., Vose, R. S., Applequist, S., and Arnfield, J. (2018). Enhancing the data coverage in the Integrated Global Radiosonde Archive. *Journal of Atmospheric and Oceanic Technology*, 35(9):1753–1770.

Ensor, D. and Pilat, M. (1971). Calculation of Smoke Plume Opacity from Particulate Air Pollutant Properties. *Journal of the Air Pollution Control Association*, 21(8):496–501.

Eresmaa, N., Härkönen, J., Joffre, S. M., Schultz, D. M., Karppinen, A., and Kukkonen, J. (2012). A Three-Step Method for Estimating the Mixing Height Using Ceilometer Data from the Helsinki Testbed. *Journal of Applied Meteorology and Climatology*, 51(12):2172–2187.

EU (2008). Directive - 2008/50 - en - eur-lex. https://eur-lex.europa.eu/legal-content/en/ALL/?uri=CELEX:32008L0050. Accessed: 2025-10-25.

EU (2024). Directive - eu - 2024/2881 - en - eur-lex. https://eur-lex.europa.eu/legal-content/EN/TXT/?uri=OJ:L_202402881. Accessed: 2025-10-25.

Ferrero, L., Riccio, A., Ferrini, B., D'Angelo, L., Rovelli, G., Casati, M., Angelini, F., Barnaba, F., Gobbi, G., Cataldi, M., and Bolzacchini, E. (2019). Satellite aod conversion into ground pm10, pm2.5 and pm1 over the po valley (milan, italy) exploiting information on aerosol vertical profiles, chemistry, hygroscopicity and meteorology. *Atmospheric Pollution Research*, 10(6):1895–1912.

Ferrero, L., Riccio, A., Perrone, M., Sangiorgi, G., Ferrini, B., and Bolzacchini, E. (2011). Mixing height determination by tethered balloon-based particle soundings and modeling simulations. *Atmospheric Research*, 102(1-2):145–156.

Frontera, A., Martin, C., Vlachos, K., and Sgubin, G. (2020). Regional air pollution persistence links to covid-19 infection zoning. *Journal of Infection*, 81(2):318–356.

Gnendiger, C., Schultze, T., Börger, K., Belt, A., and Arnold, L. (2024). Extinction coefficients from aerosol measurements. *Fire Safety Journal*, 146:104110.

Gualtieri, G., Brilli, L., Carotenuto, F., Cavaliere, A., Giordano, T., Putzolu, S., Vagnoli, C., Zaldei, A., and Gioli, B. (2024). Performance assessment of two

Low-Cost PM2.5 and PM10 monitoring networks in the Padana Plain (Italy). *Sensors*, 24(12):3946.

Gupta, P. and Christopher, S. A. (2008). Seven year particulate matter air quality assessment from surface and satellite measurements. *Atmospheric chemistry and physics*, 8(12):3311–3324.

Hammer, M. S., Donkelaar, A. V., Li, C., Lyapustin, A., Sayer, A. M., Hsu, N. C., Levy, R. C., Garay, M. J., Kalashnikova, O. V., Kahn, R. A., Brauer, M., Apte, J. S., Henze, D. K., Zhang, L., Zhang, Q., Bonne, F., Pierce, J. R., and Martin, R. V. (2020). Global estimates and long-term trends of fine particulate matter concentrations (1998–2018). *Environmental Science & Technology*, 54(13):7879–7890.

Hamra, G. B., Guha, N., Cohen, A., Laden, F., Raaschou-Nielsen, O., Samet, J. M., Vineis, P., Forastiere, F., Saldiva, P., Yorifuji, T., and Loomis, D. (2014). Outdoor particulate matter exposure and lung cancer: A systematic review and meta-analysis. *Environmental Health Perspectives*, 122(9):906–911.

Hand, J. L. and Malm, W. C. (2007). Review of aerosol mass scattering efficiencies from ground-based measurements since 1990. *Journal of Geophysical Research Atmospheres*, 112(D16).

Hänel, G. (1981). An attempt to interpret the humidity dependencies of the aerosol extinction and scattering coefficients. *Atmospheric Environment (1967)*, 15(3):403–406.

Hansen, J. E. and Travis, L. D. (1974). Light scattering in planetary atmospheres. *Space Science Reviews*, 16(4):527–610.

Harrison, R. M. (2020). Airborne particulate matter. *Philosophical Transactions of the Royal Society A: Mathematical, Physical and Engineering Sciences*, 378(2183):20190319.

Harrison, R. M. and Beddows, D. C. (2017). Efficacy of recent emissions controls on road vehicles in europe and implications for public health. *Scientific Reports*, 7(1).

Harrison, R. M., Smith, D. J. T., and Kibble, A. J. (2004). What is responsible for the carcinogenicity of pm2.5? *Occupational and Environmental Medicine*, 61(10):799–805.

Hauck, H., Berner, A., Gomiscek, B., Stopper, S., Puxbaum, H., Kundi, M., and Preining, O. (2004). On the equivalence of gravimetric pm data with teom and beta-attenuation measurements. *Journal of Aerosol Science*, 35(9):1135–1149.

Hayden, K., Anlauf, K., Hoff, R., Strapp, J., Bottenheim, J., Wiebe, H., Froude, F., Martin, J., Steyn, D., and McKendry, I. (1997). The vertical chemical and meteorological structure of the boundary layer in the Lower Fraser Valley during Pacific '93. *Atmospheric Environment*, 31(14):2089–2105.

He, Q., Zhou, G., Geng, F., Gao, W., and Yu, W. (2015). Spatial distribution of aerosol hygroscopicity and its effect on PM2.5 retrieval in East China. *Atmospheric Research*, 170:161–167.

Hess, M., Koepke, P., and Schult, I. (1998). Optical properties of aerosols and clouds: the software package OPAC. *Bulletin of the American Meteorological Society*, 79(5):831–844.

Hirota, J. A., Marchant, D. J., Singhera, G. K., Moheimani, F., Dorscheid, D. R., Carlsten, C., Sin, D., and Knight, D. (2015). Urban particulate matter increases human airway epithelial cell il-1β secretion following scratch wounding and h1n1 influenza a exposure in vitro. *Experimental Lung Research*, 41(6):353–362.

Hoff, R. M. and Christopher, S. A. (2009). Remote Sensing of Particulate Pollution from Space: Have We Reached the Promised Land? *Journal of the Air & Waste Management Association*, 59(6):645–675.

Holben, B., Eck, T., Slutsker, I., Tanré, D., Buis, J., Setzer, A., Vermote, E., Reagan, J., Kaufman, Y., Nakajima, T., Lavenu, F., Jankowiak, I., and Smirnov, A. (1998). AERONET—A federated instrument network and data archive for aerosol characterization. *Remote Sensing of Environment*, 66(1):1–16.

Hooper, W. P. and Eloranta, E. W. (1986). Lidar measurements of wind in the planetary boundary layer: the method, accuracy and results from joint measurements with radiosonde and kytoon. *Journal of climate and applied meteorology*, pages 990–1001.

Huang, Y., Kok, J. F., Martin, R. L., Swet, N., Katra, I., Gill, T. E., Reynolds, R. L., and Freire, L. S. (2019). Fine dust emissions from active sands at coastal oceano dunes, california. *Atmospheric Chemistry and Physics*, 19(5):2947–2964.

Hulst, H. C. and Van De Hulst, H. C. (1981). *Light scattering by small particles*. Courier Corporation.

Jiang, M., Liu, X., Chen, D., Han, J., Wang, Z., and Xu, M. (2019). Light Extinction Method for Measuring a Low Particle Concentration with White Cell Optics: Relationship between Light Transmittance and Particle Properties. *Energy & Fuels*, 33(11):12063–12072.

Jones, R. M. and Brosseau, L. M. (2015). Aerosol transmission of infectious disease. *Journal of Occupational and Environmental Medicine*, 57(5):501–508.

Julaha, K., Ždímal, V., Šmejkalová, A. H., Komínková, K., and Zíková, N. (2024). Boundary layer and mixing layer height: Models vs. Ground-based measurements intercomparison. *Atmospheric Research*, page 107897.

Karagulian, F., Barbiere, M., Kotsev, A., Spinelle, L., Gerboles, M., Lagler, F., Redon, N., Crunaire, S., and Borowiak, A. (2019). Review of the performance of low-cost sensors for air quality monitoring. *Atmosphere*, 10(9):506.

Kiresova, S. and Guzan, M. (2022). Measurement of particulate matter: Principles and options of measurement at present. *Acta Electrotechnica et Informatica*, 22(2):8–18.

Koelemeijer, R., Homan, C., and Matthijsen, J. (2006). Comparison of spatial and temporal variations of aerosol optical thickness and particulate matter over europe. *Atmospheric Environment*, 40(27):5304–5315.

Kopke, P., Hess, M., Schult, I., and Shettle, E. P. (1997). Global aerosol data set. *Max-Planck-Institut fur Meteorologie, 243*.

Krzyzanowski, M. and Cohen, A. (2008). Update of who air quality guidelines. *Air Quality Atmosphere & Health*, 1(1):7–13.

Kuklinska, K., Wolska, L., and Namiesnik, J. (2014). Air quality policy in the u.s. and the eu – a review. *Atmospheric Pollution Research*, 6(1):129–137.

Kwon, H.-S., Ryu, M. H., and Carlsten, C. (2020). Ultrafine particles: unique physicochemical properties relevant to health and disease. *Experimental & Molecular Medicine*, 52(3):318–328.

Lee, J., Kim, J., Song, C. H., Kim, S., Chun, Y., Sohn, B., and Holben, B. (2010). Characteristics of aerosol types from aeronet sunphotometer measurements. *Atmospheric Environment*, 44(26):3110–3117.

Levy, R. C., Mattoo, S., Munchak, L. A., Remer, L. A., Sayer, A. M., Patadia, F., and Hsu, N. C. (2013). The Collection 6 MODIS aerosol products over land and ocean. *Atmospheric measurement techniques*, 6(11):2989–3034.

Li, J., Carlson, B. E., Yung, Y. L., Lv, D., Hansen, J., Penner, J. E., Liao, H., Ramaswamy, V., Kahn, R. A., Zhang, P., Dubovik, O., Ding, A., Lacis, A. A., Zhang, L., and Dong, Y. (2022a). Scattering and absorbing aerosols in the climate system. *Nature Reviews Earth & Environment*, 3(6):363–379.

Li, T., Yu, Y., Sun, Z., and Duan, J. (2022b). A comprehensive understanding of ambient particulate matter and its components on the adverse health effects based from epidemiological and laboratory evidence. *Particle and Fibre Toxicology*, 19(1).

Liou, K. N. (2002). *An introduction to atmospheric radiation*. Elsevier.

Liu, B., Ma, X., Ma, Y., Li, H., Jin, S., Fan, R., and Gong, W. (2022). The relationship between atmospheric boundary layer and temperature inversion layer and their aerosol capture capabilities. *Atmospheric Research*, 271:106121.

Liu, B., Ma, Y., Gong, W., Zhang, M., and Shi, Y. (2019). The relationship between black carbon and atmospheric boundary layer height. *Atmospheric Pollution Research*, 10(1):65–72.

Liu, B., Ma, Y., Shi, Y., Jin, S., Jin, Y., and Gong, W. (2020). The characteristics and sources of the aerosols within the nocturnal residual layer over wuhan, china. *Atmospheric Research*, 241:104959.

Liu, H., Shah, S., and Jiang, W. (2004). On-line outlier detection and data cleaning. *Computers & Chemical Engineering*, 28(9):1635–1647.

Liu, X., Gu, J., Li, Y., Cheng, Y., Qu, Y., Han, T., Wang, J., Tian, H., Chen, J., and Zhang, Y. (2013). Increase of aerosol scattering by hygroscopic growth: Observation, modeling, and implications on visibility. *Atmospheric Research*, 132-133:91–101.

Liu, Y., Jia, R., Dai, T., Xie, Y., and Shi, G. (2014). A review of aerosol optical properties and radiative effects. *Journal of Meteorological Research*, 28(6):1003–1028.

Lyapustin, A., Wang, Y., Korkin, S., and Huang, D. (2018). Modis collection 6 maiac algorithm. *Atmospheric measurement techniques*, 11(10):5741–5765.

Ma, Z., Dey, S., Christopher, S., Liu, R., Bi, J., Balyan, P., and Liu, Y. (2021). A review of statistical methods used for developing large-scale and long-term PM2.5 models from satellite data. *Remote Sensing of Environment*, 269:112827.

Mamouri, R. E., Amiridis, V., Papayannis, A., Giannakaki, E., Tsaknakis, G., and Balis, D. S. (2009). Validation of CALIPSO space-borne-derived attenuated backscatter coefficient profiles using a ground-based lidar in Athens, Greece. *Atmospheric measurement techniques*, 2(2):513–522.

Martin, R. V., Brauer, M., Donkelaar, A. V., Shaddick, G., Narain, U., and Dey, S. (2019). No one knows which city has the highest concentration of fine particulate matter. *Atmospheric Environment X*, 3:100040.

Masiello, G., Serio, C., Liuzzi, G., Pasquariello, P., Giosa, R., Maestri, T., Martinazzo, M., Masin, F., Cassini, L., Donat, F., Proietti Pelliccia, G., Venafra, S., Sgheri, L., and De Cosmo, F. (2024). Developments of the σ-IASI/F2N radiative transfer model: a new linear-in-T approach for accurate treatment of clouds. In *Remote Sensing of Clouds and the Atmosphere XXIX*, volume 13193, pages 8–14. SPIE.

Mazzola, M., Lanconelli, C., Lupi, A., Busetto, M., Vitale, V., and Tomasi, C. (2010). Columnar aerosol optical properties in the Po Valley, Italy, from MFRSR data. *Journal of Geophysical Research Atmospheres*, 115(D17).

Melfi, S., Spinhirne, J., Chou, S.-H., and Palm, S. (1985). Lidar observations of vertically organized convection in the planetary boundary layer over the ocean. *Journal of Applied Meteorology and Climatology*, 24(8):806–821.

Mioche, G., Josset, D., Gayet, J., Pelon, J., Garnier, A., Minikin, A., and Schwarzenboeck, A. (2010). Validation of the CALIPSO-CALIOP extinction coefficients from in situ observations in midlatitude cirrus clouds during the CIRCLE-2 experiment. *Journal of Geophysical Research Atmospheres*, 115(D4).

Morales, K. F., Paget, J., and Spreeuwenberg, P. (2017). Possible explanations for why some countries were harder hit by the pandemic influenza virus in 2009 – a global mortality impact modeling study. *BMC Infectious Diseases*, 17(1).

Munkel, C., Eresmaa, N., Räsänen, J., and Karppinen, A. (2006). Retrieval of mixing height and dust concentration with lidar ceilometer. *Boundary-Layer Meteorology*, 124(1):117–128.

Orellano, P., Reynoso, J., Quaranta, N., Bardach, A., and Ciapponi, A. (2020). Short-term exposure to particulate matter (pm10 and pm2.5), nitrogen dioxide (no2), and ozone (o3) and all-cause and cause-specific mortality: Systematic review and meta-analysis. *Environment International*, 142:105876.

Peña, O. and Pal, U. (2009). Scattering of electromagnetic radiation by a multilayered sphere. *Computer Physics Communications*, 180(11):2348–2354.

Pollack, J. B., Toon, O. B., and Khare, B. N. (1973). Optical properties of some terrestrial rocks and glasses. *Icarus*, 19(3):372–389.

Pucer, J. F. (2019). The correction of teom pm10 measurements at different monitoring sites and climates. *SN Applied Sciences*, 1(10).

Qin, W., Fang, H., Wang, L., Wei, J., Zhang, M., Su, X., Bilal, M., and Liang, X. (2021). MODIS high-resolution MAIAC aerosol product: Global validation and analysis. *Atmospheric Environment*, 264:118684.

Randriamiarisoa, H., Chazette, P., Couvert, P., Sanak, J., and Mégie, G. (2006). Relative humidity impact on aerosol parameters in a Paris suburban area. *Atmospheric chemistry and physics*, 6(5):1389–1407.

Raza, A., Bellander, T., Bero-Bedada, G., Dahlquist, M., Hollenberg, J., Jonsson, M., Lind, T., Rosenqvist, M., Svensson, L., and Ljungman, P. L. S. (2013). Short-term effects of air pollution on out-of-hospital cardiac arrest in stockholm. *European Heart Journal*, 35(13):861–868.

Renard, J.-B., Dulac, F., Berthet, G., Lurton, T., Vignelles, D., Jégou, F., Tonnelier, T., Jeannot, M., Couté, B., Akiki, R., Verdier, N., Mallet, M., Gensdarmes, F., Charpentier, P., Mesmin, S., Duverger, V., Dupont, J.-C., Elias, T., Crenn, V., Sciare, J., Zieger, P., Salter, M., Roberts, T., Giacomoni, J., Gobbi, M., Hamonou, E., Olafsson, H., Dagsson-Waldhauserova, P., Camy-Peyret, C., Mazel, C., Décamps, T., Piringer, M., Surcin, J., and Daugeron, D. (2016). LOAC: a small aerosol optical counter/sizer for ground-based and balloon measurements of the size distribution and nature of atmospheric particles – Part 1: Principle of measurements and instrument evaluation. *Atmospheric measurement techniques*, 9(4):1721–1742.

Renard, J.-B., Thaury, C., Mineau, J.-L., and Gaubicher, B. (2010). Small-angle light scattering by airborne particulates: Environnement S.A. continuous particulate monitor. *Measurement Science and Technology*, 21(8):085901.

Ricciardelli, I., Bacco, D., Rinaldi, M., Bonafè, G., Scotto, F., Trentini, A., Bertacci, G., Ugolini, P., Zigola, C., Rovere, F., Maccone, C., Pironi, C., and Poluzzi, V. (2016). A three-year investigation of daily pm2.5 main chemical components in four sites: the routine measurement program of the supersito project (po valley, italy). *Atmospheric Environment*, 152:418–430.

Rindelaub, J. D., Salmond, J. A., Fan, W., Miskelly, G. M., Dirks, K. N., Henning, S., Conrath, T., Stratmann, F., and Coulson, G. (2025). Aerosol mass concentrations and dry/wet deposition of atmospheric microplastics at a remote coastal location in new zealand. *Environmental Pollution*, 372:126034.

Rogozovsky, I., Ohneiser, K., Lyapustin, A., Ansmann, A., and Chudnovsky, A. (2023). The impact of different aerosol layering conditions on the high-resolution

MODIS/MAIAC AOD retrieval bias: The uncertainty analysis. *Atmospheric Environment*, 309:119930.

Scotto, F., Bacco, D., Lasagni, S., Trentini, A., Poluzzi, V., and Vecchi, R. (2021). A multi-year source apportionment of pm2.5 at multiple sites in the southern po valley (italy). *Atmospheric Pollution Research*, 12(11):101192.

Serio, C., Masiello, G., Liuzzi, G., Cersosimo, A., Maestri, T., Martinazzo, M., Masin, F., Proietti Pelliccia, G., Venafra, S., and Camy-Peyret, C. (2024). Demonstration of a physical inversion scheme for all-sky, day-night IASI observations and application to the analysis of the onset of the Antarctica ozone hole: assessment of retrievals and consistency of forward modeling. *Journal of Quantitative Spectroscopy and Radiative Transfer*, 329:109211.

Sharma, S., Chandra, M., and Kota, S. H. (2020). Health effects associated with pm2.5: a systematic review. *Current Pollution Reports*, 6(4):345–367.

Shi, Y., Liu, B., Chen, S., Gong, W., Ma, Y., Zhang, M., Jin, S., and Jin, Y. (2020). Characteristics of aerosol within the nocturnal residual layer and its effects on surface pm2. 5 over china. *Atmospheric Environment*, 241:117841.

Shin, M., Kang, Y., Park, S., Im, J., Yoo, C., and Quackenbush, L. J. (2019). Estimating ground-level particulate matter concentrations using satellite-based data: a review. *GIScience & Remote Sensing*, 57(2):174–189.

Shukla, K. and Aggarwal, S. G. (2022). A technical overview on beta-attenuation method for the monitoring of particulate matter in ambient air. *Aerosol and Air Quality Research*, 22(12):220195.

Sorek-Hamer, M., Chatfield, R., and Liu, Y. (2020). Review: Strategies for using satellite-based products in modeling PM2.5 and short-term pollution episodes. *Environment International*, 144:106057.

Southerland, V. A., Brauer, M., Mohegh, A., Hammer, M. S., Donkelaar, A. V., Martin, R. V., Apte, J. S., and Anenberg, S. C. (2022). Global urban temporal trends in fine particulate matter (pm2.5) and attributable health burdens: estimates from global datasets. *The Lancet Planetary Health*, 6(2):e139–e146.

Stafoggia, M., Bellander, T., Bucci, S., Davoli, M., De Hoogh, K., De' Donato, F., Gariazzo, C., Lyapustin, A., Michelozzi, P., Renzi, M., Scortichini, M., Shtein, A., Viegi, G., Kloog, I., and Schwartz, J. (2019). Estimation of daily pm10 and pm2.5 concentrations in italy, 2013–2015, using a spatiotemporal land-use random-forest model. *Environment International*, 124:170–179.

Stull, R. B. (2012). *An introduction to boundary layer meteorology*, volume 13. Springer Science & Business Media.

Tesche, M., Wandinger, U., Ansmann, A., Althausen, D., Müller, D., and Omar, A. H. (2013). Ground-based validation of CALIPSO observations of dust and smoke in the Cape Verde region. *Journal of Geophysical Research Atmospheres*, 118(7):2889–2902.

Thangavel, P., Park, D., and Lee, Y.-C. (2022). Recent insights into particulate matter (pm2.5)-mediated toxicity in humans: An overview. *International Journal of Environmental Research and Public Health*, 19(12):7511.

Tositti, L., Brattich, E., Masiol, M., Baldacci, D., Ceccato, D., Parmeggiani, S., Stracquadanio, M., and Zappoli, S. (2013). Source apportionment of particulate matter in a large city of southeastern po valley (bologna, italy). *Environmental Science and Pollution Research*, 21(2):872–890.

Turner, M. C., Krewski, D., Diver, W. R., Pope, C. A., Burnett, R. T., Jerrett, M., Marshall, J. D., and Gapstur, S. M. (2017). Ambient air pollution and cancer mortality in the cancer prevention study ii. *Environmental Health Perspectives*, 125(8).

Twitty, J. T. and Weinman, J. A. (1971). Radiative properties of carbonaceous aerosols. *Journal of Applied Meteorology (1962-1982)*, 10(4):725–731.

Volz, F. E. (1972). Infrared absorption by atmospheric aerosol substances. *Journal of Geophysical Research Atmospheres*, 77(6):1017–1031.

Volz, F. E. (1973). Infrared optical constants of ammonium sulfate, sahara dust, volcanic pumice, and flyash. *Applied Optics*, 12(3):564.

Wang, J. and Christopher, S. A. (2003). Intercomparison between satellite-derived aerosol optical thickness and PM2.5 mass: Implications for air quality studies. *Geophysical Research Letters*, 30(21).

Wang, M., Kim, R. Y., Kohonen-Corish, M. R. J., Chen, H., Donovan, C., and Oliver, B. G. (2025). Particulate matter air pollution as a cause of lung cancer: epidemiological and experimental evidence. *British Journal of Cancer*.

Wang, Z., Chen, L., Tao, J., Liu, Y., Hu, X., and Tao, M. (2014). An empirical method of RH correction for satellite estimation of ground-level PM concentrations. *Atmospheric Environment*, 95:71–81.

Wang, Z., Chen, L., Tao, J., Zhang, Y., and Su, L. (2009). Satellite-based estimation of regional particulate matter (PM) in Beijing using vertical-and-RH correcting method. *Remote Sensing of Environment*, 114(1):50–63.

Warren, S. G. and Brandt, R. E. (2008). Optical constants of ice from the ultraviolet to the microwave: A revised compilation. *Journal of Geophysical Research Atmospheres*, 113(D14).

Watkins, A., Danilewitz, M., Kusha, M., Massé, S., Urch, B., Quadros, K., Spears, D., Farid, T., and Nanthakumar, K. (2012). Air pollution and arrhythmic risk: The smog is yet to clear. *Canadian Journal of Cardiology*, 29(6):734–741.

Wei, X., Chang, N.-B., Bai, K., and Gao, W. (2019). Satellite remote sensing of aerosol optical depth: advances, challenges, and perspectives. *Critical Reviews in Environmental Science and Technology*, 50(16):1640–1725.

Whaley, P., Nieuwenhuijsen, M., and Burns, J. (2021). Update of the who global air quality guidelines: Systematic reviews. *Environment International*.

WHO (2000). Guidelines for air quality. https://iris.who.int/items/67294b60-6eda-45ad-8c83-c0571790cf41. Accessed: 2025-10-25.

WHO (2003). Health aspects of air pollution with particulate matter, ozone and nitrogen dioxide. report on a who working group. https://www.who.int/publications/i/item/9789240034228/. Accessed: 2025-10-25.

WHO (2006). Air quality guidelines: global update 2005: particulate matter, ozone, nitrogen dioxide and sulfur dioxide. https://www.who.int/europe/publications/i/item/9289021926. Accessed: 2025-10-25.

WHO (2021). Global air quality guidelines: particulate matter (pm2.5 and pm10), ozone, nitrogen dioxide, sulfur dioxide and carbon monoxide. https://www.who.int/publications/i/item/9789240034228/. Accessed: 2025-10-25.

Winker, D. (2025). CALIPSO - Cloud-Aerosol LIDAR and Infrared Pathfinder satellite observations. https://www-calipso.larc.nasa.gov/. Accessed: 2025-10-25.

Winker, D. M., Pelon, J., Coakley, J. A., Ackerman, S. A., Charlson, R. J., Colarco, P. R., Flamant, P., Fu, Q., Hoff, R. M., Kittaka, C., Kubar, T. L., Treut, H. L., Mccormick, M. P., Mégie, G., Poole, L., Powell, K., Trepte, C., Vaughan, M. A., and Wielicki, B. A. (2010). The CALIPSO mission. *Bulletin of the American Meteorological Society*, 91(9):1211–1230.

Winker, D. M., Vaughan, M. A., Omar, A., Hu, Y., Powell, K. A., Liu, Z., Hunt, W. H., and Young, S. A. (2009). Overview of the CALIPSO mission and CALIOP data processing algorithms. *Journal of Atmospheric and Oceanic Technology*, 26(11):2310–2323.

Yang, P., Bi, L., Baum, B. A., Liou, K.-N., Kattawar, G. W., Mishchenko, M. I., and Cole, B. (2012). Spectrally Consistent Scattering, Absorption, and Polarization Properties of Atmospheric Ice Crystals at Wavelengths from 0.2 to 100 μm. *Journal of the Atmospheric Sciences*, 70(1):330–347.

Zheng, C., Zhao, C., Zhu, Y., Wang, Y., Shi, X., Wu, X., Chen, T., Wu, F., and Qiu, Y. (2017). Analysis of influential factors for the relationship between PM2.5 and AOD in Beijing. *Atmospheric chemistry and physics*, 17(21):13473–13489.

Zieger, P., Fierz-Schmidhauser, R., Weingartner, E., and Baltensperger, U. (2013). Effects of relative humidity on aerosol light scattering: results from different european sites. *Atmospheric chemistry and physics*, 13(21):10609–10631.

Finanziato dall'Unione europea- Next Generation EU, Missione 4, Componente 2, Investimento 3.3 (D.M. 117/2023) CUP J33C22002610002